UNIVERSITEIT•STELLENBOSCH•UNIVERSITY
jou kennisvennoot • your knowledge partner

Experimental and Numerical Analysis of Axial Flow Fans

by

Ockert P.H. Augustyn

Thesis presented in partial fulfilment of the requirements for the degree of Master of Engineering (Mechanical) in the Faculty of Engineering at Stellenbosch University

Supervisor: Dr S.J. van der Spuy
Co-supervisor: Prof. T.W. von Backström

December 2013

Departement Meganiese en Megatroniese Ingenieurswese
Department of Mechanical and Mechatronic Engineering

Declaration

By submitting this thesis electronically, I declare that the entirety of the work contained therein is my own, original work, that I am the sole author thereof (save to the extent explicitly otherwise stated), that reproduction and publication thereof by Stellenbosch University will not infringe any third party rights and that I have not previously in its entirety or in part submitted it for obtaining any qualification.

Date: ....

Abstract

Experimental and Numerical analysis of axial flow fans

O.P.H. Augustyn

Department of Mechanical and Mechatronic Engineering, Stellenbosch University,
Private Bag X1, Matieland 7602, South Africa.
Thesis: MScEng (Mech)

December 2013

The majority of power stations in South Africa are located in coal rich, but arid regions where wet-cooled condenser systems are not feasible from an environmental and economic perspective. Consequently the focus on power generation cooling has shifted towards dry-cooling systems using air-cooled steam condensers (ACSC). The steam passing through the ACSC units is cooled by an air-draught, mechanically induced by large diameter axial flow fans. Consequently the effectiveness of the cooling is impacted by the performance of these fans, which ultimately affects the overall efficiency of the power plant. However, due to the large diameters (> 10 m) of these fans, their performance is predicted based on small scale test results using the fan scaling laws.

The objective of this project was to develop a methodology which accurately predicts the fan performance of more than one fan configuration using computational fluid dynamics (CFD) software and validating the results with experimental tests. Four fans were considered in this study of which three were scaled fan models of large air-cooled axial fans. The performance of the scaled fan models (L1-, L2- and N-fan) were measured in a type A, BS 848 standard fan test facility. The geometries of the fans were scanned three-dimensionally to obtain the models for simulation purposes. The other fan considered was an 8-bladed axial fan designed by Bruneau (1994) and referred to as the B-fan. Simulations were carried out for the L2-, N- and B-fan for different computational domains while implementing the multiple reference frames (MRF) and steady RANS approach. Three variations of the k-ε turbulence model were also investigated.

Noticeable differences were found between the experimental and numerical results of the B-fan. Good correlations between the numerical and experimental fan static pressure, fan power and fan static efficiency were found for the two scaled model fans over a large operating range. The performance of the full scale fans, however, did not correlate well with the performance of the scaled models. It is concluded that accurate simulations of axial fans are possible although these domains require a large number of mesh elements. It is recommended that further research is carried out to investigate the relationship between full scale and small scale fan models.

Uittreksel

Eksperimentele en Numeriese analiese van aksiaalvloeiwaaiers

O.P.H. Augustyn

Departement van Meganiese en Megatroniese Ingenierswese,
Universiteit van Stellenbosch
Privaatsak X1, Matieland 7602, Suid Afrika.
Tesis: MSc. Ing. (Meg)

December 2013

Die meerderheid steenkool kragstasies in Suid-Afrika is geleë in droë, maar steenkool ryke streke waar natverkoelde kondensor stelsels uit ŉ omgewings en ekonomiese perspektief nie geskik is nie. Die fokus in kragopwekking verkoeling het dus verskuif na droë-verkoelings stelsels en spesifiek die gebruik van lugverkoelde stoomkondensors (LVSKs). Die stoom in LVSK eenhede word verkoel deur atmosferiese lug wat meganies geïnduseer word deur groot aksiaalvloeiwaaiers. Die effektiwiteit van die verkoelingsproses word gevolglik beïnvloed deur die werksverrigting van hierdie waaiers wat uiteindelik die algehele effektiwiteit van die kragstasie beïnvloed. As gevolg van hierdie waaiers se grootte word hulle werksverrigting egter bepaal op grond van kleinskaal toetsresultate en deur gebruik te maak van die waaierskaleringswette.

Die hoofdoelwit van hierdie projek was om ‘n metodiek te ontwikkel wat die werksverrigting van ŉ aksiaalwaaier akkuraat kan voorspel vir ŉ verskeidenheid opstellings, deur gebruik te maak van berekenings vloei meganika (BVM) sagteware en die resultate eksperimenteel te verifieer. Die projek het vier waaiers ondersoek waarvan drie van hierdie waaiers geskaleerde modelle van groot lugverkoelde aksiaalwaaiers was. Die werksverrigting van die geskaleerde waaiers (L1-, L2- en N-waaier) was met ‘n tipe A, BS 848 standaard waaier toetsfasiliteit gemeet. Die geometrie van dié waaiers was ook drie-dimensioneel opgemeet vir simulasie doeleindes. Die B-waaier, ‘n 8 lem aksiaalwaaier, wat ontwerp is deur Bruneau (1994) was slegs numeries ondersoek. Die L2-, N- en B-waaier was gesimuleer in verskillende berekeningsdomeine deur gebruik te maak van die multi verwysingsraamwerk en gestadigde vloeiberekenings benaderings. Drie k-ε turbulensie modelle was ook ondersoek.

Merkbare verskille tussen die eksperimentele en numeriese resultate van die B-waaier was waargeneem. Goeie korrelasie tussen die eksperimentele en numeriese resultate van die geskaleerde waaiers vir ‘n wye bedryfsbestek was gevind. ‘n Vergelyking tussen die volskaal en kleinskaal waaiers se werksverrigting het egter beduidende afwykings aangetoon. Deur gebruik te maak van ‘n groot aantal selle in die berekeningsdomein was dit moontlik om ŉ verskeidenheid aksiaalvloeiwaaiers akkuraat te simuleer. Verdere navorsing wat die verhouding tussen volskaal en kleinskaal waaiers ondersoek woord aanbeveel.

Acknowledgements

Thank you Dr. van der Spuy and Prof. von Backström for all you advice, guidance, encouragement and positive critique.

Thank you Prof. Meyer for your inspiration to help me think out of the box.

Jutami Botha (soon to be Augustyn) you are such a blessing and I appreciate you a little more than a lot.

Thank you, Mom, Dad, Ria and Susan for your support and encouragement throughout the entire project.

The best friends in the world who made life outside work an absolute joy. You know who you are.

Thank you to the mechanical department's staff that had to endure with me for 3 years. Cobus, Ferdi, Greamme, Calvin, Murisha, Julian and Nati. You are worth gold.

My office friend, Andrew Gill, you deserve to be in this project's reference list. Thank you for your friendship, wisdom and patient attitude.

To the One I live for, in whom I have found life!

Contents

List of Figures

List of Tables

Nomenclature

Symbols

A	Area	m^2
C	Flow velocity, Turbulence constant	$m.s^{-1}$
D	Diameter	m
E	Wall roughness constant	~
L	Length scale	m
N	Rotational speed	rpm
P	Power	W
R	Gas constant	$J.kg^{-1}.K^{-1}$
S	Mean strain	~
T	Temperature, Torque	(K/°C)/ N.m
U	Free stream velocity	$m.s^{-1}$
X	Body forces	~
c	Mass average velocity magnitude	$m.s^{-1}$
f	Wall-damping function	~
k	*Turbulent kinetic energy*	$m^2.s^{-2}$
p	Pressure	Pa
r	Radius	m
t	Thickness distribution	m
u, v, w	Velocity components	$m.s^{-1}$
y	Normal distance from the wall	m

$\alpha\varepsilon$	Compound coefficient	~
ε	Turbulent dissipation rate	m^{2}.s^{-3}
ι	Turbulence length scale	m
κ	Von Karman’s constant	~
λ	Turbulent viscosity blending function	~
μ	Dynamic Viscosity	kg.m^{-1}.s
ν	Kinematic Viscosity	m^{2}.s^{-1}
ρ	Density	kg.m^{-3}
σ	Normal stress	Pa
τ	Shear stress	Pa
ω	Angular velocity, specific dissipation rate	rad.s^{-1}/ s^{-1}
ϑ	Turbulence velocity scale	m.s^{-1}
ϕ	Flow coefficient	~
$\dot{V}'$	Scaled volumetric flow rate	m^{3}.s^{-1}
N'	Scaled rotational speed	rpm
P'	Scale rotational power	W
$\dot{V}$	Volumetric flow rate	m^{3}/s
$\dot{m}$	Mass flow rate	kg.s^{-1}
p'	Scaled rotational pressure	Pa
t'	Approximated thickness distribution	m
u', v', w'	Fluctuating velocity components	m.s^{-1}
δ_{ij}	Kronecker Delta	~

$\tilde{v}$	Turbulent kinematic viscosity	$m^2.s^{-1}$
Δ	Differential	~
Ω	Mean rate-of-rotation	~

Subscript

0	Zero value
a	Axial
c	Camber
$drift$	Compensated for drift
$dsett$	Dynamic component in settling chamber
e	
FS	Fan static
i	Inner/hub diameter
i, j, k	Tensor notation
m	Mass
no_load	No load shaft torque
o	Outer/tip diameter
s	Static, small scale
scale	Thickness distribution scale factor

t	Thickness distribution, total, turbulent viscosity
t1	Upper thickness distribution coordinate
t2	Lower thickness distribution coordinate
tip	Fan blade tip
w	Wall
x, y, z	Cartesian directions
x_t=x_c	Joint coordinate for x_t and x_c
amb	Ambient
$bell$	Inlet bellmouth
$sett$	Settling chamber
$t, 2layer$	2-layered turbulent viscosity
t, enh	Enhanced Wall Treatment turbulent viscosity
$v1$	Spalart-Allmaras wall damping function
ε	Turbulent dissipation rate
μ	Turbulent viscosity constant
—	Time-averaged quantity

1 Introduction

The majority of South Africa's power is produced from coal-fired power plants situated in semi-arid regions. Choosing the source of cooling for these power generating cycles has become an important and increasingly complex problem. This can be attributed to the limited availability and rising cost of water in the vicinity of plant sites, noise restrictions, environmental considerations and proliferating legislation. Furthermore, restrictions on thermal discharge from natural bodies of water in evaporative cooling have more recently resulted in the use of closed cycle systems (Kröger, 1998). There are mainly two methods used for cooling power generation cycles: Evaporative- or wet-cooling and dry-cooling.

Historically wet-cooled power stations have been utilized due to their higher thermal efficiencies, although an adequate supply of suitable water is required compared to dry-cooled systems. However, with an annual rainfall of half the global average, water scarcity is a reality in South Africa. Approximately 97% of power station water usage in South Africa is attributed to cooling, and power generation in South Africa accounts for 1.5 % of the country's total annual water consumption (Pather, 2004). Taking this into consideration and the fact that most newly built and currently constructed power stations are located in coal rich but water scarce regions, wet-cooled systems are not feasible from an environmental and economic perspective. Consequently the focus on power generation cooling has shifted towards dry-cooling systems using air-cooled heat exchangers (ACHE). Figure 1.1 shows the direct dry-cooled system of the Medupi coal-fired power plant currently constructed in Lephalale, South Africa. At its completion Medupi, producing 4800 MWe, will have the largest dry-cooled system in the world.

Figure 1.1 - Dry-cooled system of Medupi power station currently under construction.

ACHEs can be cooled by means of natural draught or mechanical draught. Natural draught systems usually make use of cooling towers and an indirect cooling process. Kendal power station situated in South Africa is an example of an indirect dry-cooled plant using cooling towers to induce a natural draught through its ACHEs. This is the largest indirect dry-cooled power station in the world having a total capacity of 4100 MWe. Mechanical draught dry-cooled systems use axial fans to force air through the ACHE. In a direct dry-cooled system, using mechanical draught, the steam exiting the turbine passes directly through to the ACHE where it condenses. These units are referred to as air-cooled steam condensers (ACSC).

The performance of ACSC units, as part of the power generation cycle, has a large impact on the overall efficiency of the plant. This can be explained by considering Figure 1.2, a T-s diagram of a Rankine cycle.

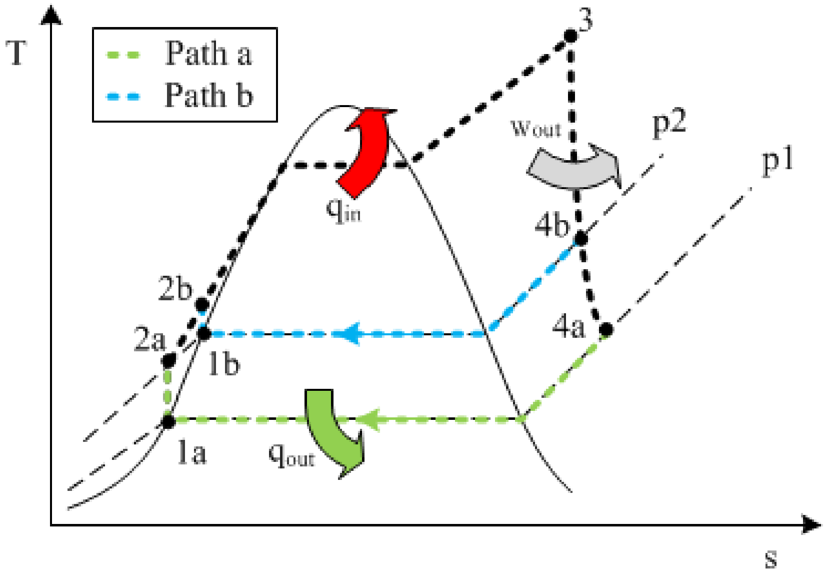

Figure 1.2 - Rankine energy cycle

Heat is added (q_{in}), using a boiler, to the cycle in order for the water to reach a superheated steam condition (point 3). The pressure at this point is fixed and independent of the performance of the turbine or cooling system. The superheated steam passes through the turbine and work is done. The amount of work done by the turbine is determined by the pressure difference across the turbine inlet and outlet (backpressure). Thus, an increase in the back pressure will result in a decrease in work output (W_{out}). Consequently the back pressure is constantly monitored to ensure that the pressure at the turbine outlet remains constant (indicated by design Path a). If the total heat rejected (q_{out}) is not enough to ensure a condensed liquid at the condenser exit, the air flow rate through the ACSC units must be increased. In certain scenarios the heat rejection rate may still not be enough to ensure a condensed liquid and constant backpressure, possibly due to adverse weather conditions. In such cases the back pressure will increase and the system will subsequently operate as indicated by Path b. The pressure increase reduces the amount of enthalpy to be removed from the saturated fluid to reach a fully condensed liquid. The efficiency of a plant is defined as,

$$\eta = \frac{W_{out}}{q_{in}} \tag{1.1}$$

and therefore the efficiency of the entire power generation cycle increases with an decrease in the back pressure. Therefore if the ACSC units cannot provide adequate cooling for a wide range of operating conditions the efficiency of the plant will be adversely affected. The scenario presented above illustrates the importance of well-designed and effective ACSC units which includes the various factors which influence the ACSC unit's performance. Factors which influence the performance (ability to reject heat) of an ACSC include the ambient dry-bulb temperature, air density, finned tubes temperature and air flow rate created by the fans (Le Roux, 2010).

The heat rejection rate of ACSC units is greatly influenced by the air flow rate through the heat exchanger and recirculation forming below the cooling tower (Bredell et al., 2006; Zhao et al., 2012). Numerous studies have been conducted, specifically focussing on the effect of distorted inflow conditions which affect the performance of the large axial fans and consequently the performance of an ACSC. Distorted inflow conditions are caused by structures, windy conditions, other surrounding fans and the positioning of the fan itself in an array. Stinnes and Von Backstrom (2002) and Hotchkiss et al. (2006) showed that the performance of axial fans is adversely affected by cross-flow. Experimental results showed a reduction in the volume flow rate for the same fan static pressure values with increasing cross-flow angle.

Authors such as Bredell et al. (2006), Owen and Kröger (2010) and Louw (2011) conducted studies simulating the full scale fans in arrays using simplified methods and favourable results were found. Van der Spuy et al. (2010) also carried out numerous simulations using simplified methods to model the performance of scaled axial flow fan arrays and comparing them with experimental results. Although simplified methods are less resource intensive, these methods have shown to be inaccurate in the near-stall region (Van der Spuy, 2011). Nevertheless Van der Spuy et al. (2010) accurately predicted the performance of the axial fan array for the normal operating region but recommended that a full explicit CFD simulation on an axial fan be carried out for off-design operating conditions.

The performance of axial fans in an ACSC is subsequently a critical component in the design and operation of ACSC units. However, the performance of large diameter fans, such as the fans used in ACSC units, cannot be determined from experiments. Large diameter axial cooling fans, such as the E-series from Howden (see Figure 1.3), can be up to 14.63 m (48 ft.) in diameter, which makes it impractical to test or monitor on site.

Therefore, the performance specifications of these large axial fans are based on small scale test results. The scaled model's performance is adjusted to the actual geometric specifications using the fan scaling laws. However, literature suggests that due to the difference between the Reynolds numbers (based on the chord length) of the scaled and actual fan model the performance cannot simply be adjusted using the fan scaling laws (Heß and Pelz, 2010; Pelz et al., 2012).

Figure 1.3 - Howden E-series industrial axial fan (Howden, 2007)

The accuracy of the design performance of large axial fans used specifically in large air-cooled condensers is uncertain due to the fact that these fans cannot be tested in a standard test facility. Studies have been conducted, as mentioned above, to simulate large axial fans in operation but only limited understanding has been gained due to the simplicity of the models. The accurate simulation of different geometry fans holds multiple benefits. Being able to accurately predict the performance of large axial fans in changing weather conditions will ultimately result in more efficient ACSC units and more efficient and environmentally friendly power plants.

1.1 Project objectives

A previous study conducted by Le Roux (2010) at the University of Stellenbosch considered the full explicit simulation and testing of the B2-fan which was designed by Bruneau (1994). The simulations carried out by Le Roux (2010) resulted in good correlation at the design point and higher flow rates when using a single reference frame approach. However, the numerical results deviated from the experimental results in the near-stall region. Therefore, questions regarding the simulation of axial fans, especially in the near-stall region, remained. This project can be regarded as a continuation of the work of Le Roux (2010).

The primary objective of this project is to find a methodology, using ANSYS CFD software, which accurately predicts the fan performance for more than one fan configuration. This methodology must use multiple reference frames in order to enable the user to simulate and examine the operation of multiple fans, as typically found in an ACSC. Furthermore, the economic use of computational resources to simulate these fans is essential. However, this should not be to the detriment of simulation accuracy. Therefore, the methodology is to be validated by simulating the B2-fan, designed by Bruneau, (1994) and comparing the numerical results with Le Roux (2010)'s experimental results.

To develop the methodology mentioned above a geometric model of the B2-fan was initially created using the design specifications given by Bruneau (1994). Instead of using *NUMECA FineTurbo* CFD software, used by Le Roux (2010), ANSYS *TurboGrid* is be used to simulate the B-fan using the same computational domain and boundary conditions as described by Le Roux (2010). Once the simulations have reproduced the results of Le Roux (2010) a methodology would have been established that could be improved upon. The primary focus of the project was then approached.

To achieve the primary objective three scaled axial fans (L1-, L2- and N-fan) were tested in a BS 848 test facility and simulated using the methodology developed simulating the B-fan. The geometric models of the scaled fans were generated by means of reverse engineering. The numerical results were compared to the experimental results. The possibility of generating an average representative blade from multiple blade measurements was also examined.

2 Literature review

Initial literature studies indicated that extensive research has been performed on the numerical and experimental testing of turbomachinery. Lately increased attention has specifically been given to the simulation of axial flow fans. This can be attributed to the minimum energy efficiency requirements for fans that have been implemented, for example in Europe (Guedel et al., 2012). The earlier mentioned study by Le Roux (2010), simulating axial fans, pointed out that there was very little evidence of numerical simulations conducted on axial flow fans at that stage. For the purposes of this project, literature was not only used to identify the various methodologies that are commonly used in simulating axial fans, but also to examine different solving techniques, turbulence models and software used to simulate axial fans. Various approximations are made in the CFD modelling of flow fields and therefore deviations were expected. Acceptable values for convergence, residuals levels and correlation of general performance were therefore also investigated.

To simulate rotating machinery in CFD, various approaches to modelling the rotor can be taken. These include approximate models of the rotor such as the pressure jump approach (Shankaran and Dogruoz, 2010; Van der Spuy et al., 2010) and the actuator disk model (ADM) approach. The ADM approach described in-depth by Thiart and von Backström (1993) has been validated by numerous authors (Bredell et al., 2006; Meyer and Kröger, 2001; Van der Spuy et al., 2010). This approach can accurately predict the performance of axial fans for a large range of flow rates. The ADM, however, was found to under-predict the performance at lower flow rates further away from the design point (Le Roux, 2010). The pressure jump and actuator disk models do not require physical modelling of the fan, but represents the operation of the fan by means of momentum source terms. A more accurate representative approach involves simulating an actual fan model in multiple moving reference frames. For steady state simulations, the multiple reference frame (MRF) approach (otherwise known as the frozen-rotor approach) and the mixing plane approach can be used. The sliding mesh approach is used for an unsteady (transient) simulation. These approaches all require a three-dimensional model of the fan geometry (ANSYS Fluent, 2011). Most of the numerical simulations for rotational systems currently implement the MRF or sliding mesh approach.

Le Roux (2010) conducted a study on the numerical simulation and experimental testing of the B2-fan. Simulations of 1/8th of the fan were conducted in a simplified version of the BS 848 (type A) test facility using *NUMECA FINE/Turbo*. The B2-fan has a diameter of 1.542 m and hub-tip ratio of 0.4. Simulations were carried out using the 1-equation Spalart-Allmaras turbulence model (Spalart and Allmaras, 1992). A mass flow inlet and static pressure outlet with radial equilibrium was specified at the inlet and outlet boundaries respectively. Large deviations in performance (errors of 30-50%) between numerical and experimental values were found when the MRF and mixing plane approach for rotational domains were applied. However, by rotating the entire domain at the rotational speed of the fan, good correlation was found at higher flow rates. Le Roux (2010) recommended the use of other software packages and turbulence models such as the k-ε turbulence models. Cyrus et al. (2012) also made use of *NUMECA Fine/Turbo* software to simulate a high pressure axial fan, although the fan was smaller in diameter (600 mm). A mixing plane approach using the Spalart-Allmaras turbulence model was applied and the boundary conditions resembled those of Le Roux (2010). Although periodicity was used, the inlet region’s periodicity differed from the rest of the computational domain where a 180° sector was modelled. Numerical results were validated by experimental tests and the data from these tests correlated well in the region of the design point. No simulations at a flow coefficient of less than 0.5 were conducted. As was the case with Le Roux (2010), the torque was under-predicted.

According to De Gennaro and Kuehnelt (2012), axial flow fans can be seen as rotating fluid machines and the Navier-Stokes equations can either be solved by a MRF or sliding mesh approach. Principally, solving the Navier-Stokes (N-S) equations directly would be ideal. Due to the non-linearity of these equations and the computational cost, there are two main approaches for solving these equations – the Reynold’s Averaged Navier-Stokes (RANS) equations and Large Eddy Simulations (LES).

A time-averaged decomposition of the instantaneous velocity in a flow field is solved using the Navier-Stokes equations, resulting in the development of the RANS equations. This procedure creates the problem of mathematical closure which results in the need for turbulence models. LES is a time-dependent approach which specifically focuses on capturing and accurately modelling large eddies by mesh filtering. Choosing the correct approach and turbulence model becomes a trade-off between the level of detail required and the computational resources available (De Gennaro and Kuehnelt, 2012).

Cezario (2012) analysed a fan-cooled electric motor and evalutated various turbulence models while paying specific attention to the effect of the y^+-value and mesh size. All simulations were carried out in *ANSYS CFX* and were validated by experimental tests carried out on a specially manufactured electrical motor (which was simplified for close correlation with the numerical geometry). The k-ω SST turbulence model, a combination of the k-ε and k-ω turbulence models derived by Menter (1993) and the standard k-ε turbulence model, was examined. The wall y^+- value for the k-ω SST model was specified to be smaller than 2 and for the k-ε model, utilizing the wall function, it was greater than 11. A sensitivity study on different y^+-values indicated the importance of using the correct y^+-values.

The correlation between the numerical and experimental values for both turbulence models were found to range from adequate to very good, even though the SST model showed greater robustness, accuracy and a larger computational time. The k-ω SST turbulence model was also used in simulations by Pascu et al. (2009), Bamberger and Carolus (2012) and De Gennaro and Kuehnelt (2012).

Bamberger and Carolus (2012) simulated a small axial fan (D = 300 mm) in *ANSYS CFX* with periodic boundaries using a mass flow inlet and ambient static pressure outlet. *ANSYS TurboGrid* was used to create a structured hexahedral mesh containing 1 million cells with a ducted inlet and outlet stretching one diameter upstream and two diameters downstream. The numerical results were validated by comparison to experimental results and showed very good correlation for higher to mid flow rates even though the experimental test facility and computational domain differed slightly. Simulations were not carried out for low flow rates. It should be noted that the average total pressure upstream of the fan was determined by calculating the sum of the area-averaged static pressure p_s and the mass-averaged velocity magnitude c in the following manner:

$$p_t = p_s + \rho\frac{c^2}{2} \tag{2.1}$$

A similar setup was used for the numerical work carried out by De Gennaro and Kuehnelt (2012), although a polyhedral mesh was used. The focus of both studies was to accurately predict fan noise by numerical simulation and therefore very fine meshes were required. In both cases the y^+-value was specified to be equal to one.

Pascu et al. (2009) used *ANSYS CFX* and the MRF approach to validate three axial fan designs, each fan being 280 mm in diameter. The blade region consisted of an unstructured tetrahedral mesh which had a ducted inlet length of 3D and a ducted outlet length of 2D. The designed performance was reached in all three cases. It must be noted that for these three cases the computational domain was small due to the size of the fans and the large hub-tip ratios. Therefore, the use a more reliable, but computationally demanding turbulence model such as the k-ω SST turbulence model, (which is recommended to have a y^+ value of approximately 1) could be afforded for the relatively small computational domain.

In some of the literature differences were noticed in the geometry of the numerical domain when compared to the test facilities that were used to validate the numerical simulations. This could be attributed to the large size of the test facilities which require much larger computational domains. In order to use turbulence models such as k-ω SST or LES modelling, these domains are usually simplified to reduce the computational domain size. The effect of different experimental configurations on the performance of the B2-fan was examined by Meyer and Kröger (2001). The fan performance for the configurations in Figure 2.1(a-c) was compared and found to deviate only slightly from each other. A numerical model representing the configuration depicted by Figure 2.1(d), using the ADM approach, was also compared to the experimental results of the type A, BS 848 facility. The numerical data correlated very well with the experimental results within the normal operating range of the fan, although slightly under-predicting the fan shaft power. This suggests that the simplification of numerical models can be seen as a good approximation of a more complex experimental facility.

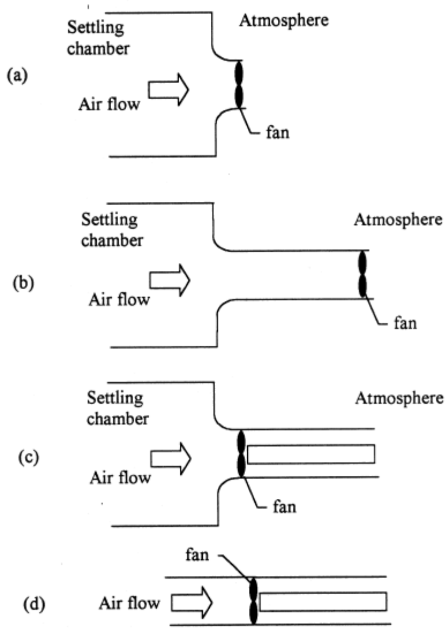

Figure 2.1 - Various test configurations used in the experiments of Meyer and Kröger (2001)

A similar study was conducted by Guedel et al. (2012) in which four different casing configurations were tested for a 630 mm diameter axial fan. The experimental facility adhered to ISO specifications. The four configurations were also simulated using *STAR-CCM+*. The purpose of the simulations was to investigate the feasibility of predicting test performance for axial fans only through numerical simulation. The full computational domain (no periodicity) consisted of an unstructured polyhedral mesh volume (including a large outlet domain) having a total of 14.65 million cells (See Figure 2.2). All simulations used the realizable k-ε turbulence model with a steady state MRF approach. In contrast to the findings of Meyer and Kröger (2001), significant differences in the fan performance of the experimental test results between various configurations were found. Even so, the numerical results correlated well with experimental results, although simulations were only carried out for a very small flow rate region. At lower flow rates, convergence was found to be problematic and in some cases a large number of iterations were required to reach acceptable correlation. Also significant is the large number of cells used in these simulations, already reduced by using polyhedral meshing. Modelling and simulation were performed on two workstations (XEON 2.93 GHz and 128 GB RAM) with 22 parallel processors.

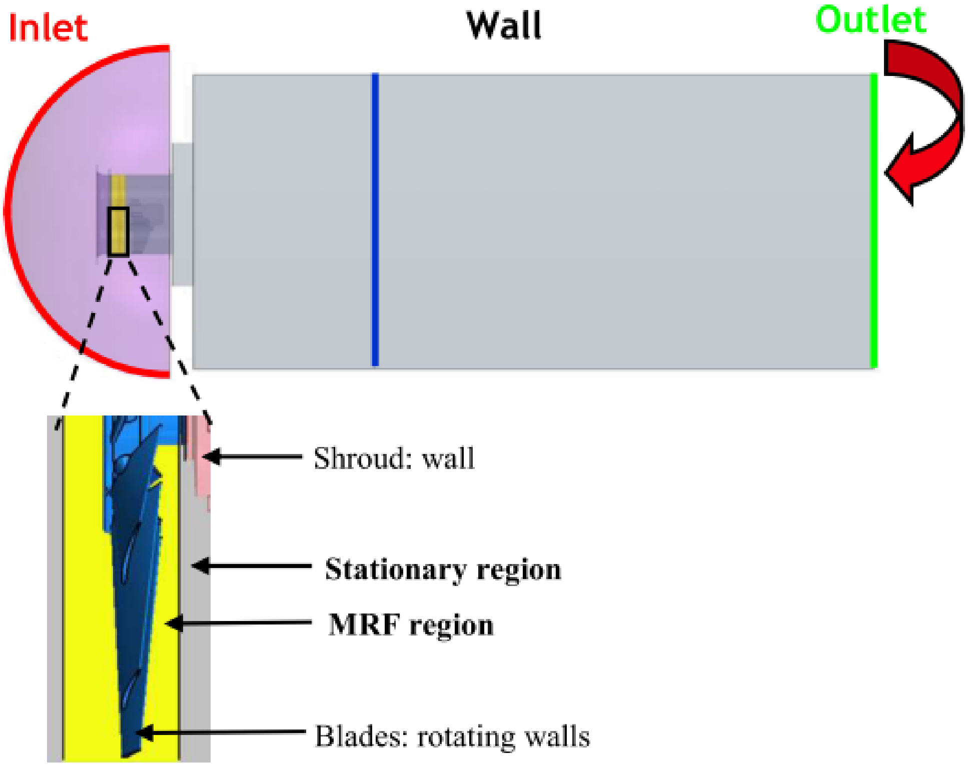

Figure 2.2 - Computational domain for one of the four numerical configurations of Guedel et al. (2012)

A less computationally demanding study was performed by Masi and Lazzaretto (2012) on the numerical simulation and experimental validation of axial fans (D = 630 mm) with specific focus placed on reliable performance with minimal computational time. Masi and Lazzaretto (2012) used polyhedral meshing but stated that it is slightly less accurate than hexahedral meshes and it performs better than tetrahedral meshes. Due to the conformal nature of polyhedral cells, more effective localized meshing is possible. This saves on computational resources. A sensitivity analysis was conducted beforehand on four different computational domains by varying the turbulence model and cell number in each case. It was found that accuracy was largely dependent on cell number rather than turbulence model. Masi and Lazzaretto (2012) consequently simulated the four computational domains, three of them being periodic domains of increasing refinement and varying geometry simulated by the MRF approach and using a two-layered k-ε realizable turbulence model. The two layer k-ε approach (discussed in Chapter 5) refers to the enhanced treatment of the near-wall region. The fourth model, a very coarse non-periodic computational domain, was simulated using the unsteady sliding mesh approach. Experimental tests were carried out on two different outlet configurations, namely a free outlet and a ducted outlet. The correlation between numerical and experimental tests varied from very poor to very good depending on the type of geometry. It was concluded that for very accurate meshing, a large number of cells is required and the counter-acting effect of the over prediction of dissipation at the blade tip together with an idealized geometry produces the most favourable results. Furthermore, a change in the inlet velocity profile is noticed when components such as the bellmouth and an electric motor are considered.

A similar study was also conducted by Jian-Hui and Chun-Xin (2008), which compared the RNG and standard k-ε turbulence model and found good correlation between experimental and numerical data for both turbulence models. Berg and Wikström (2007) modelled a Volvo cooling fan, which was validated by experimental tests and showed very good correlation, specifically for the total-to-static pressure increase. The MRF approach was found to predict the total-to-static pressure increase within 3.5% of the experimental results for the operating region. The fully non-periodic unstructured tetrahedral computational domain was simulated using *ANSYS Fluent* with the standard k-ε turbulence model.

Another study implementing the MRF approach and using the k-ε realizable turbulence model was conducted by Shankaran and Dogruoz (2010). The CAD model used for the numerical simulations was generated by manual measurements of the actual fan. However, simulations were validated by experimental tests and good correlation for the entire flow rate spectrum was found. The computational domain, however, was very small which allows for greater mesh refinement. A similar study was done by Vad et al. (2007). He simulated and tested a large forward skewed axial fan using *ANSYS Fluent* in a periodic computational domain. The standard k-ε turbulence model was used in a domain that had a rather short ducted inlet (mass flow) and outlet (“outflow”). Although correlation between experimental and numerical results was reasonable, the validity thereof may be questioned due to a lack of information regarding their simulations. The same could be said about Amano et al. (2005). Lin and Tsai (2011) also showed good correlation between experimental and numerical values using *ANSYS Fluent* and the standard k-ε turbulence model although there was very little information regarding the details of each simulation.

Zhao et al. (2012) simulated a full scale air-cooled condenser unit using a sliding mesh (unsteady) approach and the standard k-ε turbulence model. The mesh consisted of tetrahedral and hexahedral cells and the computational domain was divided into different regions. Figure 2.3(a-c) shows the mesh and computational domain. The entire mesh consisted of 1.4 million cells and very good correlation between the design specifications’ operating point and the numerical results was shown. Only a single operating point was simulated. No cross-flow analysis was mentioned. To analyse the effect of installing guide vanes at the exit of the air-cooled condenser, another simulation was carried out and a slight decrease in overall performance was noticed (See Figure 2.3(d)).

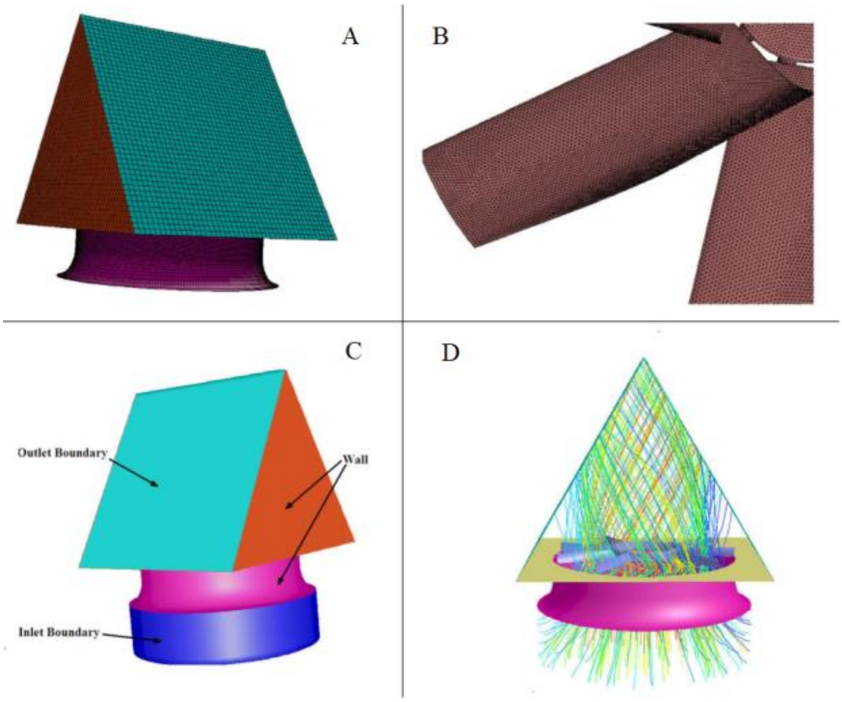

Figure 2.3 - Computational domain of an air-cooled condenser using a sliding mesh approach (Zhao et al., 2012)

Unsteady simulations that make use of the sliding mesh approach and implement computationally expensive techniques such as LES and Detached Eddy Simulations (DES), are considered for a greater number of applications due to the availability of larger computational power (Iwase et al., 2012). De Gennaro and Kuehnelt (2012), however, pointed out that the application of these approaches still does not guarantee reliable results. In studies by Borello et al. (2012), Fernandez Oro et al. (2011) and Iwase et al. (2012), numerical simulations were conducted using LES to predict the unsteady performance of axial fans. The mesh sizes for Borello et al. (2012) and Iwase et al. (2012) were both greater than 13 million cells. Nevertheless, Fernandez Oro et al. (2011), utilized *ANSYS Fluent's* ability to apply the wall-function for larger y^+ values and used LES in a mesh grid which had y^+ values between 30 and 60. This approach dramatically reduced the number of domain cells to approximately 2 million, although accuracy was compromised as a result. This specific LES technique was referred to as the wall modelled LES (WMLES) approach. Good correlation was shown between experimental and numerical results although there was still some deviation prevalent. The order of error was found to be similar in comparative steady state simulations. It must be noted, however, that the unsteady nature of these simulations provided valuable information with regards to vortex formation, flow separation and eddy formation, which is specifically useful in the prediction of fan noise. The computational time in all three studies was lengthy, with the WMLES approach taking 350 hours (~2 weeks) per operating point to reach stable results.

From literature, certain commonalities with regards to numerical simulations were found which can be summarized by the following points:

- The MRF approach can be regarded as the preferred approach in steady state rotational fluid domain simulations. For unsteady simulations, the sliding mesh approach is always used.
- In most cases *ANSYS Fluent* and *CFX* software packages have been used, although the ability of *STAR CCM+* to create polyhedral meshes has made it an attractive alternative.
- The k- ω SST turbulence model proved to be the most accurate and robust approach, although the y^+-value recommendation, resulting in large computational meshes, makes it computationally demanding especially when the fan becomes large (> 600 mm). There was no mention made of the k-ω equation which can probably be attributed to poor performance in the free stream. There was no distinctly preferred k-ε turbulence model, with all three variations showing good results.
- The specified inlet and outlet boundary conditions varied although there was a tendency towards mass flow (velocity) inlet and pressure (static) outlet boundary conditions. Indications of greater accuracy by using non-periodic boundary conditions could not be found, since good correlation was shown for computational domains using periodic boundary conditions.
- Simulation sensitivity towards grid refinement was highlighted by various authors. Most experimental and numerical work was also carried out for small diameter axial fans (< 630 mm).
- The minimum accepted residual value was 10^{-4}.
- Reliable unsteady simulations, using approaches such as LES, requires a large amount of computational resources although accuracy is not necessarily improved. Unsteady simulations were used for the prediction of flow field phenomena (necessary for fan noise analysis).

3 Fan blade data

In Chapter 2 the various approaches for simulating axial fans were discussed. Examples of these approaches include the models that approximate fan performance by implementing mathematical interfaces such as the pressure-jump approach (Van der Spuy et al., 2010) and the actuator disk model (Thiart and von Backström, 1993). Approaches such as the multiple reference frame (MRF), mixing plane and sliding mesh method, however, require a three-dimensional geometric model of the actual axial fan that will be simulated.

If the actual design details for a specific axial fan are known, the process of generating a geometric model is relatively straightforward. However, simulating an axial fan of which there is no design details available is more challenging. The design details in the case of the B2-fan, mentioned in Chapter 1, were known and an accurate geometry was generated. This, however, was not the case for the scaled models of the L1-, L2- and N-fans.

This chapter will discuss the fundamental concepts in generating a numerical model from design data. More importantly, the process of creating an accurate numerical model using three-dimensional scanned data from an actual manufactured axial fan that can be used for numerical simulation purposes, will also be explained.

Figure 3.1 illustrates the nomenclature for two-dimensional blade profile geometries that will be used throughout the rest of the thesis. The definitions can be set out as follows:

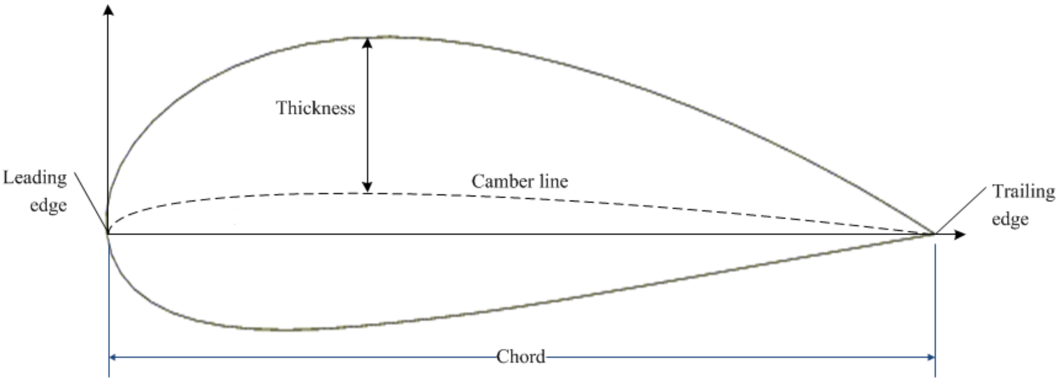

Figure 3.1 - Nomenclature for two-dimensional blade profile geometries

- Leading edge: The foremost position of a blade profile, which theoretically also becomes the stagnation point (local velocity is zero) in a flow field.
- Trailing edge: Rearmost position of a blade profile.
- Chord: The maximum distance of a blade profile measured from the leading to the trailing edge.

• Camber:	The angle between a tangent to the camber line at the leading and trailing edge.
• Camber line:	A curve that can be approximated to be halfway between the top and the bottom surfaces of the blade profile at any percentage chord length (A more detailed definition is given later).
• Thickness:	The distance between the top and bottom surface or between the camber line and a surface.

Furthermore, geometrical models are usually defined by a point cloud. A point cloud consists of numerous points, each point defined inside a Cartesian coordinate system, which can be seen as the foundation of any geometry. Curves can be fitted through the points to further define the geometry and a surface can consequently be generated from multiple curves.

3.1 B-fan

The B2-fan will be referred to as the B-fan in this project. The details of the design process that led to the development of the B2-fan can be found in Bruneau (1994). The focus of this section is to provide a simplified process to generate a three-dimensional model of the B-fan from the two-dimensional blade design theory formulated by Bruneau (1994).

Axial fans (or turbomachinery in general) are often designed using two-dimensional blade element theory. Designs use different variations of two-dimensional aerofoils to meet certain performance requirements for different radial stations (Pascu et al., 2009). The data of these aerofoils are usually given in the form of x and y coordinates normalized in terms of the chord length.

For the numerical model of the B-fan, the original data points were used as given by McGhee and Beasley (1973). The aerofoil, referred to as the NASA GA(W)-1, is defined by x and y coordinates in terms of percentage chord and is specified to have a maximum thickness distribution of 17%. The B-fan, however, was designed with a linear change in thickness from 13% at the hub to 9% at the fan tip. The original data points were therefore multiplied by a thickness distribution factor in order to scale the blade profiles.

In order to define the thickness distribution of the original point data (see Table D.1), a camber line had to be calculated. Generally, the camber line of an aerofoil blade profile is defined by a function,

$$z_c = f(x_c) \tag{3.1}$$

and similarly the thickness distribution is also defined by a function,

$$t = g(x_c) \tag{3.2}$$

with (see Figure 3.2),

$$\left(\frac{z_{t1} - f(x_c)}{x_{t1} - x_c}\right) = -1/\left(\frac{dz_c}{dx_c}\right) \tag{3.3}$$

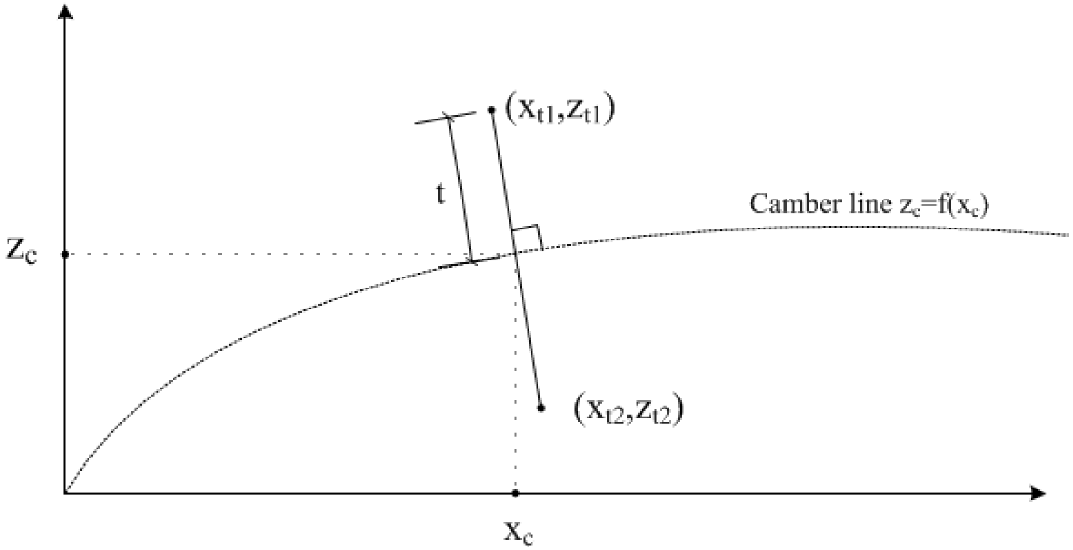

Figure 3.2 - Method of applying the thickness distribution to the camber line

If the camber for a specific aerofoil is small relative to the chord length, as was the case of the B-fan, the approximate chamber line can be defined as,

$$h(x_c) = \frac{z_{t1} + z_{t2}}{2} \tag{3.4}$$

where

$$x_{t1} = x_c$$

The approximated thickness distribution t' can then be defined as,

$$t' = z_{t1} - h(x_c) \tag{3.5}$$

In order to calculate the new aerofoil coordinates for the B-fan, the approximated thickness distribution is scaled by a new thickness distribution t_{scale}, and the z-coordinates for each $h(x_c)$ are determined in the following manner:

$$z_{x_t=x_c} = h(x_c) \mp t'\left(\frac{t_{scale}}{17}\right) \tag{3.6}$$

The numerical B-fan model used for simulation consisted of five equally spaced radial blade profiles from the hub to the tip of the fan (although there can be any number of profiles as may be required). The thickness distribution varies linearly from 13 % at the hub to 9% at the tip. Since the experimental tests by Le Roux (2010) were carried out with a 3 mm tip clearance and a blade root setting angle of 59 degrees (see Figure D.2 for stagger line), the same specifications were used for the geometric model. For further details on how the B-fan was generated and the method explained above, see Appendix D.

3.2 N and L-fans

The three scaled models will be referred to as the L1-fan, L2-fan and N-fan. These fans are scaled versions of large air-cooled condenser axial fans which were provided by the manufacturer of the larger fans. They were to be simulated numerically and compared to experimental test results. No geometry or CAD model, however, was provided and the design specifications of these fans were unknown. To simulate these fans, solid CAD models were required and the scaled models had to be scanned three-dimensionally.

The L1-, L2- and N-fans were scanned using two different 3D scanning techniques to obtain a numerical point cloud of each of the fans' blades. The L1-fan was initially scanned using a non-contact active 3D scanner. However, the scanned data produced by the non-contact scanner was considered to be inaccurate at the leading and trailing edge. A contact 3D scanner was therefore used to scan the L1-, L2- and N-fan, the details of which are set out in the following section.

Theoretically (and in the case of numerical models such as the B-fan), each blade of the manufactured L1, L2 and N-fans would be identical. In reality, however, minor errors in the manufacturing process would result in the blades being slightly different. A visual inspection of the blades showed this to be the case. To accurately quantify these differences, but also determine a representative geometry of each manufactured fan, accurate numerical models of each fan blade was required. It should be noted that axial fans can be assumed to observe periodicity for steady state conditions and therefore the numerical simulations would be carried out with a single fan blade.

All blades of the three scaled fans were scanned, although only one blade was required for simulation purposes. Having the data of all fan blades made it possible to investigate the differences between the various manufactured blades of the same fan. Furthermore, the uncertainty regarding the effect of simulating only a single blade, which does not represent the entire fan, could be investigated. The two scanning approaches used are discussed below.

3.2.1 Non-contact active 3D scanner

A non-contact scanner uses multiple cameras and emitted light to obtain the geometry of an object. The time required for scanning is usually independent of the geometry, but rather a function of the accuracy. For a fairly simplistic geometry such as that of a fan blade, accurate scanning requires very little time.

Post-processing of the scanned data generates a high definition point cloud as shown in Figure 3.3. The non-contact scanner was only used to scan the L1-fan. The large amount of data can be seen as an advantage but results in the post-editing being time consuming.

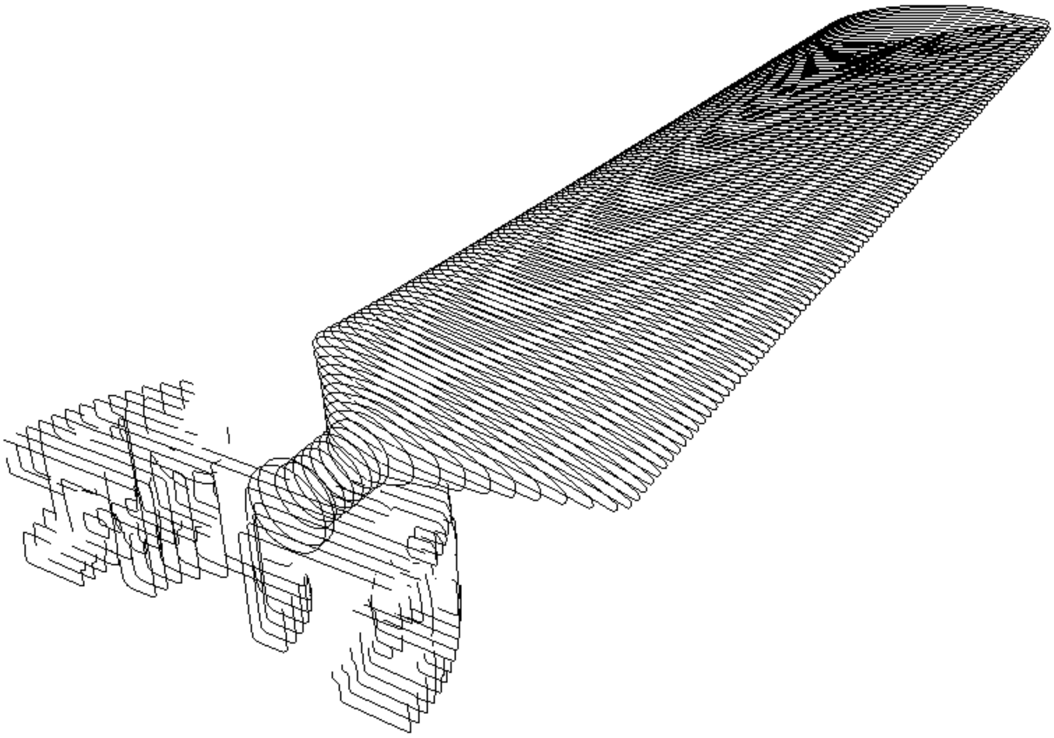

Figure 3.3 - 3D wireframes of the L1-fan scanned by the non-contact scanner

3.2.2 Contact 3D scanner

The contact scanner generates a point cloud of geometry by means of physical touch, which can be unfavourable in some cases where delicate materials are scanned. Contact with the fibre-glass manufactured L1-, L2- and N-fan blades resulted in very accurate point clouds. Each probe started at the trailing edge suction side, following the geometry around to the pressure side which ensured that the leading edge of each radial profile was accurately scanned. This procedure was repeated for multiple radii in the span-wise direction. Due to the nature of the scanning process, however, it proved to be time consuming and expensive. Therefore, only 8 radially spaced blade profile probe traces were carried out for each blade. This resulted in very low density point clouds being generated, as shown in Figure 3.4.

Figure 3.4 - 3D wireframes of the L1-fan scanned by the contact scanner

3.2.3 Post editing

Post-editing of the point clouds was required for both the scanning procedures detailed in sections 3.2.1 and 3.2.2. Due to the functioning of the non-contact scanner each fan blade had to be scanned in two sequences namely the pressure- and suction side. The pressure and suction side data were then merged to form a single point cloud in post-editing. The very small positional changes during scanning of the two sides of each fan blade resulted in inaccurate alignment of the pressure and suction side leading and trailing edges.

At the time of scanning, the effect of the leading and trailing edge on the flow field and overall performance were not known and very accurate modelling thereof was required, hence the decision to rather use the contact scanner. The non-contact scanner data of the L1-fan, however, proved to be consistent with the data from the contact scanner. Although there are differences between the two data sets, the error was initially thought to be larger. This is illustrated in Figure 3.5. The details regarding the differences between the two L-fans can be found in Appendix D. Notice the difference in thickness between the L1- and L2- fan.

Only eight profiles per blade were scanned using the contact scanner. The hub region had a complex geometry in comparison to the rest of the blade and consequently measurements were taken at a radius of 95, 110, 125, 145, 260, 375, 490 and 605 mm.

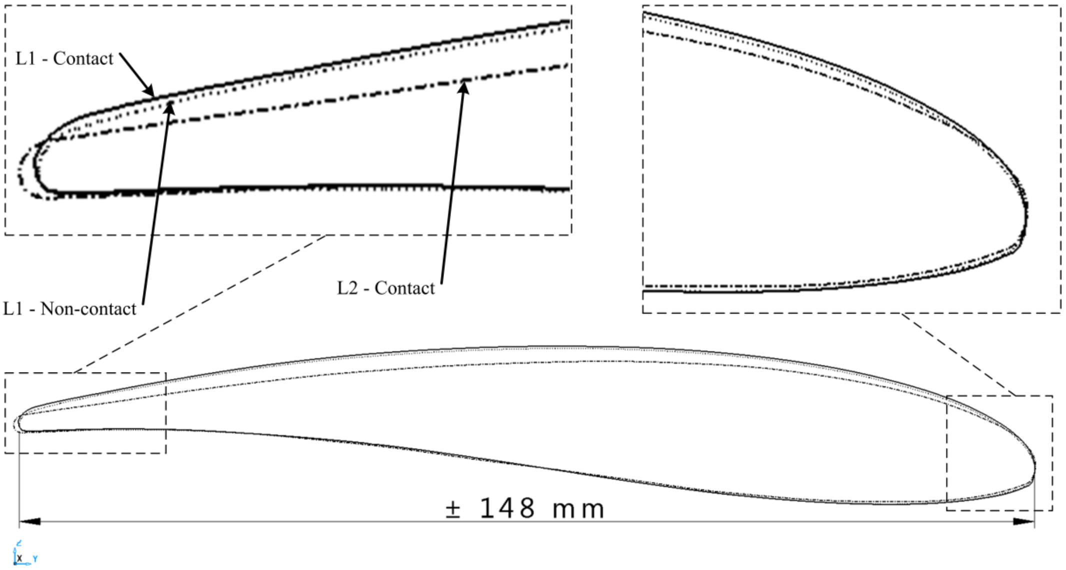

Figure 3.5 - Comparison of the scanned data between the contact scanner and non-contact scanner for the L1-fan

It is usually assumed that all the blades of a fan are identical. Consequently, the simulation of a single fan blade with periodic boundaries is also regarded as a good representation of the entire fan. In the case of the scaled fan models, there were differences between the different fan blades of a particular fan. Therefore the validity of simulating a single fan blade with periodic boundaries to represent an entire fan was questioned. In order to create a representative geometry of the entire fan, an attempt was made to create an average representation of a fan blade by combining all the data of each of the fan blades for a specific fan.

Initial efforts indicated that using the original data, as was specifically the case with the non-contact scanner, was not feasible. The data could not simply be averaged because there was no regular arrangement of the scanned data’s coordinates. The positioning of each fan blade’s geometry also varied with radius, although the position of the hub remained fixed. This resulted in blade profiles of different fan blades not aligning onto each other at specific radii. Consequently, the original data had to be manipulated so that profiles at the same radial distances would align. Furthermore, since no information regarding the stacking line, camber line, stagger angle, chord line or thickness distribution were available, these parameters needed to be approximated accurately.

Considering all the approximations and manipulation of the sets of fan blade data, the result of the representative blade did not prove to be accurate enough. It was found that within the scope of the project, it was not possible to determine an accurate average representative blade for numerical simulation. This could specifically be attributed to the unknown stagger angle and stacking line which could not be averaged. The process of approximating these parameters and calculating an average blade from multiple fan blades is discussed in more detail in Appendix D.

One of the main objectives, as set out in Chapter 1, was to simulate these axial fans rather than investigate the effects of manufacturing error on performance. Therefore simulations were carried out using a single fan blade for each axial fan. A small comparative study was, however, done to compare the fan blade geometry of the L2-fan and L1-fan (see Figure D.5.). Due to the contact scanner's ability to measure the geometry of each blade more accurately, the numerical models were created using the measured data from the contact scanner.

ANSYS TurboGrid (structured mesh turbomachinery software) was used to create the mesh of each fan. To generate a computational mesh for each fan, the geometry of the fan is imported through a *.crv*-file. A *.crv*-file is a text file, representing a point cloud which contains multiple layers. A layer is defined by x, y and z coordinates of a specified radial blade profiles. A *.crv*-file can be created by the user by specifying the coordinate points or by using *ANSYS BladeModeler*. *ANSYS BladeModeler* requires a CAD model (ex. *.x_t*, *.step*, *.iges*) of a fan blade to generates a *.crv*-file.

In the case of the B-fan, the numerical data points were neatly arranged from the hub to the fan tip, which was ideal for lofting surfaces of point cloud geometries. The relative complexity of the hub region of the other scaled model fans and a large amount of data points resulted in complications with regards to surface lofting. *ANSYS TurboGrid* had difficulty in lofting between the hub region blade profiles of the scaled fans while maintaining the correct geometry, due to the limited number of blade profiles (layers) and it primarily being a meshing software program. Therefore, the original blade profiles were not sufficient to create a *.crv*-file. However, *ANSYS BladeModeler* allows the user to specify the position of multiple layers on an imported fan geometry (CAD model) and increased number of layers in the hub region would resolve the surface lofting problem encountered in *ANSYS TurboGrid*. A solid model, generated in a specialized CAD environment, was therefore required.

In the context of creating a solid model with smooth surfaces, the accurate representation of the actual model resulted in some modelling difficulties. *Delcam Powershape* was used to loft the scanned data profiles and create an *.x_t*-file (*parasolid* file). *Powershape* is specialized reverse engineering software and is ideal for the purpose of post-processing scanned three-dimensional data.

In creating a solid model, the lofting procedure creates a surface fit through a selection of profiles (layers) that define the shape of the geometry in a three-dimensional environment. The geometry of each profile plays a major part in the outcome of the solid model surface. The high accuracy of the contact scanner profiles, however, resulted in lofting being impractical. Ideally, profiles of the same lofting sequence should have the same number of data points, regularly arranged with respect to the other data points in a two-dimensional plane. Initial lofting of the original data resulted in a very uneven surface finish, especially at the leading and trailing edges. The outcome of the finish at the trailing edge of the lofted L2-fan can be seen in Figure 3.6. The unevenness was due to the actual manufactured models' surfaces containing areas of unevenness. The effect of this unevenness was unfortunately magnified by the lofting procedure. It was found that for the purposes of meshing around the blade surface, having a smoother surface resulted in a much better and acceptable mesh. Therefore, the data points had to be edited and this meant that some of the detail of each profile would be lost.

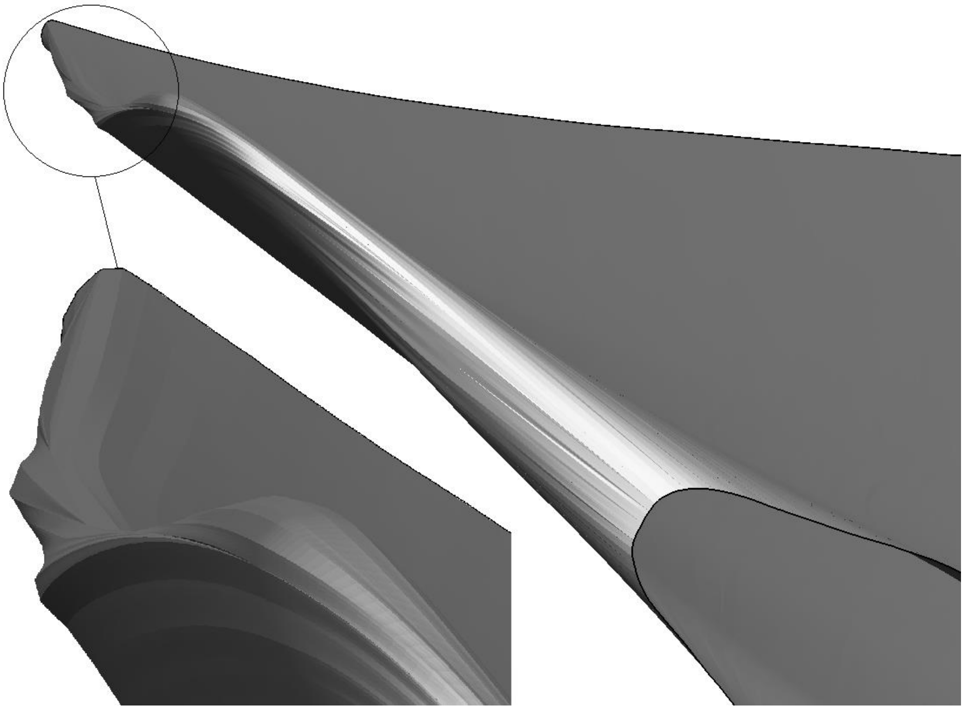

Figure 3.6 - Trailing edge surface of the L2-fan, lofting the original data layers.

In order to simplify, but still try to maintain the original geometry of the fan blade, each profile was edited individually. The purpose of the simplification was to smooth out the existing geometry curve of each blade profile. In order to accomplish this, the number of data points defining any given blade profile had to be reduced. Having fewer, but strategically placed data points positioned on the original curve, resulted in a smoother curve of the same geometry. The effect of reducing the number of data points on the leading edge is shown in Figure 3.7. It is important to note the scale of the changes that were made. The largest deviation, only 80 microns, from the original curve's leading edge is shown in Figure 3.7.

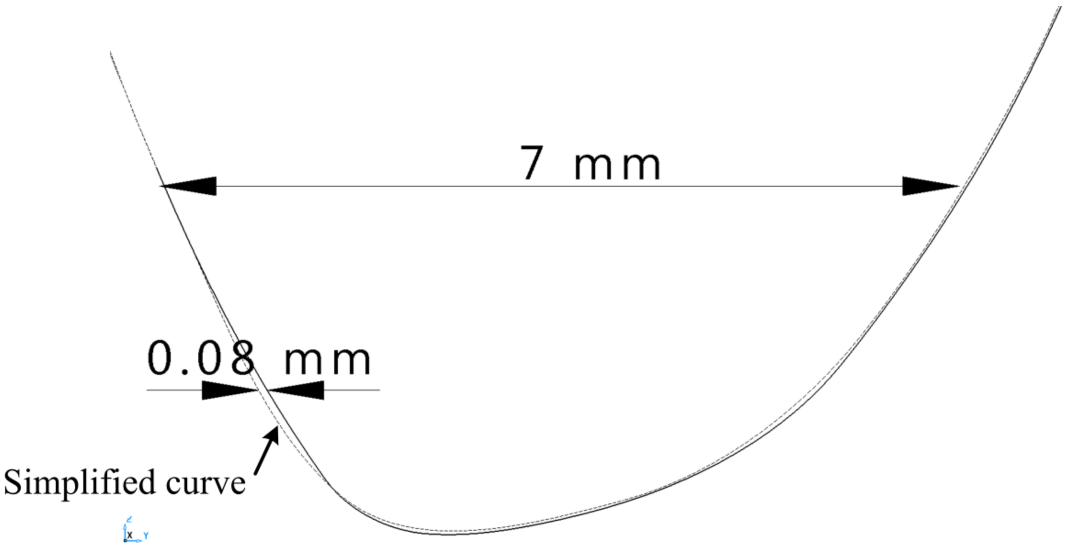

Figure 3.7 - Comparison between the original scanned data curve and the simplified curve

The simplification procedure for each profile was divided into four sub-divisions: The leading edge, trailing edge, suction side and pressure side. The same number of data points was used for each of the sub-divisions of each profile. Once a curve had been simplified it was possible to increase the number of data points defining the simplified curve for the purposes of surface lofting. Having more data points increased the accuracy of surface lofting. It is important to note that decreasing the number of data points changed (simplified) the curve geometry while adding data points had no effect.

Careful simplification, as explained above, resulted in much smoother surfaces of the lofted solid models. This was particularly noticeable at the leading and trailing edges of a model. The hub region was also characterised by subtle changes in geometry. Due to the fact that the contact scanner was not able to scan at the fan tip (r = 620 mm), the fan blade surface was extrapolated to a value greater than 625 mm to take the tip clearance into account. Finally, the coordinate system for each of the solid models was changed to correspond to the required direction for each axis in *ANSYS Turbogrid.* The position of the origin was also shifted to where the stacking line (x-axis) and rotating axis intersect (z-axis).

In Figure 3.8 and Figure 3.9 the solid model geometries of the L2- and N-fan blades are shown. Further details on how the mesh was created from these solid models are discussed in later chapters. It must be emphasized that importing data points through a user-specified *.crv*-file into *ANSYS TurboGrid* must be the first priority. This ensures that minimal round-off errors are introduced between the various software programs. This, however, is only practical if the numerical data was generated using the design specifications of a fan (as was the case with the B-fan). Simply lofting the original three-dimensional data from scanned geometry could result in an inaccurate solid model due to the limitations of the lofting procedure and the non-uniform arrangement of the data points.

Figure 3.8 - Numerical solid model of the L2-fan

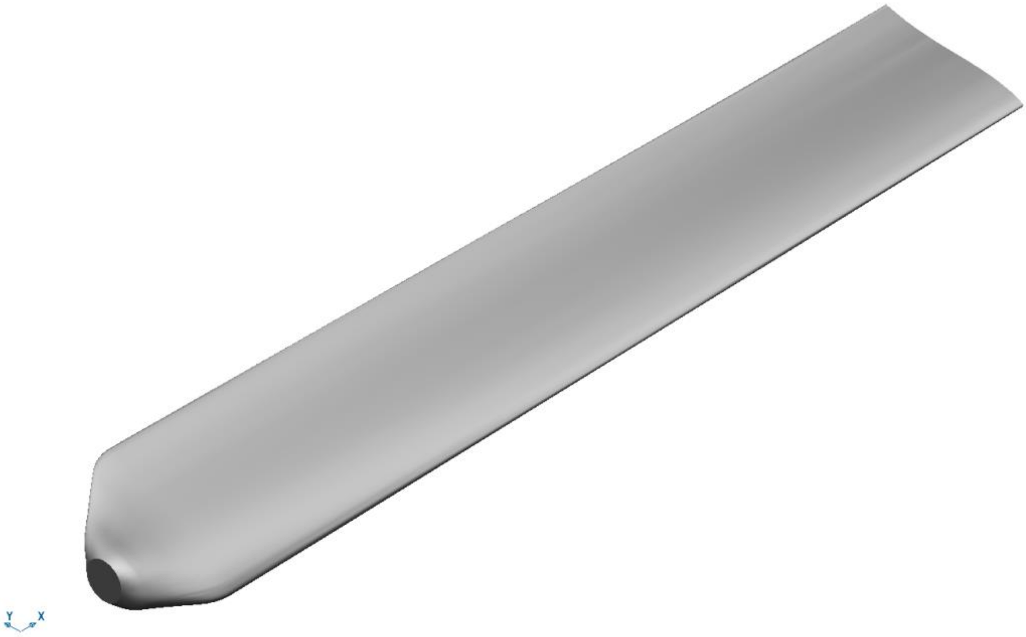

Figure 3.9 - Numerical solid model of the N-fan

3.2.4 Blade-setting angle

The blade setting angles of the solid models had to be adjusted to match the experimentally tested angles. It was crucial that the definition of the experimentally tested and numerically simulated blade-setting angles be exactly the same. In the case of the B-fan, the blade setting angle could be adjusted by altering the design values. However, this was not possible with the scanned data although the physical design, blade-setting angle and method of specifying the angles were known.

Figure 3.10 below illustrates how the blade-setting angle should be determined experimentally. Measuring the blade-setting angle 5 mm from the blade tip, as specified by the manufacturer, was difficult due to the poorly defined fan blade tips. For experimental purposes, the position of measuring the blade-setting angle was changed to 25 mm from the fan tip (595 mm from the axis of rotation). This ensured repeatable accuracy when setting the angles. Further details on the blade-setting angle can be found in Chapter 4.

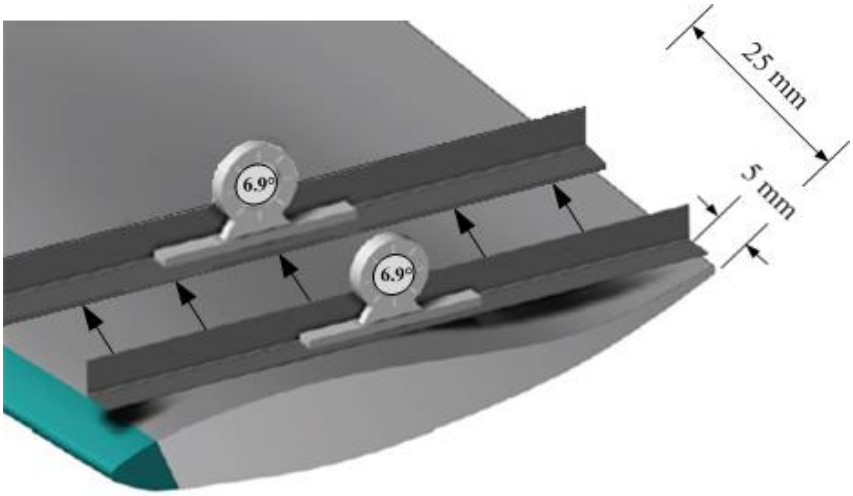

Figure 3.10 - Different measuring positions of the protractor

Because there were no numerical data points available at a radius of 595 mm, the lofted solid model surface was used to adjust the blade-setting angle. A straight tangent line was fitted to the blade surface of a numerical model at the specified radius. The coordinates of the intersection between the blade surface and the straight line was used to calculate the gradient of the line that corresponds to the blade-setting angle. The desired blade-setting angle could be found by rotating the entire solid model around the stacking line until the gradient of the intersection coordinates were equal to the desired blade-setting angle. Once the blade-setting angle was adjusted the fan tip was shortened to the desired length.

4 Experimental work

Testing was carried out on the three scaled model fans, namely the L1-, L2- and N-fan. In order to validate the numerical simulations of the B-fan, data presented by both Stinnes (1998) and Le Roux (2010), who carried out experiments on the B-fan separately, would be used. No experiments were performed on the B-fan during this study.

The purpose of the experimental testing of the axial fans was primarily to determine the aerodynamic performance of the various fans. This includes the total-to-static pressure increase across the fan, the torque induced by the fan (measured at the shaft) and determining the fan static efficiency. These parameters are presented in relation to the volume flow rate, which is determined by measuring the pressure drop over the inlet bellmouth. Having determined the performance of the various fans, the fan scaling laws were used to compare the scale models with their full scale equivalents. Another important part of the experimental tests was the use of the data for the purposes of validating the numerical simulations. Consequently, besides ensuring that the experimental tests were repeatable, attention to detail and accuracy were necessary, especially during calibration of the measuring devices.

4.1 L-fans

The two L-fans, referred to as the L1-fan and L2-fan (Figure 4.1), are similar in geometry and shape and have exactly the same outer and inner diameters. At a glance the chord lengths also seem similar, although during closer inspection clear differences are noticeable in the thickness distribution, blade weight and surface finish. The blades of the L1-fan were noticeably heavier, with a larger thickness distribution.

Both fans have 8 blades with an outer rotor diameter of 1 240 mm and a hub/tip ratio of 0.135. A comparative study on the geometric differences between the L1- and L2-fan is discussed in Appendix D. Figure D.5(a-b) indicates that there is very little variation in the chord length with change in radii in both cases. The chord length for most of the blade span is between 145-150 mm. The hub geometry for both fans is identical and consists of two totally separate parts held together by eight bolts and nuts. The hub was supplied originally with a shaft and key configuration but was customized in order to accommodate a taper lock bolt-on-hub. The taper lock configuration resulted in easy fastening and removal of the fan during testing. This alteration was made to all of the fans that were tested.

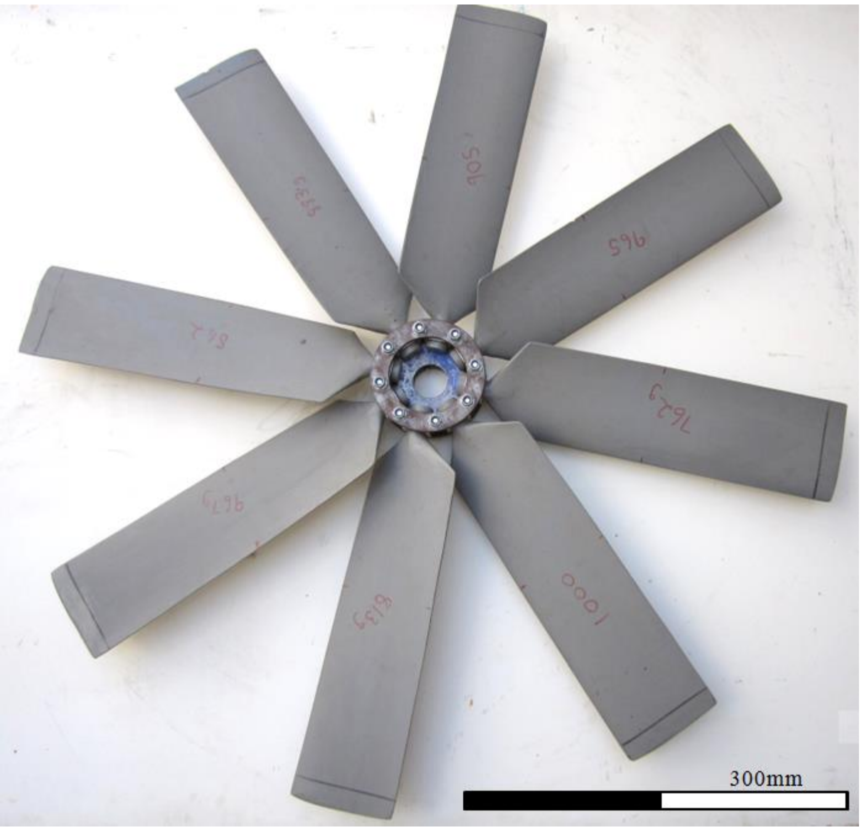

Figure 4.1 - Tested L2-fan

The L1-fan had a smooth surface finish in contrast to the matt surface finish of the L2-fan. The L2-fan's blades weighed between 762 g and 1000 g while the L1-fan's blades all weighed close to 1500 g each.

4.2 N-fan

The N-fan has the same outer diameter and hub/tip ratio as the L-fans, but has 9 blades with a lower solidity. The N-fan is characterised by a much smaller chord length which has little radial variation, as can be seen from Figure 4.2. The hub geometry, as mentioned in the case of the L-fans, had to be altered from its original design. However, having nine blades, a slightly different configuration was required. In comparison with the L-fans, the N-fan's hub was much heavier. This resulted in further changes to the hub geometry in order to reduce its weight.

The surface finish of the N-fan resembled that of the L2-fan and the weight difference between blades varied little (550-600 g). The N-fan's small chord length and thin thickness distribution resulted in the fan blades being slightly flexible.

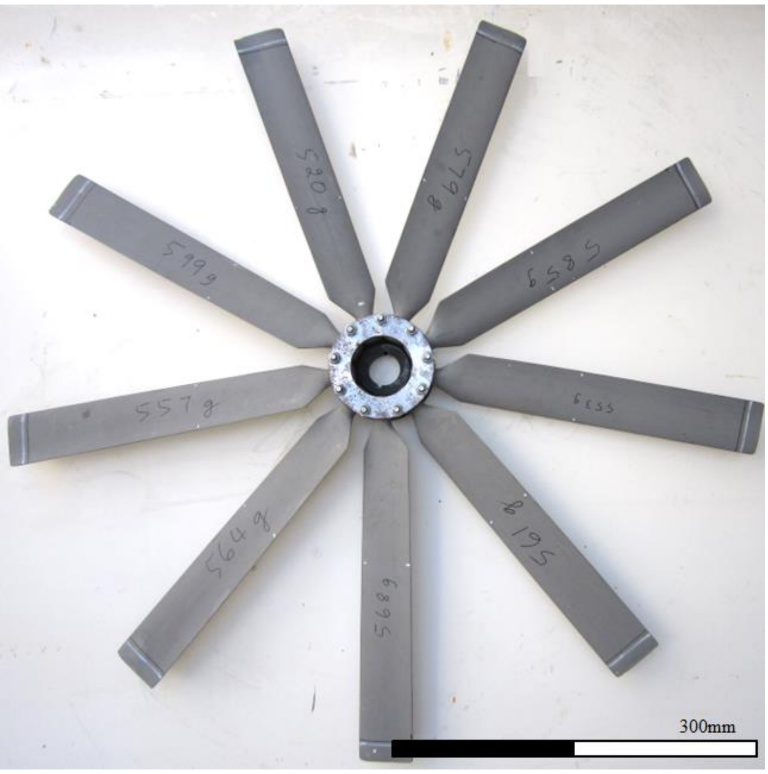

Figure 4.2 - Tested N-fan

4.3 Setup parameters

Axial fans are characterised by the pressure increase across a fan, the power it consumes and the overall efficiency of the fan. These parameters are given in relation to the volume flow rate passing through the fan. For a type A configuration (open inlet and open outlet) the pressure increase is defined by the difference between the total inlet pressure and static outlet pressure. The power used to drive the fan is measured by determining the torque on the fan shaft. The fan efficiency is an indication of how effectively the fan translates the power that is consumed into a pressure increase. To determine these characteristics for a wide operating range of a specific fan, the blade setting angles, volume flow rate and rotational speed for each fan was varied.

As mentioned earlier, the supplied fans were scaled models of industrial size fans that are used for air-cooled steam condensers. To compare a full scale model of any nature with its scaled model, one must ensure that the operating conditions for both in relative terms remain the same. Although the design operating conditions for the small scale model fans were unknown, these operating conditions were determined by means of dimensional analysis. Dimensional analysis is used to establish similarity between the actual and scale model. The Reynolds number is the most useful dimensionless parameter for finding similarities in conditions in scaled models. The known details of the actual and small scale fans are given in Table 4.1.

Table 4.1 - Full and small scale fan specifications

	Large scale (L-fan)	Large scale (N-fan)	Small scale (L1, L2, N)
D_o	34 ft (10 363 mm)	34 ft (10 363 mm)	1 240 mm
D_i	-	-	169 mm
Fan speed			-
Design static pressure			-
Design volume flow rate			-
Blade tip chord length			-
*	$\rho = 1.071\ \frac{kg}{m^3},\quad \mu \sim 1.8e^{-5}\ \frac{kg}{ms}$	$\rho = 0.999\ \frac{kg}{m^3},\quad \mu \sim 1.8e^{-5}\ \frac{kg}{ms}$	

The Reynolds numbers of the full scale fans, based on the fan blade chord length, was calculated using Equation 4.1:

$$Re = \frac{\rho\, V_{tip}\, L_{chord}}{\mu} \tag{4.1}$$

In order to satisfy dimensional similarity the Reynolds numbers of both fans are required to be identical. From the formulation above it is clear that in order to keep the Reynolds numbers the same, the tip speed of the small scale fan will have to be significantly larger due to its smaller blade chord length. The chord length of the small scale fans can be approximated using the scale factor, $\frac{10.363}{1.24}$. Consequently the tip speed of the small scale fan is calculated to be approximately 4000 rpm, which is impractically high.

To determine feasible operating conditions for the scaled fans, the obvious route to follow would be to simply maximize the rotational speed. This would minimize the difference between the Reynolds numbers of the full and scaled fan models. However, there are safety requirements which limit the rotational blade speed. By fixing the non-dimensionalised flow coefficient, calculated as follows,

$$\phi = \frac{C_a}{U_{tip}} \tag{4.2}$$

and therefore keeping the velocity triangles the same in both cases, an acceptable and comparable rotational speed can be determined. The blade tip velocity of the full scale fan is approximately 60 m/s. The required rotational speed for the small scale model fans was consequently calculated to be 900 rpm. The fan supplier also suggested that the fans should not be tested at rotational speeds above 900 rpm. According to Kroger (1998) fans which are much larger than the test model can deviate from the predicted performance of the model. This is due to the fact that the fan scaling laws do not take into account frictional effects if the Reynolds numbers are not identical.

4.3.1 Blade setting angles

Geometric similarity requires the small scale blade setting angles to resemble that of the large scale fan. The L-fans' design angle was known to be 6.9°, measured as shown below in Figure 4.3, whereas the N-fan's design blade-setting angle was 11.6°. For the purposes of determining the performance for a wider operating range in each case, five different angles were tested. Tests were conducted at the design angle and two setting angles above and below the design angle, at one (L-fans) or two (N-fan) degree increments. The method for setting the blade angle was specified in terms of the large scale fan. The blade setting angle is specified to be measured 50 mm from the large scale fan's blade tip. Determining the angle on the small scale fan according to the method mentioned above proved to be impractical due to the scale factor which reduced the distance to only 5 mm.

The problem was aggravated by poor definition at the fan tip. To ensure that the blade setting angles were measured accurately for each change in angle, a fixed distance, further away from the tip, was defined. The angles were measured using a digital protractor (see insert in Figure 4.3). The blade angles were adjusted by placing the hub, with the blades already installed, on a level table. The necessary hub nuts were loosened to adjust the angle for each blade. All nuts were tightened thoroughly after initial adjustment and the blade setting angle of each blade was measured again. Setting all the angles at precisely the same value proved to be very difficult. A tolerance of 0.2 degrees was allowed for all blade setting angles. Slight changes in the blade angles during operation were noticed when failing to tighten the bolt and nut configuration properly.

Figure 4.3 - Measuring the blade-setting angle

4.3.2 Positioning and tip clearance

According to Le Roux (2010), who carried out experiments on the B-fan using the same facility, no noticeable change in performance was found by changing the axial position of the fan inside the shroud. All fans were nevertheless positioned at the centre of the shroud. None of the experimental fans' designs allowed for a change in tip clearance and consequently the tip clearance was fixed for all fans. The tip clearance in all cases was 5 mm although small differences (±1 mm) were found due to differences between the manufactured parts.

4.3.3 Fan Operation

As stated previously, all three fans were to be tested at 900 rpm. During start-up, however, it was noticed that the supplied fans were not balanced well enough to enable rotation at such high speeds. The fans could not be dynamically balanced due to the size and geometry of the fans and an attempt was made to improve the balancing of the fans by imposing a static momentum balance on the blades. Each blade was weighed using a mass scale and the lowest force resultant was found by changing the arrangement of the blades by means of an algorithm written in *Scilab* (see Appendix F). This procedure, in the case of the L2-fan, improved the initial static resultant of 122 N to only 7 N. This enabled the fan to rotate at much higher speeds. However, the improvements mentioned above were not sufficient to enable rotation at 900 rpm. Improvements to the test facility reduced vibration on the entire system as discussed further in Appendix A. This allowed the tests to be performed at higher rotational speeds. To examine the validity of the fan scaling laws, certain blade setting angles were tested at various rotational speeds. The data of the different rotational speeds would then all be scaled to the same rotational speed for comparison.

4.4 Test Facility

All tests carried out on the N and L-fans were conducted at the large fan test facility situated at Stellenbosch University, Department of Mechanical & Mechatronic Engineering. The facility is situated outdoors and therefore weather conditions such as wind and fluctuating temperatures can influence the results and the repeatability of the tests. The specifications of the facility for axial flow fans are based on the type A, BS 848 standards. The type A setup specifies a free open inlet to open outlet configuration. The design and commissioning of the facility is discussed in detail by Venter (1990) and further details on the test procedure and the instrumentation used during the tests can be found in Appendix A. The main features of the facility as shown Figure 4.4 in are:

1. A calibrated bellmouth inlet ($D_{bellmouth}$ = 1008 mm) is used to measure the volume flow rate through the fan. Because the test tunnel is 1500 mm shorter than required by the BS 848 standards the compound coefficient ($\alpha\varepsilon$) was validated to be 0.9803 for this particular facility (Stinnes, 1998).

2. A throttle unit with flow straighteners that is used to manually adjust the volume flow rate through the test facility.

3. A 6 blade, 7.5 kW, axial flow booster fan with variable speed drive to overcome the flow resistance induced by the front tunnel-end of the facility. The booster fan specifically enables measurements to be taken at low pressure rise, high volume flow rate operating points.

4. A flow straightener to remove swirling flows and eddies induced into the flow field by the booster fan.

5. Guide vanes and three mesh screens of increasing fineness are situated inside the settling chamber (6) to ensure a uniform velocity profile and distribution of air entering the inlet of the fan.

6. A settling chamber (4 m high, 4 m wide and 7 m long) to slow down the inlet flow velocity into the fan to such an extent that the dynamic pressure at the fan inlet is considered to be negligible if the velocity is smaller than 2 m/s (BS 848 standards, 1997). The large dimensions of the settling chamber relative to the test fan diameter ensure that the fan inlet is considered to be "open".

7. The test fan(s) with diameter of 1240 mm situated inside the bellmouth.

8. The test fan propulsion unit. The fan is driven by a 10 kW motor controlled by a variable speed drive. For the purposes of the tests, an altered 3-belt drive system to reduce the rotational speed of the fan shaft had to be installed. The torque transducer is positioned between the fan and the pulley at the end of the drive shaft.

4.4.1 Equipment

The equipment used to measure the performance characteristics of all the fans are as follows. For a detailed discussion see Appendix A.

Pressure: HBM PD1 inductive differential transducer. (range : ±1000 Pa)

Torque: HBM T2 torque transducer with slip-ring (500 Nm)
T22 torque transducer with no-slip ring (100 Nm)

Speed: Turck Inductive proximity sensor (0-10 V)

Other: A thermometer was placed inside the settling chamber to measure the air temperature. Atmospheric pressure was measured using a barometer and information from the engineering faculty's local weather station. Variable speed drives were used to control the rotational speed of the fans.

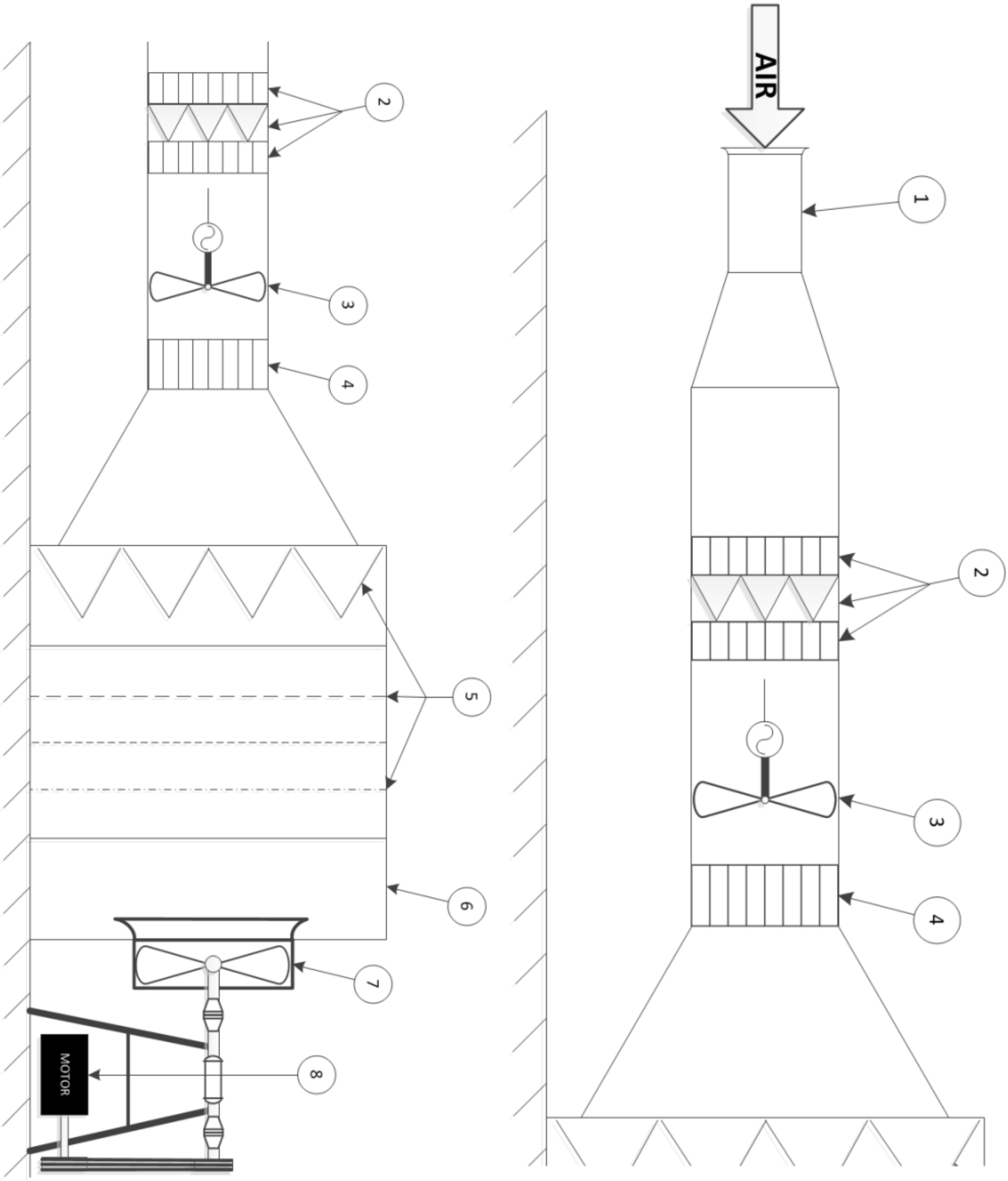

Figure 4.4 - BS 848 test facility

5 Numerical modelling

In Chapter 2 it was shown that a number of studies on the simulation of axial fans have been conducted. Most of these studies indicated that the procedure for simulating an axial fan is thought to be well understood. However, there were significant differences between the experimental and numerical results found in most studies mentioned in Chapter 2. Furthermore, the accurate simulation of fans at low-Reynolds numbers has been found to be largely overlooked in literature. This thesis focussed on investigating computational resource friendly, but accurate, ways of simulating axial fans over their full operating range. This included examining various turbulence models and the effect of simplifying (size reduction) the geometry of a domain. All fans were simulated assuming steady state conditions using various Reynolds averaged Navier-Stokes (RANS) k-ε turbulence models. The numerical results are compared to the experimental data presented in section 6.2.

As previously stated a thesis on the simulation of axial fans was performed at Stellenbosch University by Le Roux (2010) using *NUMECA FineTurbo* numerical software. *NUMECA Fine/Turbo* is primarily designed for high pressure ratio and high flow rate turbomachinery applications. Le Roux (2010) found that *NUMECA Fine/Turbo* could not successfully attain the required convergence levels in the lower flow rate region found in axial flow fans and *ANSYS Workbench* version 14.0 was selected for use in this thesis. *ANSYS Workbench* includes the geometrical CAD and basic meshing software (*ANSYS DesignModeler*, *ANSYS Meshing*), the turbomachinery meshing software (ANSYS *TurboGrid*) for the fan passage and the solver (ANSYS *Fluent*).

Computational resources for modelling purposes, which include mesh generation and post-editing, used a 2.5 GHz quad-core processing unit and 8GB RAM. In general a gigabyte of RAM was required for every million cells that were meshed. In some cases three separate meshes were combined into a single case file which increased the required computational memory. This consequently limited the number of cells for each separate zone to a degree. The solving of a case file, however, was carried out on a computational cluster with a capability of up to 16 CPU units per case.

Three fans were simulated for the purposes of the study namely: the B-fan, N-fan and L2-fan. Although no experimental testing was carried out on the B-fan it was regarded as an ideal starting point for the numerical investigation due to the fact that previous numerical work had already been done on the B-fan by Le Roux (2010). The hub region of the B-fan rotor is also known to have little fluid separation for a wide range of flow conditions.

5.1 Computational flow modelling

The principles of conservation of mass, energy and momentum are used to derive the fundamental equations necessary to describe the behaviour of any fluid. The governing equations relevant to this thesis, using tensor notation, are:

- The **continuity equation**

$$\frac{\partial \rho}{\partial t} + \frac{\partial}{\partial x_j}(\rho u_j) = S_m \qquad \textbf{(5.1)}$$

where S_m is the mass added source term (ANSYS Fluent, 2011). For incompressible flow the time-dependent density term can be neglected.

- The **momentum equation** (Navier-Stokes formulation) for the x-direction

$$\rho\left(\frac{\partial u_i}{\partial t} + u_j \frac{\partial u_i}{\partial x_j}\right) = \frac{\partial \sigma_{ij}}{\partial x_j} + X_i \qquad \textbf{(5.2)}$$

where X_i represents the body forces and σ_{ij} is defined as

$$\sigma_{ij} = -p\delta_{ij} + 2\,\mu\, S_{ij} - \frac{2}{3}\mu\, S_{kk}\,\delta_{ij} \qquad \textbf{(5.3)}$$

and

$$S_{ij} = \frac{1}{2}\left(\frac{\partial u_i}{\partial x_j} + \frac{\partial u_j}{\partial x_i}\right) \qquad \textbf{(5.4)}$$

The derivations for the governing equations of state can be found in Kays et al. (2004) and ANSYS Fluent (2011). Because of the incompressible nature of the flow it is assumed that solving the energy equation will have no significant effect on the solution. The first term on the left hand side of Equation 5.2, represents the time dependent nature of the velocity that can be found in a flow field. The flow is considered steady and the time dependent term can be neglected. This is however not entirely true for turbulent flow. Although the average state of the flow field can be considered steady, the flow properties for turbulent flow vary in an unpredictable manner. These fluctuations are characterized by three-dimensional variation which includes rotational structures called turbulent eddies that have a wide range of characteristic lengths and velocities. Small eddies are dominated by viscous effects and can be regarded as isotropic. The dominant effect of inertia forces in large eddies on the other hand cause its behaviour to be largely anisotropic (fluctuations are different for different directions). A ‘large-eddy’ Reynolds number can be defined, based on the characteristic length (ι) and velocity (ϑ) of larger eddies which is used in turbulence modelling (Versteeg and Malalasekera, 2007).

The most accurate approach in solving turbulent flow is by Direct Numerical Simulation (DNS) which uses the instantaneous continuity equation and the three Navier-Stokes equations to form a closed set of equations with unknowns u, v, w and ρ. By using very fine spatial discretization DNS develops a transient solution with sufficient time steps in order to solve the small turbulent eddies and fast fluctuations (Versteeg and Malalasekera, 2007). For further reading on DNS see Moin and Mahesh (1998). Solving the flow field numerically for turbulent flow by direct use of the governing equations, such as DNS, is very resource intensive and therefore alternative solving methodologies are available which facilitate numerical solving by less computational demanding procedures.

5.1.1 Turbulence modelling

There are two major approaches used to solve turbulent flow other than DNS. The first approach applies a time-averaging procedure to the governing equations and decomposition of the instantaneous flow into a mean and fluctuating variable. This substitution leads to an extra term which requires at least another equation to establish mathematical closure. The universal behaviour of all eddies are also modelled by a single turbulence model. Due to the difference in behaviour of small and large eddies, especially in a low-Reynolds number flow regime, large errors in solutions can occur (Versteeg and Malalasekera, 2007).The second approach solves the larger turbulent eddies with a time-dependent simulation using spatial filters to separate the larger eddies from the small eddies. This is referred to as Large Eddie Simulations (LES). Further details on LES can be found in Versteeg and Malalasekera (2007) and Tu et al. (2008). Although LES takes the anisotropic nature of large eddies into account, it is important to note that LES does not guarantee improved results for all cases.

The Reynolds average Navier-Stokes equations

The random velocity fluctuations found in turbulent flow can be decomposed into a mean velocity $(\overline{u})$ and fluctuating component(u'). The instantaneous velocity is then defined as

$$u(t) = \overline{u} + u'(t) \tag{5.5}$$

Substituting Equation 5.5 into each of the governing equations and applying the principle of time-averaging (as described in Kays et al., 2004) results in a set of time averaged equations. For the x_i momentum equation this will give:

$$\frac{\partial}{\partial x_j}\left(\rho\overline{u}_j\overline{u}_i + \rho\overline{u_j'u_i'}\right) = \frac{\partial}{\partial x_j}\left(\overline{\sigma}_{ij}\right) + \overline{X}_i \tag{5.6}$$

Equation 5.6 is referred to as the Reynolds averaged Navier-Stokes (RANS). The viscous stress tensor and fluctuating convective term, referred to as the turbulent stress tensor, can be coupled and therefore:

$$\frac{\partial}{\partial x_j}\left(\rho \overline{u}_j \overline{u}_i\right) = -\frac{\partial \overline{P}}{\partial x} + \frac{\partial}{\partial x_j}\left(\overline{\tau}_{ij} - \rho \overline{u_j' u_i'}\right) + \overline{X}_i \tag{5.7}$$

Although the mathematically derived turbulent stress tensor is highly nonlinear and reflects the time-dependent fluctuations found in turbulent flow it can still be quantified experimentally. The tensor consists of nine terms for the x, y and z direction although symmetry reduces the number to six (Kays et al., 2004). These stress terms are called the Reynolds stresses. Mathematical closure, however, has become impossible due to the addition of the turbulent stress tensor and therefore another equation is required. These turbulent stress terms are modelled using turbulence models (Versteeg and Malalasekera, 2007).

The Reynolds stresses which originate from the RANS approach need to be modelled appropriately. The first method of modelling the turbulent stress tensor is to solve each Reynolds stress separately. This is referred to as the Reynolds stress model (RSM). This model requires an equation for each term in the tensor (six terms for 3D flow, four terms for 2D flow) and a scale-determining equation (ANSYS Fluent, 2011). Modelling each Reynolds stress separately results in accurate modelling of the flow although an additional seven equations increases the required computational resources for a three-dimensional simulation greatly.

The Boussinesq approach

Another, more common, method is the Boussinesq approach. The additional $-\rho\overline{u_j' u_i'}$ term in Equation 5.7 is defined as a shear stress, which is based on the assumption that there is an analogy between the viscous shear stress and turbulent shear stress. Based on the formulation,

$$\tau_{xy} = \tau_{yx} = \mu\left(\frac{\partial u}{\partial y} + \frac{\partial v}{\partial x}\right) \tag{5.8}$$

Boussinesq proposed that the turbulent stress tensor is proportional to the mean velocity gradient. The Reynolds stresses are therefore related to the velocity gradient as shown below in tensor notation:

$$-\rho\,\overline{u_j' u_i'} = \mu_t\left(\frac{\partial u_i}{\partial x_j} + \frac{\partial u_j}{\partial x_i}\right) - \frac{2}{3}\left(\rho k + \mu_t\,\frac{\partial u_k}{\partial x_k}\right)\delta_{ij} \tag{5.9}$$

where

$$k = \frac{1}{2}\left(\overline{u'^2} + \overline{v'^2} + \overline{w'^2}\right) \tag{5.10}$$

which is the turbulent kinetic energy per unit mass. The turbulent viscosity, μ_t, is defined as the proportionality factor. The second term on the right hand ensures that normal stresses are modelled correctly. This approach differs from the RSM in that the turbulent viscosity is assumed to be isotropic, which is not strictly true. The assumption, however, holds for flows dominated by only one turbulent shear stress which covers many technical flows (ANSYS Fluent, 2011). Due to the relative simplicity of the approach the computational resources required is reduced in comparison to the RSM. The Boussinesq approach is used in the case of various turbulence models which include the Spalart-Allmaras, k-ε models and k-ω models.

Spalart-Allmaras

The Spalart-Allmaras model (Spalart and Allmaras, 1992) involves one additional transport equation for the turbulent kinematic viscosity, $\tilde{\nu}$. The (dynamic) turbulent viscosity is defined as

$$\mu_t = \rho\, \tilde{\nu}\, f_{v1} \tag{5.11}$$

where

$$f_{v1} = \frac{\chi^3}{\chi^3 + C_{v1}^3}, \tag{5.12}$$

and

$$\chi = \frac{\tilde{\nu}}{\nu} \tag{5.13}$$

The wall-damping function, f_{v1}, is a damping factor between zero and one. At high Reynolds numbers the function tends to unity and is equal to the kinematic turbulent viscosity. The viscosity affected region of the boundary layer must be solved, which requires a y^+-value of approximately one. Since the turbulence kinetic energy is not calculated the last term in Equation 5.9 is neglected. This model is developed for wall-bounded aerodynamic flows and gives good performance for boundary layers under adverse pressure gradients, which is important in predicting stalls. Due to the fact that the length scale is not calculated, but also not specifically calibrated for general internal flows, the model produces large errors in free shear flows and complex geometries (ANSYS Fluent, 2011; Versteeg and Malalasekera, 2007).

k-ε turbulence models

The two-equation k-ε turbulence models focus on the mechanisms which affect the turbulent kinetic energy. Many formulations of the k-ε turbulence model have been proposed, three of which will be discussed here. The variable ε represents the rate of dissipation of turbulent kinetic energy and is the destruction term in the kinetic energy equation. Important to note is that the dissipation of turbulence is a result of the work done by the smallest eddies against viscous stresses (Versteeg and Malalasekera, 2007). The turbulent kinetic energy equation is given in its exact form while the exact equation for the rate of viscous dissipation contains many unknown variables and physical reasoning is applied to define ε. In the derivation of the k-ε model the flow is assumed to be fully turbulent, which suggests that the molecular viscosity is negligible. The length scale ι and velocity scale ϑ for large-scale turbulence are, however, defined as

$$\vartheta = \sqrt{k} \tag{5.14}$$

$$\iota = \frac{k^{3/2}}{\varepsilon} \tag{5.15}$$

The definition of the length scale suggests that small, dissipating eddies are coupled to large-scale turbulence which in reality proves to be valid for higher Reynolds numbers. To compute the Reynolds stresses the Boussinesq approach is used and the turbulent viscosity is therefore defined as

$$\mu_t = C_\mu \, \rho \, \vartheta \iota = \rho \, C_\mu \frac{k^2}{\varepsilon} \tag{5.16}$$

The *standard k-ε model* proposed by Launder and Spalding (1974) makes use of the universal near-wall flow behaviour at high Reynolds numbers. The validity of this assumption based on turbulent kinetic energy analysis proves to hold for y^+ values between 30 and 500 and therefore the turbulent kinetic energy and rate of dissipation can be used to define a log-law function

$$u^+ = \frac{U}{u_\tau} = \frac{1}{\kappa} \ln(E \, y^+) \tag{5.17}$$

where

$$k = \frac{u_\tau^2}{\sqrt{C_\mu}} \tag{5.18}$$

and

$$\varepsilon = \frac{u_\tau^3}{\kappa y} \tag{5.19}$$

The Von Karman's constant κ = 0.41 and E = 9.8 are used for smooth walls. The variable y represents the normal distance from the wall. At low Reynolds numbers, however, the wall function is not valid and a damping factor similar to f_{v1} for Spalart-Allmaras can be applied. The dynamic viscosity can also be added to both equations to account for low Reynolds numbers. The rate of dissipation tends to become very large as the wall is approached and there is no good approximation found to date which accurately models the dissipation rate for a wide variety of flows (ANSYS Fluent, 2011; Versteeg and Malalasekera, 2007).

The standard two-equation k-ε model assumes that the Reynolds stress tensor, $-\rho\overline{u_j' u_i'}$, is proportional to the mean rate of deformation of a fluid element which is not valid in rapidly changing flows. Furthermore the assumption that all flow behaves in an isotropic manner does not hold true for situations in which adverse pressure gradients, recirculating or complex flows are found. Due to these limitations of the standard k-ε model, other formulations have been proposed.

The *two-layer k-ε model* is a less grid independent and stable low-Reynolds number k-ε model. *ANSYS Fluent* however incorporates the principles of this formulation in the *Enhanced Wall Treatment* model explained later. The prediction of the low Reynolds number near-wall region is improved by distinguishing between the fully turbulent region and the viscous sub-layer and placing the near-wall node in the viscous region. The two regions are identified by calculating $Re_y = y\sqrt{k}/\nu$. The fully turbulent region, $Re_y \geq 200$, is solved by the standard k-ε formulation. In the viscous region, $Re_y < 200$, only the k-equation is solved and the dissipation rate is determined by calculating the length scale by an algebraic equation (ANSYS Fluent, 2011; Versteeg and Malalasekera, 2007).

The *RNG k-ε model* is mathematically highly complex and therefore only the fundamental changes are mentioned, as given by ANSYS Fluent (2011). An additional term has been added to the ε-equation to improve performance for rapidly straining flows. An effective viscosity is also derived in the form of a differential formula which accounts for low-Reynolds effects. The prediction of swirl is improved by the RNG model. Consequently the RNG model out performs the standard k-ε model for the effects of rapid strain and streamline curvature effects. The RNG model, however, does not always outperform the standard k-ε model (Versteeg and Malalasekera, 2007).

The r*ealizable k-ε turbulence* model (Shih et al., 1995) is different from the standard k-ε model in two distinct ways: The turbulent viscosity is formulated differently and the equation for the dissipation rate has been derived in a more exact manner. The realizable model mathematically satisfies certain constraints on the Reynolds stresses by combining the Boussinesq relationship and the turbulent viscosity defined by Equation 5.16. The constant C_μ is now defined as a variable

$$C_\mu = \frac{1}{A_0 + A_s \frac{k\,U^*}{\varepsilon}}, \qquad A_0 \; and \; A_s \; given \; constants \tag{5.20}$$

where

$$U^* \equiv \sqrt{S_{ij}\,S_{ij} + \tilde{\Omega}_{ij}\,\tilde{\Omega}_{ij}} \tag{5.21}$$

$$\tilde{\Omega}_{ij} = \Omega_{ij} - 2\,\varepsilon_{ijk}\,\omega_k \tag{5.22}$$

$$\Omega_{ij} = \overline{\Omega_{ij}} - \varepsilon_{ijk}\,\omega_k \tag{5.23}$$

and S_{ij} is the mean strain and Ω_{ij} is the mean rate-of-rotation tensor in a moving reference frame with an angular velocity ω_k. These equations are deemed important due to the fact that the extra rotational term $-2\,\varepsilon_{ijk}\,\omega_k$ is not compatible with simulations using multiple reference frames and *ANSYS Fluent*, by default, removes this term from the realizable k-ε formulation. According to ANSYS Fluent (2011) the model is still relatively new but initial performance tests have shown the realizable model to provide the best performance for validation studies on complex and separated flows.

k-ω turbulence models

The turbulent viscosity in the k-ε models was defined as the product of the velocity scale and length scale given by Equations 5.16. For the *standard k-ω turbulence model* the dissipation rate ε is replaced by another variable, the turbulence frequency (specific dissipation rate) $\omega = k/\varepsilon$. This model is modified to incorporate low-Reynolds number flows and integration to the wall. Therefore the viscous sub-layer does not require wall damping functions as discussed in the case of Spalart-Allmaras. The sensitivity of simulations to the value of k and ω in the free stream flow region is, however, one of the downsides to this model and is not recommended in general flows (ANSYS Fluent, 2011).

The *k-ω SST turbulence model*, proposed by Menter (1993), combines the stable performance of the k-ε turbulence model in the free stream region with the k-ω model which is characterized by the simplistic yet accurate prediction of the near-wall region. These two models are added together by a blending function which activates the appropriate model in the separate regions. It also allows for smooth transition between the two models (ANSYS Fluent, 2011). Furthermore, performance in flows with adverse pressure gradients and wake regions are improved by limiting turbulent viscosity (Versteeg and Malalasekera, 2007). This model proves to be reliable and accurate for a wide variety of flows.

Emphasis is usually placed on the importance of the correct y^+-value for the wall cell although it is more important to place enough cells in the boundary layer. For turbulence models such as the k-ω SST and the Spalart-Allmaras model,which solve the boundary layer, *ANSYS Fluent* recommends y^+-values of approximately one with at least ten cells located inside the boundary layer. If wall-functions are used the near-wall y^+ value should not be much less than 30. The sensitivity of a solution to the above mentioned parameters presents a challenge when creating a computational mesh. For this reason *ANSYS Fluent* has developed an *Enhanced Wall Treatment* function.

The use of the Enhanced Wall Treatment for k-ε turbulence models results in a y^+ insensitive simulation which combines the two-layer approach with enhanced wall functions as referred to by ANSYS Fluent (2011). For the purposes of modelling the Reynolds stresses the two-layer model for the turbulent viscosity is blended with the turbulent viscosity in the high Reynolds region by

$$\mu_{t,enh} = \lambda_\varepsilon\, \mu_t + (1 - \lambda_\varepsilon)\, \mu_{t,2layer} \tag{5.24}$$

where the turbulent viscosity in the viscosity-affected region is defined as

$$\mu_{t,2layer} = \rho\, C_\mu\, \iota_\mu\, k \tag{5.25}$$

and the length scale is calculated from the algebraic relation

$$\iota_\mu = y\, C_l\left(1 - e^{-Re_y/A_\mu}\right) \tag{5.26}$$

The blending function $\lambda_\varepsilon = \lambda_\varepsilon(Re_y)$ tends to unity as the fully turbulent region is approached with $\lambda_\varepsilon(Re_{y=0}) = 0$. The constant C_l is calculated by the formulation $C_l = \kappa C_\mu{}^{-3/4}$ and the constant A specifies the width of the blending function. The dissipation rate, ε, in the viscous region is calculated by

$$\varepsilon = \frac{k^{3/2}}{\iota_\varepsilon} \tag{5.27}$$

where the length scale ι_ε is calculated in a similar way to ι_μ. The dissipation rate for the fully turbulent region is obtained from solving the transport equation. Furthermore a single wall function which is extended to include both the linear and logarithmic law-of-the-wall is included. This formulation correctly predicts the behaviour for large and low y^+ values. Velocity behaviour in the buffer region ($3 < y^+ < 10$) is also well represented. The Enhanced Wall Treatment function is recommended by *ANSYS Fluent* for all two-equation wall function turbulence models.

5.1.2 Rotational modelling

To simulate rotating machinery various rotational modelling approaches as mentioned in Chapter 2 are available. Steady state modelling approaches include the mixing plane and MRF approach. The sliding mesh formulation is applied to transient simulations. Only steady state simulations were carried out for this thesis. The summary of the literature review given in Chapter 2 stated that most steady state simulations used the MRF approach and therefore this approach was used for all simulations.

Both the mixing plane and MRF approaches divide the computational domain into different rotational parts referred to as cell zones. These zones are separated (connected) by interface boundaries. The mixing plane and MRF approach differ in the way the flow is treated at these interface boundaries. In the case of the MRF approach a local reference frame transformation is implemented which enables the calculation of fluxes at both sides of the interface. For the mixing plane approach the flow data is circumferentially averaged at the interface boundaries by either a mass-averaged or area-averaged formulation. Mixing the flow at the interface boundaries removes all unsteadiness and circumferential variation (ANSYS Fluent, 2011).

ANSYS Fluent solves the rotating zones using a set of moving reference frame equations. It also allows the user to specify whether the velocity is solved in a relative or absolute frame of reference. The relative velocity formulation calculates velocities relative to its subdomain's motion. This implies that the governing equations are formulated relative to the motion of the subdomain. The governing equations for the absolute velocity formulation are very similar although the velocity and velocity gradient quantities are stored in an absolute frame of reference. Note that the velocity and velocity gradient vector quantities are the only variables which change with a change in reference frame. All scalar quantities such as static pressure and density are simply passed from one zone to the other. *ANSYS Fluent* recommends the absolute velocity formulation for cases in which most of the computational domain is specified as stationary.

Using different software packages to model the inlet and outlet domains resulted in non-conformal mesh interfaces. *ANSYS Fluent* deals with non-conformal meshes by creating new faces on the interface from the two zones.

To illustrate this procedure consider the two cell zones in Figure 5.1. New faces represented by a-d, d-b, b-e and e-c are produced from the intersection between the two interface zones. To calculate the information passed on from cell zone 1 two new faces are defined replacing the face DE. Information from both cells I and III are therefore used due to the newly defined faces d-b and b-e. Partially overlapping meshes (e.g. face a-d) is treated as specified by the user in *ANSYS Fluent*. These faces can be treated as walls, boundaries with periodic repeats (usually valid for sliding meshes and turbomachinery applications) and non-conformal periodic boundaries.

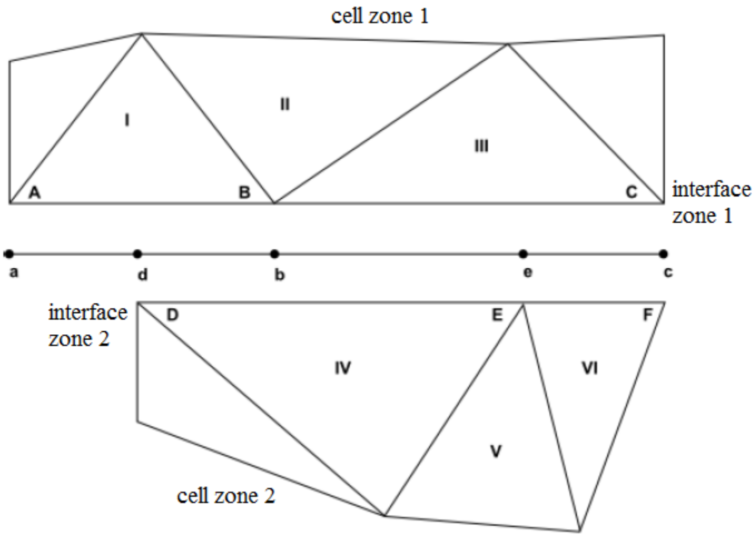

Figure 5.1 - Non-conformal mesh handling (ANSYS Fluent, 2011)

5.2 Modelling

Figure 5.2 illustrates the fundamental processes that are involved in simulating an axial fan as applied to this thesis. For the purposes of this discussion these processes will be divided into three main sections namely: computational domain, meshing and solving.

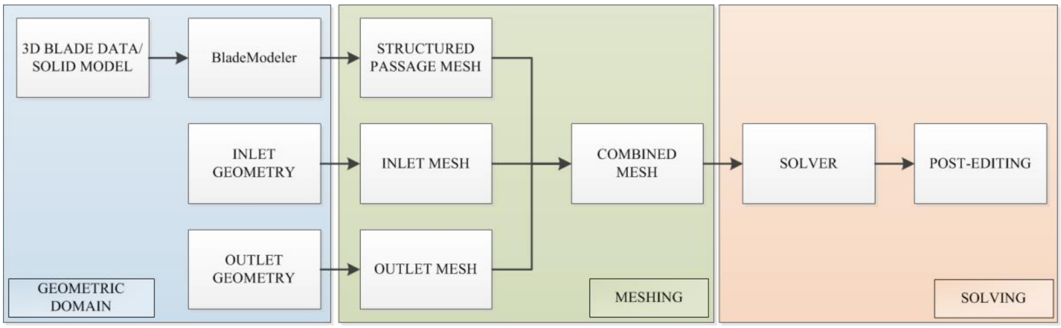

Figure 5.2 - Fundamental processes involved with simulating an axial fan

Geometric domain

The geometric domain was divided into an inlet, passage (which includes the blade geometry) and an outlet. The physical geometry and dimensions for each of the three domain parts directly influence the mesh that is generated. The fan solid model that was created as explained in Chapter 3 is imported into ANSYS *BladeModeler* (which is activated inside ANSYS *DesignModeler*) and forms part of the blade passage geometry.

Meshing

The meshing software uses the generated geometry to create a mesh according to user specifications. Each mesh was created independently of the other. Once the three meshes were created, they were combined (not merged) to form a single mesh which represented the full computational domain. It was possible to create a limited size mesh in *ANSYS TurboGrid* with a conformal inlet and outlet.

Solving

Boundary conditions and solver settings (discretization methods, turbulence model etc.) were applied to the computational mesh domain inside ANSYS *Fluent*. A case file consisting of the computational mesh and its accompanied settings were initialized and solved for a specified number of iterations. Post-processing followed after the convergence of a simulation.

Figure 5.3 is a detailed flowchart of the numerical simulation process from start to finish. The purpose of the flow chart is to provide a foundation from where further and future numerical work on axial fans can be built upon. It also indicates various decision paths that could have been taken to solve a case. Other important points to note are:

- All solid CAD fan models were imported into *ANSYS DesignModeler* and *ANSYS BladeModeler* was used to generate the blade profile file required in *ANSYS TurboGrid*.

- *ANSYS TurboGrid* only generates structured grids for turbomachinery applications.
- The larger inlet and outlet domains were created in *ANSYS DesignModeler* and the meshes generated in *ANSYS Meshing.*
- *ANSYS Fluent* was used for solving all simulations, although *ANSYS CFX* was also available.

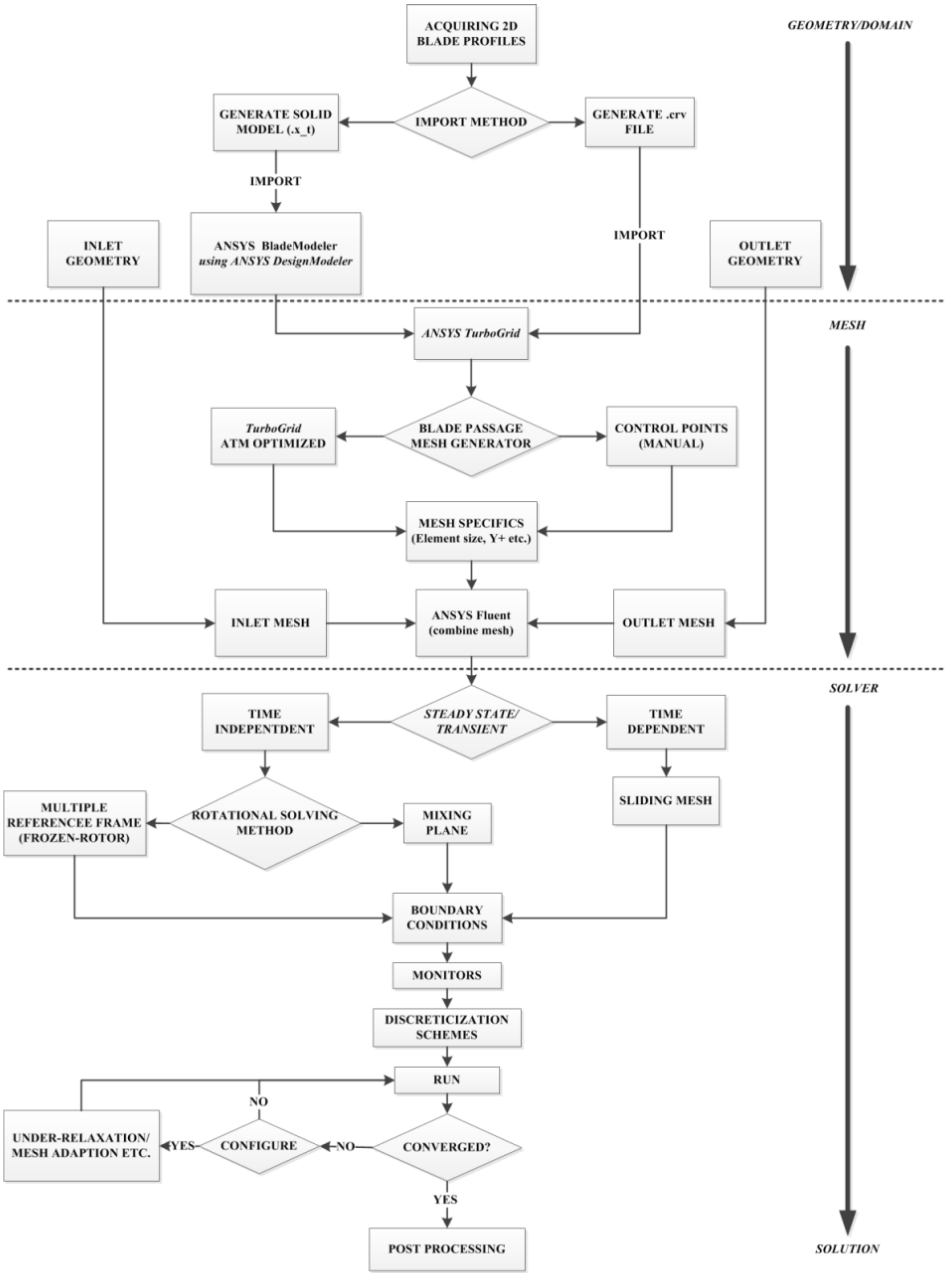

Figure 5.3 - Detailed flow chart of the process in Figure 5.2

To examine the effect that the domain has on a simulation various alterations had to be considered. There were two main concepts from which all of the computational domains were derived. Both these concepts are shown in Figure 5.4. Concept A's domain consist of a ducted inlet and ducted outlet. Both the inlet and outlet (or either) can be an annulus section as variant. Concept B is a simplified representation of the BS 848 (Type A) facility where the experimental tests were carried out. The inlet of Concept B can be seen as a plane, downstream of the screen meshes in Figure 4.4. The outlet represents atmospheric conditions.

A.) Ducted inlet & outlet

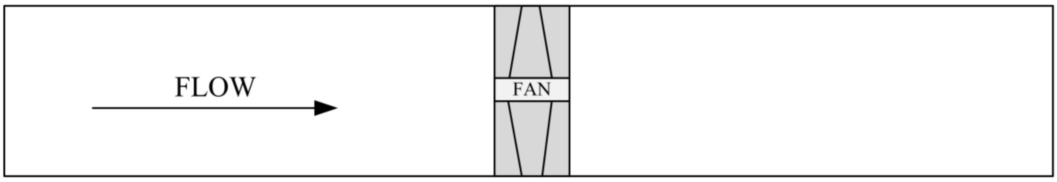

B.) BS 848 Facility

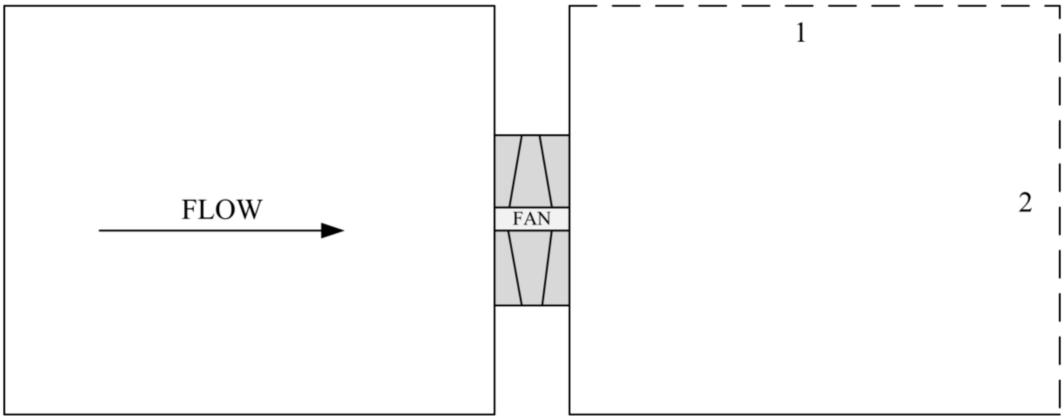

Figure 5.4 - Two main computational domain concepts

Axial fans can be regarded as periodic machines which made it possible to reduce the computational domain to only an 8th (B-fan and L2-fans) or 9th (N-fan) of the size. This resulted in much less computational demanding simulations and also made local refinement of the mesh grid possible. The B-fan will be discussed separately from the L2- and N-fan with regards to geometry, meshing and boundary conditions.

5.2.1 Mesh

All computational meshes were generated using either *ANSYS TurboGrid* or *ANSYS Meshing*. The blade passage meshes for the different fans were all created using *ANSYS TurboGrid*'s structured grid functionality.

The blade geometry in *ANSYS TurboGrid* was defined based on the data of the .crv-file exported from *ANSYS BladeModeler*. Blade profile (layer) curves, consisting of numerous coordinates connected by lines, were created by using a B-spline or linear piece-wise approach. Likewise spanwise lofting could either be done by using B-splines or linear lines ("ruled"). These settings have a significant effect on the surface finish of the blade geometry and overall mesh quality at the near-blade (wall) region.

The "ATM optimized" mesh topology option was used in all cases. Instead of creating a mesh using the O, H or C topologies, the "ATM optimized" option creates topology layers based on the geometry of the turbomachinery domain. The positioning of the layers is user specified across the span of the blade and the final mesh volume is built upon these layers. Figure 5.5 shows a layer of the leading edge region of the L2-fan.

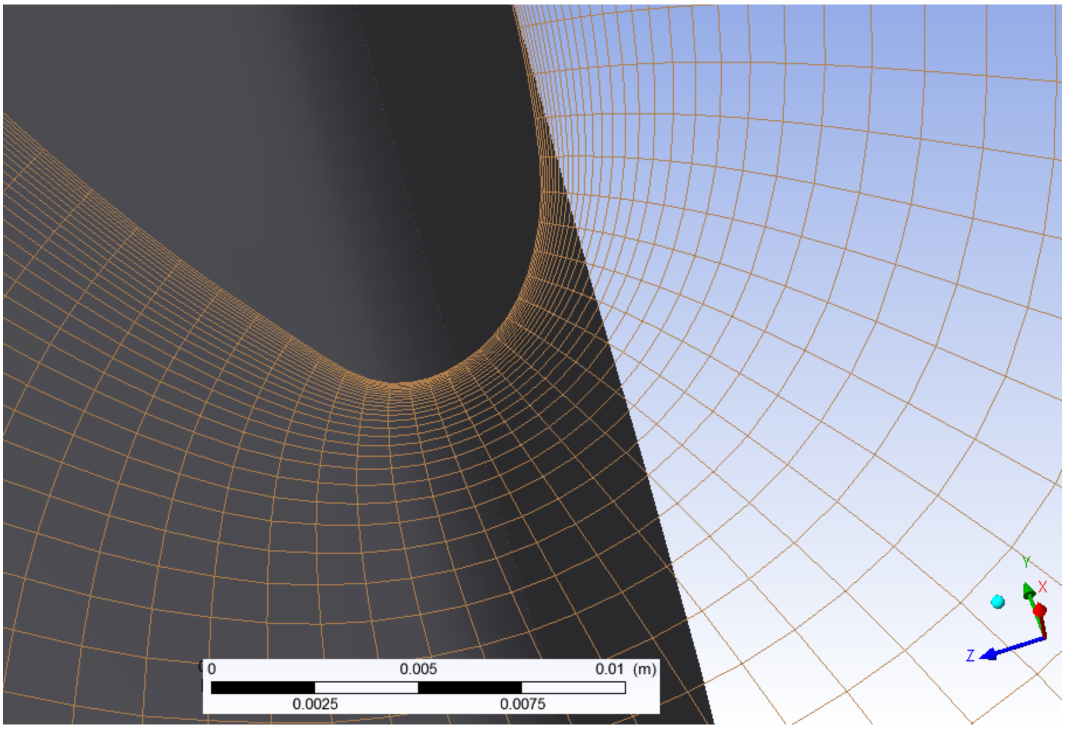

Figure 5.5 – Leading edge of L2-fan mesh layer

ANSYS TurboGrid allows the user to specify a target number of cells and the near-wall spacing Δy in accordance with the required y^+-value at the blade wall. Δy is calculated by

$$\Delta y = L\, y^+ \sqrt{80}\, \mathrm{Re}_x^{1/14} \frac{1}{Re_L} \tag{5.28}$$

where L is the average blade chord length and Re_x is approximated to be the same as the specified Re_L-value based on the chord length. This method enables the user to change the target cell number but still maintain the correct near wall spacing Δy. Local refinement of the mesh was done by configuring the multiple layers. Important to note is that local refinement on a specific layer is carried through the mesh volume due to its structured nature. The number of cells in the spanwise direction was determined by a proportional factor based on the combined limits of the wall spacing and target cells. In some cases the proportional factor had to be decreased in order for the wall spacing and target cell limits to be satisfied.

The above described method allowed quick and easy mesh generation, but the quality of the mesh was indicated by mesh statistic parameters. Three specific mesh statistics parameters were considered important, as suggested by *ANSYS TurboGrid*:

- Minimum volume: If the mesh contains any negative volume cells *ANSYS TurboGrid* does not permit the export of the mesh. This is usually an indication of faulty defined cells.
- Maximum/Minimum face angle: This parameter is an indication of the skewness of a cell. Values between 15° and 165° were considered acceptable.
- Edge length ratio (Aspect ratio): It is a ratio of the longest edge of the face divided by the shortest edge of the face. Theoretically this parameter should be as close to 1 as possible. The percentage of cells over this limit was also considered to be important.

Due to *ANSYS TurboGrid* placing a limit on the number of inlet and outlet cells in the flow direction (z-direction) the larger inlet and outlet meshes were created in *ANSYS Meshing*. The details of these larger meshes are controlled by specifying a number of elements to various edges. There were no significant near-wall regions except for the inlet bellmouth wall. Generating the larger inlet and outlet meshes in different software than the passage resulted in non-conformal meshes at the interfaces.

5.2.2 Boundary conditions

Boundary conditions fulfil an important role in all simulations because it governs the computational stability and numerical convergence thereof (Tu et al., 2008). The initial conditions of a simulation are also specified at these boundaries. Two types of boundary conditions can be specified: the Dirichlet and Neumann boundary conditions. The Dirichlet boundary condition involves specifying a physical quantity, defined as

$$\phi = f(analytic) \tag{5.29}$$

where ϕ is a transport property. For the Neumann boundary condition a derivative of the transport property is specified, such as

$$\frac{\partial \phi}{\partial n} = 0 \tag{5.30}$$

It is generally good practise to specify a Dirichelt boundary condition at the inlet and Neumann boundary condition at the outlet. This, however, is not an absolute necessity as it is not always possible (Tu et al., 2008). Another important factor to consider is the specification of the entering turbulent flow. The important boundary conditions used for all simulations in this thesis will be discussed briefly.

Mass flow inlet

This boundary condition provides a specified mass flow rate (or mass flux) at the inlet. The mass flow inlet allows the total pressure to vary across the boundary as the solution permits. Unlike the velocity inlet, a mass flow inlet can be used for compressible and incompressible flow. ANSYS Fluent (2011) however, recommends a total pressure inlet boundary condition if the pressure at the inlet is known. The continual adjustment of the total pressure when using a mass flow rate boundary condition can cause slow convergence.

Pressure outlet

The specification of the static pressure is required for a pressure outlet boundary condition which allows the mass flow/velocity to vary. The option of specifying radial equilibrium as explained and used by Le Roux (2010) can also be applied. ANSYS Fluent (2011) also allows the user to specify the “backflow” conditions which can reduce instability and minimize convergence difficulties.

Outflow

The outflow boundary condition is used to model exits where the details of neither the mass flow nor pressure are known. A zero diffusion flux for all flow variables is specified at the boundary and therefore no specific value is required at the boundary. This condition is approached physically in fully-developed flow. The outflow boundary condition used in ANSYS *Fluent* cannot be specified for:

- Flows where an inlet pressure boundary exists.
- Compressible and unsteady flows.

ANSYS Fluent (2011), however, states that the outflow boundary condition can be placed in the developed flow region if the axial flow gradients are expected to have a small impact on the flow. It also mentions that recirculation at the outflow boundary can affect convergence even if the final solution is expected to have no backflow (particularly in turbulent flow simulations).

Turbulent inlet flow parameters

The mass flow inlet boundary condition requires the specification of the turbulent inlet flow conditions. The turbulent intensity I and hydraulic diameter D_H were specified in all cases. According to ANSYS Fluent (2011) the turbulent intensity can be approximated by

$$I = \frac{u'}{u_{avg}} = 0.16\left(Re_{D_H}\right)^{-1/8} \tag{5.31}$$

where Re_{D_H} is the Reynolds number based on the hydraulic diameter which is, for an annular duct, defined as

$$D_H = D_o - D_i \tag{5.32}$$

For the larger square inlet, based on the BS 848 test facility, the hydraulic diameter was calculated by

$$D_H = \sqrt{\frac{4bh}{\pi}} \tag{5.33}$$

5.2.3 Solving methods and Discretization

ANSYS *Fluent* allows the user to choose between two numerical solving methods: pressure-based and density-based. The pressure-based method was developed for low-speed incompressible flows whereas the density based method is generally used in compressible flows. In both cases a control-volume-based technique is used. All simulations carried out in this study used the pressure-based approach due to axial fans operating in the incompressible flow regime (ANSYS Fluent, 2011). The choice of the pressure–velocity coupling method was based upon the use of the SIMPLE algorithm in fan research by authors such as Thiart and Von Backström (1993); Bredell et al. (2006); Fernandez Oro et al. (2011); Lin and Tsai (2011); Louw (2011); Masi and Lazzaretto (2012) and Zhao et al. (2012).

There are various options available for handling spatial discretization in ANSYS *Fluent*. The QUICK scheme is specifically useful for swirling and rotating flows. It is regarded as a higher-order discretization scheme which is typically more accurate than a second-order upwind scheme for structured meshes with cell faces aligned with the flow. The QUICK scheme can also minimize diffusion errors although this scheme is usually less computationally stable compared to a second-order upwind scheme (ANSYS Fluent, 2011; Versteeg and Malalasekera, 2007). In a study by Van der Spuy et al. (2010) evaluating various models for the performance of axial fans the QUICK scheme was used. Other studies using the QUICK scheme to simulate axial fans included Meyer and Kröger (2001), Vad et al. (2007) and Jian-Hui and Chun-Xin (2008). Considering all the above mentioned, the QUICK scheme was used for all simulations carried out in this study.

5.3 B-fan

The purpose of simulating the B-fan was to establish a methodology that could also be used to simulate the L2- and N-fan. Le Roux (2010) initially simulated the B-fan with a large axis-symmetric inlet and outlet resembling the BS 848 test facility as shown by Concept B in Figure 5.4(b). The outlet boundary conditions of the two approaches of Le Roux (2010) used a slip wall at the upper outlet boundary (Figure 5.4(b-1)) and a zero static pressure at the downstream outlet (Figure 5.4(b-2)). The use of multiple rotating reference frames such as the mixing plane and MRF approach resulted in large errors. Good performance for higher flow rates was found when the entire domain was solved in a single rotating frame. Taking into consideration the final remarks of Le Roux (2010) and the findings of Meyer and Kröger (2001) a different approach was taken for the simulation of the B-fan. A systematic approach starting with the most elementary concept was followed. Instead of simulating the entire BS 848 test facility, a simplified geometry consisting of an annular duct inlet and outlet would be simulated without tip clearance. Once these simulations produced satisfactory results more detail was added to the geometry with the purpose of applying it to the L2- and N-fan.

All B-fan simulations were carried out with an annular duct inlet and annular duct outlet. The entire mesh was generated in *ANSYS TurboGrid* which was advantageous because of *ANSYS TurboGrid's* ability to generate conformal mesh interfaces between the various cell zones.

Initial modelling of the B-fan, using the Spalart-Allmaras turbulence model, required a large number of cells in the blade passage region. This could be attributed to a recommended y^+-value of 1. Although it was possible to achieve the required y^+-value, the aspect ratio in the near-wall region exceeded an acceptable limit (~500). Based on the theory discussed in section 5.1.1 and the literature review in Chapter 2 the k-ε turbulence model was selected as the best alternative choice for further simulations. To examine the difference between various k-ε turbulence models a comparative study between the standard, RNG and realizable k-ε models were carried out. The results of these simulations would be used to direct the approach taken for the L2- and N-fan simulations.

5.3.1 Computational domain

Figure 5.6 is a meridional plane view of the computational domain used for all simulations of the B-fan. The length of the inlet is one fan diameter (D = 1.542 m) and the length of the outlet is one and a half fan diameters. Initial simulations were also carried out with a two diameter outlet length but no significant difference in the measured parameters was found. Poor quality cells were, however, present near the outlet of the two diameter domain and therefore the outlet was shortened to one and half diameters. Note that the width of the hub is extended from 0.15 m to 0.2 m. This was due to the leading and trailing edges (of the actual blade) being very close to the edge of the hub and *ANSYS TurboGrid* being unable to generate a satisfactory mesh in those regions. A change in the hub length only affected the size of the relative reference frames in which the flow is solved if one considers that the inlet and outlet were annular ducts.

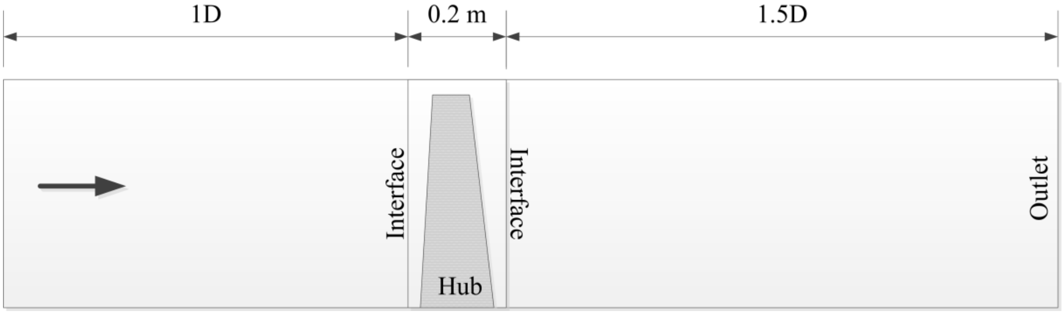

Figure 5.6 - Meriodinal plane of the computational domain of the B-fan

5.3.2 Mesh specifications

Three B-fan meshes of increasing size were simulated to demonstrate mesh independence. Table 5.1 gives the specifications for each of the three meshes. Mesh 1 had a y^+-value of 60 although the target number of cells was the same as Mesh 2. Note that the target cell size is only applicable to the blade passage. The inlet and outlet mesh sizes were largely based on the 100 cell limit in the flow direction. The number of target cells was doubled for Mesh 3, although the y^+-value was still set at 30. The initial high target cell number was due to the requirement of the mesh statistics parameters. Large aspect ratios were found in the trailing edge region which is due to the large blade span (~ 463 mm) and near-wall spacing requirements. By increasing the specified y^+-value for the first near-wall node the total number of cells were slightly reduced. The number of cells in the spanwise direction was specified by the proportional factor. Increasing the proportional factor increased the number of cells in the spanwise direction.

Table 5.1 - Specifications for the three different size meshes of the B-fan

B-fan	**Mesh 1**	**Mesh 2**	**Mesh 3**
Target number of cells	1 000 000	1 000 000	2 000 000
y^+	60	30	30
Re_L	630 000	630 000	630 000
Proportional factor	1.5	1.5	2
Total number of cells	2 354 828	3 114 586	5 478 878

The B-fan blade was designed with a cut-off trailing edge and therefore linear piece wise curves were lofted in the spanwise direction using B-splines. Furthermore, generating a well-defined mesh in this region was problematic.

Although *ANSYS TurboGrid* has a function for cut-off trailing edges, applying the option did not result in a satisfying mesh. Good definition at the trailing edge was found when localised edge refinement was increased in this region.

The validity of simulating the tip clearance region using wall functions was uncertain and therefore initial simulations were carried out without the modelling of a tip clearance. However, a mesh with tip clearance of 3 mm was simulated using the realizable k-ε turbulence model for comparative study. The mesh resembled the fine mesh used in the no-tip clearance case. The cell distribution in the 3 mm tip clearance region is shown in Figure 5.7. The near-wall spacing at the shroud and blade tip adheres to the y^+-value specified.

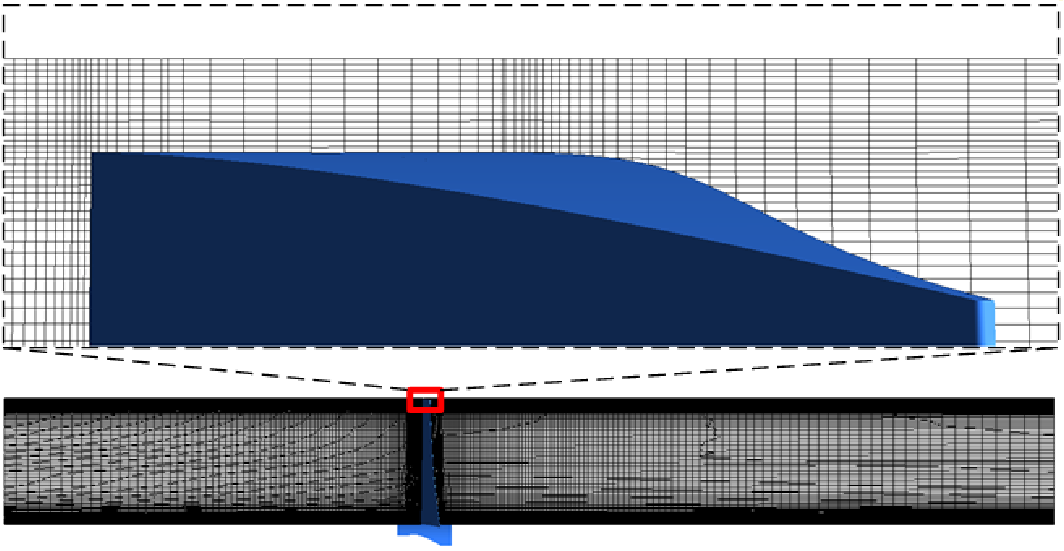

Figure 5.7 - B-fan computational mesh

5.3.3 Boundary conditions

Due to the fact that the entire mesh was generated in *ANSYS TurboGrid* the interfaces of the three cell zones were conformal. The blade passage cell zone, pressure- and suction blade surfaces and hub wall was specified to rotate at the design speed of 750 rpm relative to the absolute reference frame. All other cell zones and walls were stationary, relative to the absolute reference frame.

An inlet mass flow boundary condition was specified and an outflow condition at the outlet of the relative duct. All walls were specified as smooth no-slip walls and periodic boundary conditions were applied. All turbulence models were specified to use *ANSYS Fluent*'s Enhanced Wall Treatment function. This is partially due to the fact that the near-wall mesh recommendation of the k-ε turbulence models ($y^+ > 30$) could not be met for the entire blade surface. Each mesh size was simulated using each of the three k-ε turbulence models (standard, RNG and realizable) for three flow rates (12, 16 and 20 m^3/s). This equates to 27 simulations. A further three simulations were carried out with a tip clearance of 3 mm. Figure 5.7 shows the entire computational mesh.

5.4 N- and L2-fan

The L2- and N-fan were modelled similarly and will therefore be discussed together. Due to the fact that experiments were carried out for these fans and the B-fan simulations were only performed to develop a method of approach, greater focus was placed on the simulation of these fans. It is important to note that the fan geometries used in these simulations originated from the scanned data discussed in Chapter 3.

With the knowledge gained from the B-fan simulations, simulating a test facility with the actual fan used in the experiments seemed possible. However, a systematic approach was again followed to eliminate obvious mistakes. Both fans were therefore simulated in two distinctly different computational domains: a simplified inlet and outlet duct (resembling the computational mesh of the B-fan) and a closely representative model of the test facility.

5.4.1 Computational domain

The two computational domains were based on the concepts shown in Figure 5.4. The first domain is similar to the B-fan's domain having an annular inlet and outlet duct which will be referred to as Approach 1. The second domain, referred to as Approach 2, is based on the BS 848 facility shown in Figure 5.4(b).

Approach 1

The dimensions for this particular computational domain are shown in Figure 5.8. The inlet, similar to the B-fan's domain, was one diameter in length and the outlet one and half diameters long. Due to the small diameter of the hub and a very narrow hub casing the interfaces had to be specifically configured to ensure a good quality mesh in this region. This resulted in curved interfaces at the inlet and outlet as shown in Figure 5.8.

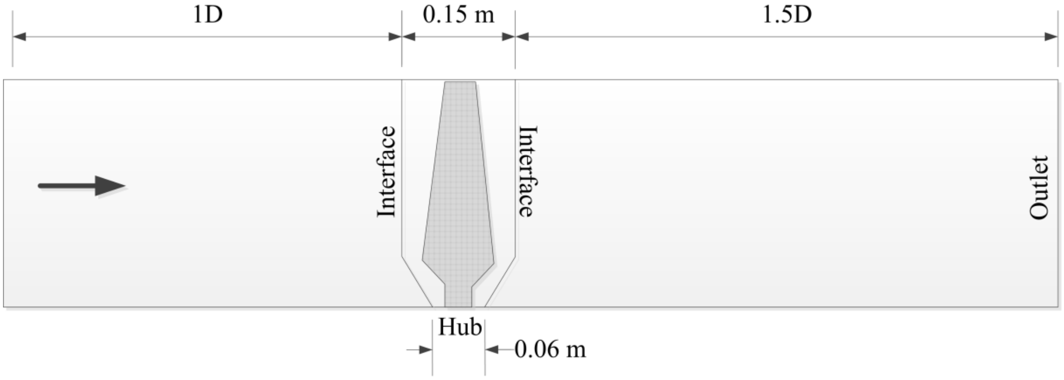

Figure 5.8 - Computational domain for Approach 1 of the L2- and N-fan

Approach 2

The second approach resembles the BS 848 test facility where the L2- and N-fan were tested. The computational domain shown in Figure 5.9 is divided into five distinct zones. Each zone has different mesh characteristics. Due to the curved interfaces of the rotor passage (zone 5) a short inlet and outlet domain is required to provide suitable interfaces to connect with other zones. These faces form part of the interfaces between zone 4 and 5 and zone 1 and 5. Using various zones allows for local refinement of the structured mesh.

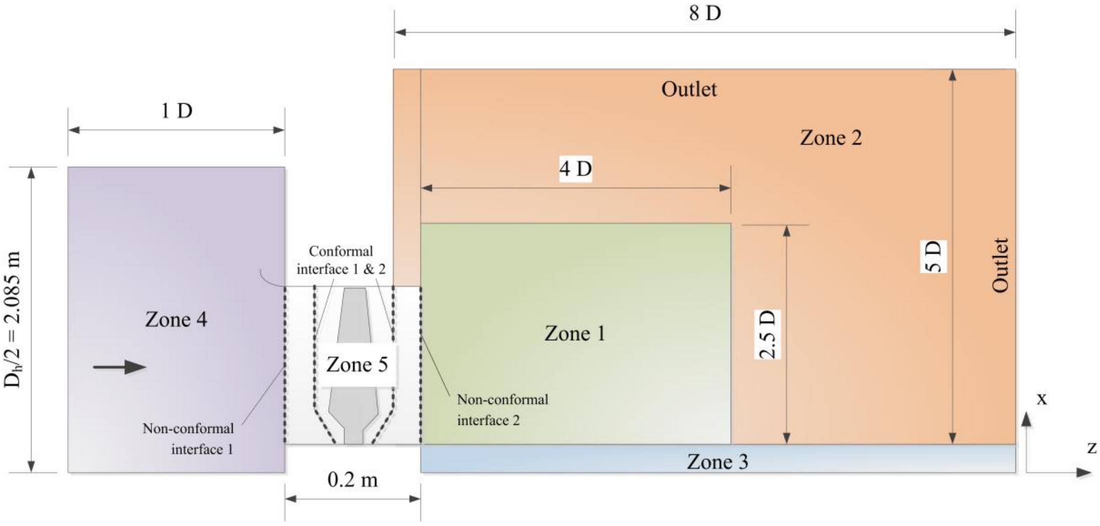

Figure 5.9 - Computational domain for Approach 2 of the L2-fan and N-fan

5.4.2 Mesh specifications

Approach 1

The procedure used for creating a mesh for Approach 1 was similar to the procedure used to create the B-fan's mesh. As mentioned earlier the initial target number of cells was dependent on the geometry of the fan and the required mesh statistic parameters. Due to the geometry of both fans in the hub region and an uneven lofted surface, a fine mesh was required to ensure accurate modelling. Furthermore, in order to satisfy the required mesh statistic parameters, large initial target cell numbers were used. Therefore only a single mesh size was simulated. The specifications for the L2- and N-fan are given in Table 5.2.

Table 5.2 - Mesh Specifications for Approach 1 of the L2- and N-fan

Approach 1	**L2-fan**	**N-fan**
Target number of cells	2 000 000	2 000 000
y^+	30	60
Re_L	600 000	600 000
Proportional factor	2	2
Total number of cells	**5 163 087**	**5 080 650**

Having found that the results of the B-fan's simulations indicated accurate modelling of the tip clearance a 5 mm tip clearance was included into the model. Figure 5.10 shows the region between the tip and the shroud. The y^+-value specified at both walls (shroud and blade tip) were between 30 and 60 with 30 elements placed in the space between the tip and shroud.

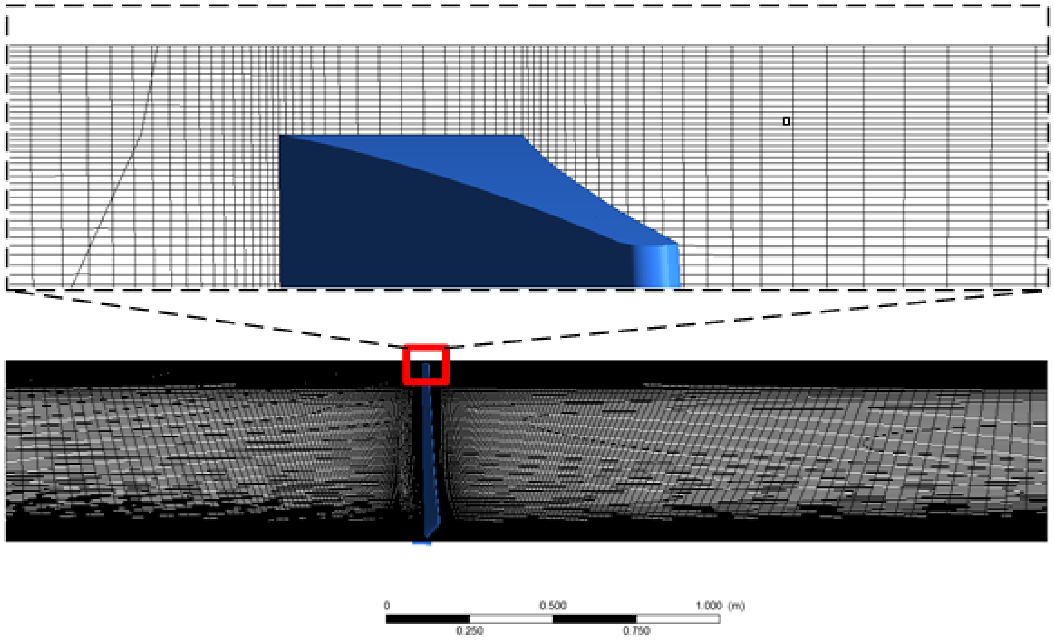

Figure 5.10 - Mesh in tip clearance region of Approach 1 for L2-fan

Approach 2

The details of Approach 2's mesh (see Figure 5.11) will be discussed referring to the zones shown in Figure 5.9. The mesh of both fans of Approach 1 was used in the larger mesh of Approach 2. The conformal inlet and outlet zones were, however, shortened as explained earlier which reduced the total number of cells of the original mesh dramatically. Due to the added large inlet and outlet, multiple interfaces were required, most being non-conformal. Initial attempts were made to use tetrahedral grids for the large outlet (for local refinement purposes), but no significant decrease in cell numbers was found. Therefore all zones consisted of structured grids.

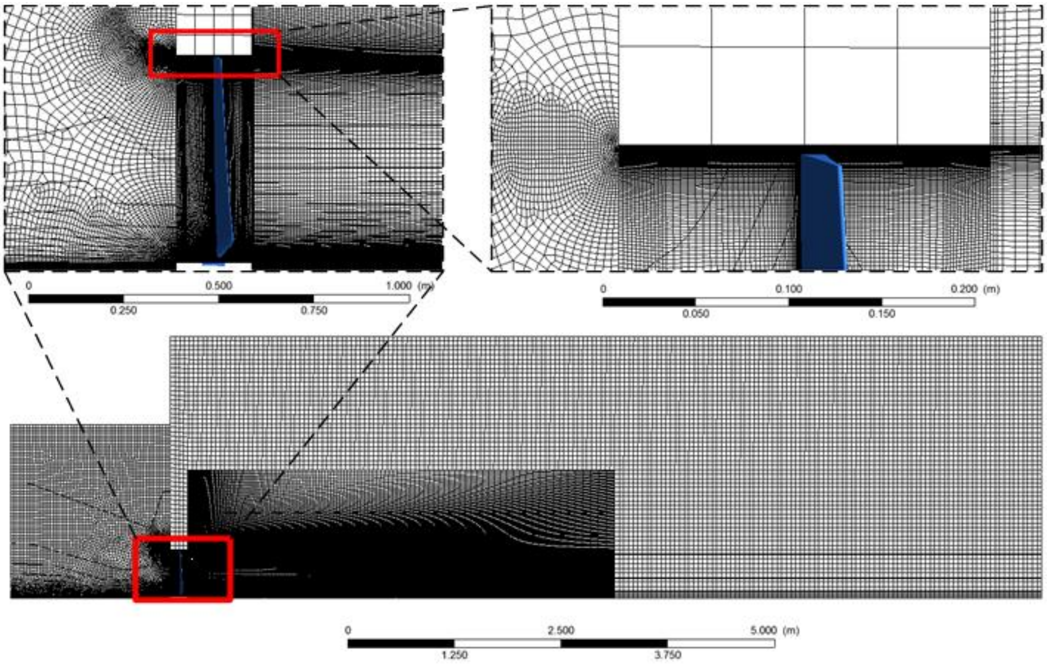

Figure 5.11 - Mesh of Approach 2

The large, but shortened, inlet (zone 4) of the domain housed the inlet bellmouth. The cells in the bellmouth region were locally refined to ensure appropriate near-wall spacing. The outlet consisted of zone 1, 2 and 3. The purpose of the division of the zones was to apply localized refinement to the necessary regions. zone 1, which encompasses the sensitive flow region at the exit, is a very fine mesh. This ensures that the larger velocity gradients and swirl which is present in the region behind the fan is captured. zone 2 is a coarser mesh which reduces the cell number in the regions where there is less flow activity. Due to practical reasons zone 3 was modelled separately from zone 2 although the two zones were conformal at their interface. The details of the various zones are given in Table 5.3.

Table 5.3 - Mesh Specifications for Approach 2 of the L2- and N-fan

Approach 2	**L2-fan**	**N-fan**
Zone 1	3 746 040	6 446 628
Zone 2+3	149 020	132 820
Zone 4	497 372	454 678
Zone 5	2 850 738	2 187 150
Total number of cells	**7 243 170**	**9 221 276**

5.4.3 Boundary conditions

The boundary conditions of Approach 1 were similar to the boundary conditions of the B-fan. Therefore, a mass flow inlet and outflow boundary condition at the outlet was specified. The rotational speed of the blade passage cell zone was specified to rotate at 900 rpm. The fan shroud velocity was specified as stationary for all fans in both approaches.

The boundary conditions of Approach 2 were different from Approach 1, specifically in the case of the outlet which used a pressure outlet instead of an outflow boundary condition. The cell zones of zone 5 (passage inlet, blade passage and passage outlet) and the blade pressure-, suction- and tip surfaces were specified to rotate at 900 rpm relative to the stationary reference frame. All other walls and cell zones were stationary. The outlet of Approach 2 resembled an open atmosphere which required flow to enter (backflow) and exit the outlet boundaries. Large amounts of backflow were expected to cross the outer outlet boundary which would result in slower convergence. The turbulent intensity for the backflow was specified to be 1%, the hydraulic diameter remaining the same. All walls had a no-slip condition.

The results of the B-fan's simulations indicated that the realizable k-ε turbulence model performed the best of the three k-ε models. The performance was based on accuracy across the flow rate range, the rate of convergence and stability during simulations. Therefore all simulations for the L2- and N-fan were carried out using the realizable k-ε turbulence model. The Enhanced Wall Treatment function was again used for the same reasons given for the B-fan simulations.

5.5 Solution control and monitors

Certain measures are used to indicate and ensure reliable validation between experimental and numerical results. These measures include monitoring parameters which influence the solution and the convergence of the simulation. A numerical procedure has converged if the properties of a solution are characterized by consistency and stability (Tu et al., 2008). A more mathematical approach to the above statement is found by monitoring the residuals. Residuals represent the imbalance found at a nodal point for a cell volume. The sum of all local grid point residuals is defined as the global residual. According to Tu et al. (2008) a numerical procedure is regarded to be converged if the global residual has reached a tolerance level of 10^{-5}.

Although residuals are a good indication of the level of convergence it proved to be an inconclusive measure of convergence for the simulations of the B-, L2- and N-fan. Monitors were used to track the change of pressure, torque and mass flow values at specified locations for increasing iterations. The literature review in Chapter 2 indicated acceptable residual levels to be between 10^{-4} and 10^{-6}. Solutions were therefore considered to be converged if all residuals reached a tolerance value of the order 10^{-5} and the monitored parameters remained constant for increasing iterations. Figure 5.12 indicates the converged nature of the pressure difference across the inlet and the outlet boundaries for Approach 2 of the L2- and N-fan.

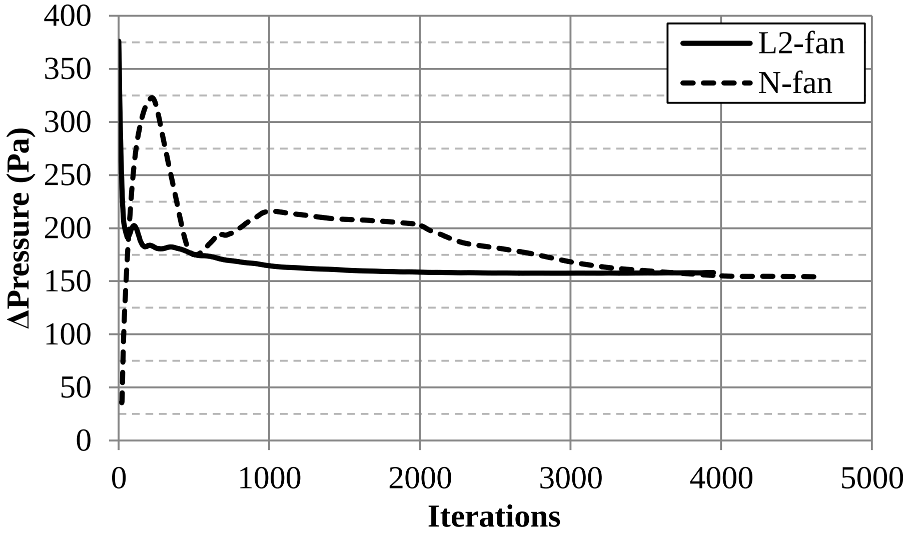

Figure 5.12 - Convergence of pressure for the L2-fan and N-fan.

Similarly Figure 5.13 shows the convergence of the pressure difference between the inlet and outlet boundaries of the different turbulence models for the ducted domain of the B-fan. It was found that the torque and mass flow monitors had a tendency to converge more quickly than the pressure, which is to be expected.

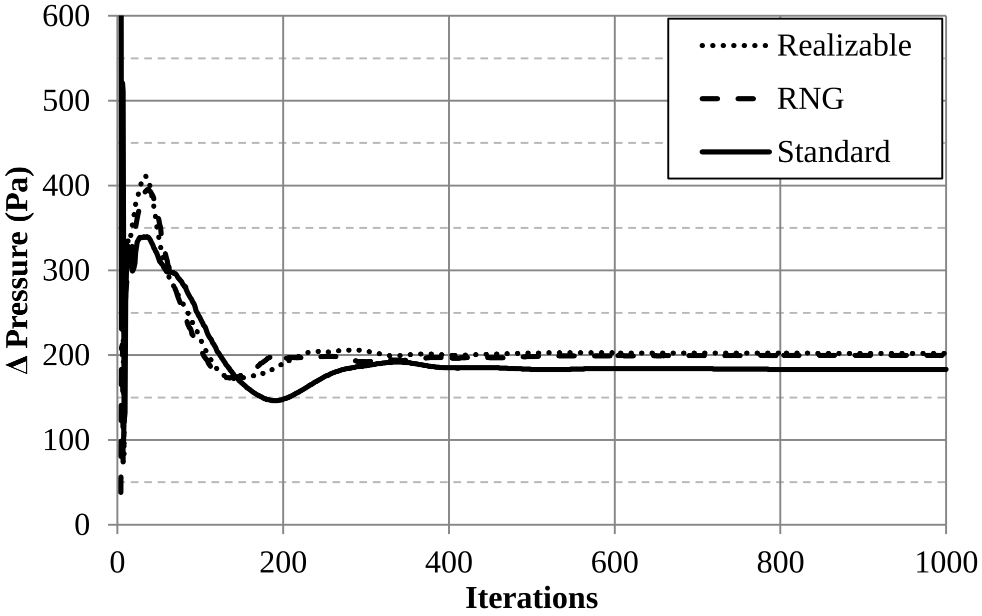

Figure 5.13 - Convergence of pressure for three turbulence models of the B-fan

Convergence time for the coarse mesh simulations of the B-fan were only a few hours. The refined mesh simulations of the B-fan, which had twice as many cells, converged after 10 hours of iteration. The computational time of Approach 1 varied between 25-30 hours whereas the large computational domains of Approach 2 resulted in some simulations only converging after 45-50 hours.

6 Results

Details of the experimental and numerical setups have been discussed in the previous two chapters. This chapter focusses on the results obtained in both cases. The numerical results are also compared to the experiments test results in order to validate the CFD simulations.

6.1 Experimental results

Three small scale fans (L1, L2 and N) were tested for five different blade-setting angles at different rotational speeds. The facility was refurbished between the tests of the L1-fan and L2-fans and therefore the L1-fan was the only fan tested on the non-refurbished test facility. The refurbished facility included a new drive system, data acquisition hardware and software and a torque transducer. Further details on the changes made to the test facility are discussed in Appendix A. The performance characteristics for each fan are also given in Appendix E.

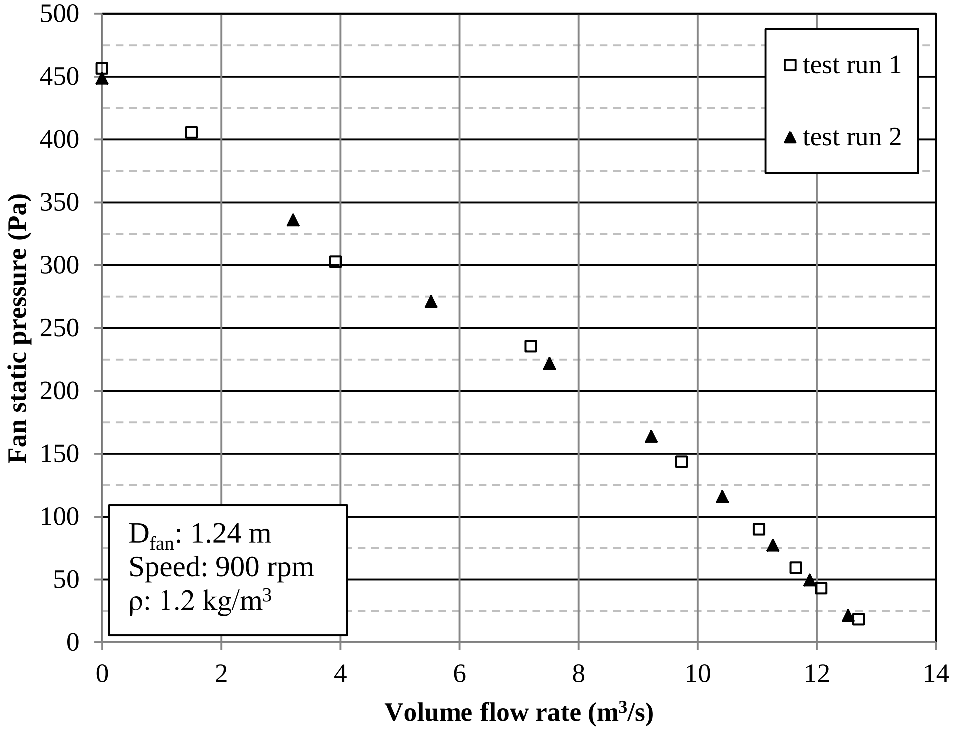

Figure 6.1 - Repeatability of the fan static pressure of the L2-fan for a blade-setting angle of 6.9°

The repeatability of all experimental tests was examined by comparing different test runs of similar operating conditions with each other. Figure 6.1 shows two tests of the total-to-static pressure performance for the L2-fan on different days. At higher flow rates (> 6 m^3/s) the repeatability of measurements for the pressure at the inlet bellmouth and settling chamber were very good ($\Delta p_s < 1\%$). Due to the small size of the fans relative to the size of the test facility, pressure differences at lower flow rates (see 0 m^3/s) became less repeatable ($\Delta p_s \sim$ 2%). Repeatability was found to be influenced by the ambient conditions, the drift observed in the pressure transducers and the calibration of all instrumentation. Repeatability for the torque and speed measurements was found to be similar to the pressure measurements.

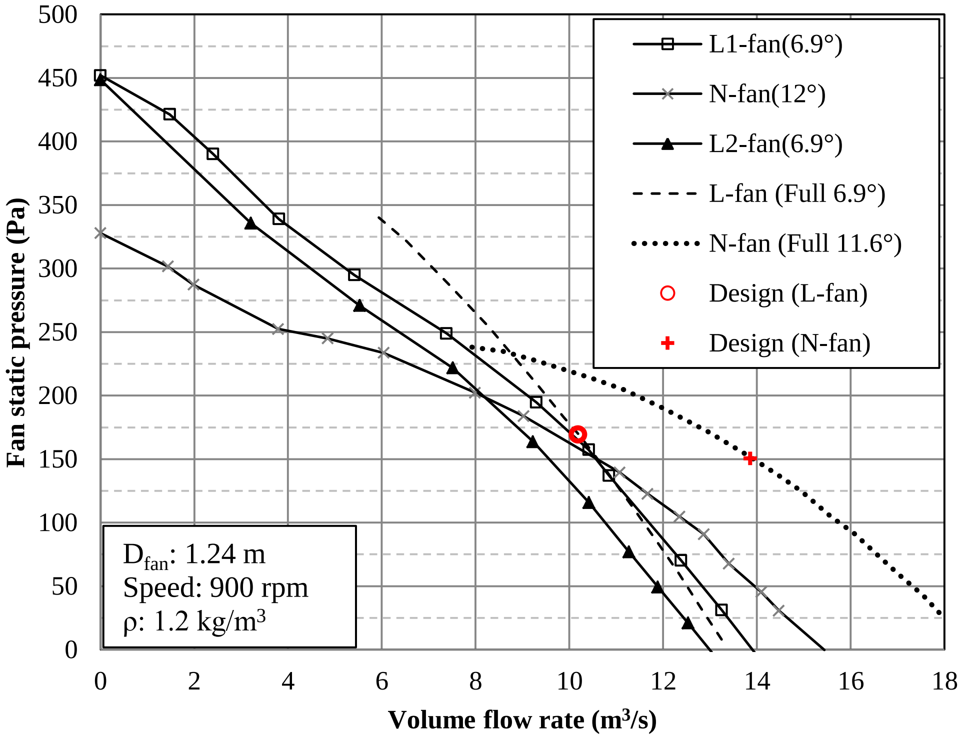

Figure 6.2 - Fan static pressure comparison between the full scale and the small scale N-, L1- and L2- fans

Figure 6.2– 6.4 compares the scaled models of the L1-, L2- and N-fan with the supplied full scale fan characteristics. For a comparative study between the scaled models and the full scale fan, the full scale data was scaled to the diameter (D = 1.24 m) of the small scale fans. The scaled design values of the full scale fans are given in Table 6.1.

Table 6.1 – Scaled values of the full scale L-fan and N-fan used in comparative study

	L-fan	N-fan
N	900 rpm	900 rpm
D	1.24 m	1.24 m
Q	10.18 m^3/s	13.86 m^3/s
p_s	169.43 Pa	150.56 Pa
P	2632.95 W	3343.57 W
η	65.5 %	62.42 %

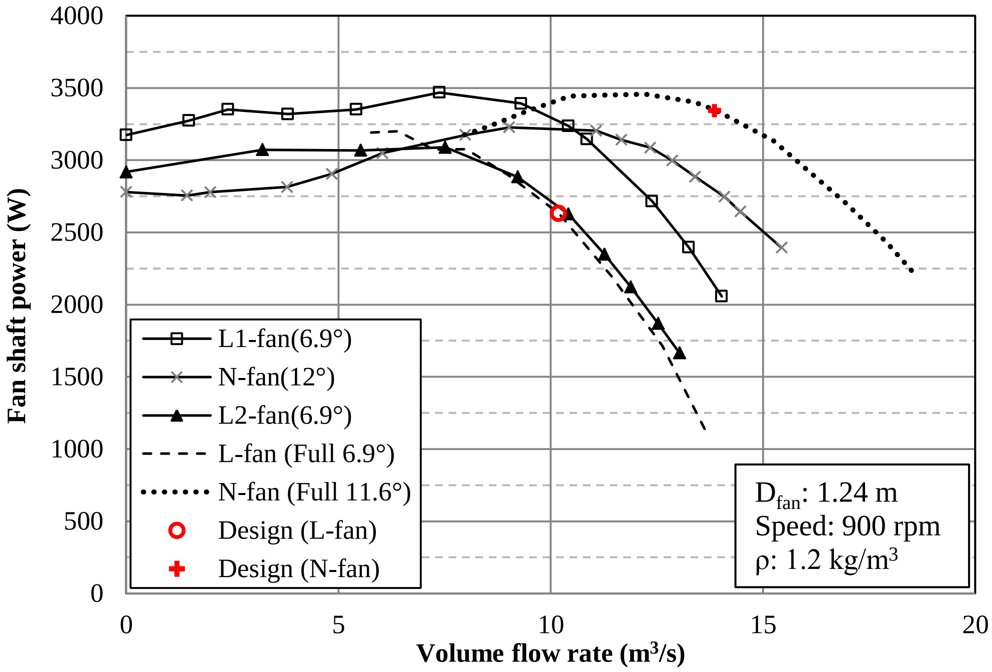

Figure 6.3 - Fan shaft power comparison between the full scale and the small scale L1-, L2- and N-fans

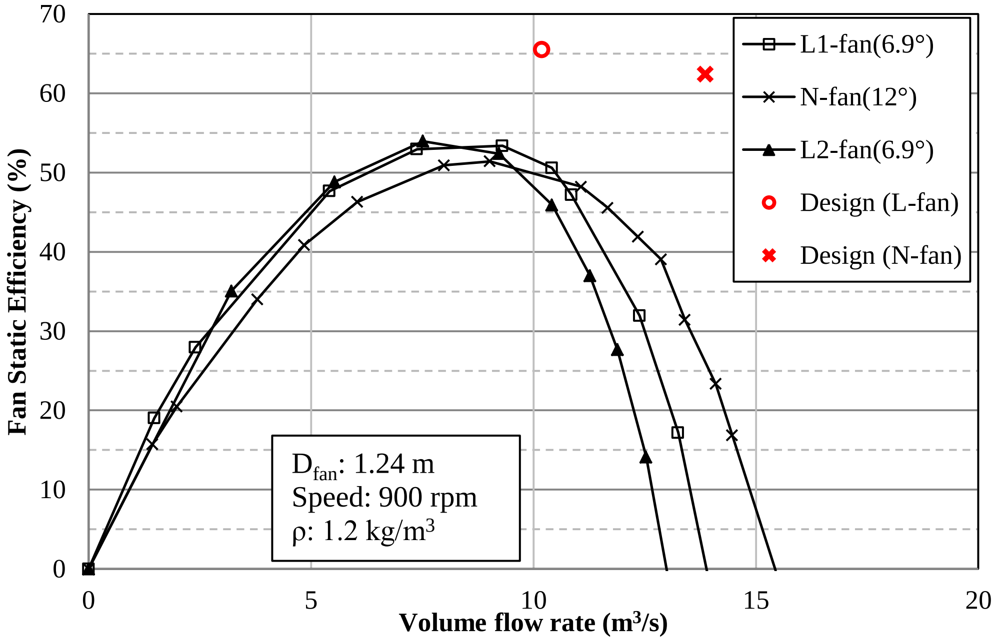

Figure 6.4 - Fan static efficiency comparison between the full scale and the small scale L1-, L2- and N-fans

Figure 6.2 shows the different fan static pressure maps of the various fans. Note that the supplied data of the full scale fans do not extend to the lower flow rate region. The figure indicates that the L1-fan and L2-fan follows the characteristic trend of the full scale model in the high flow rate region. For lower flow rates, this is not the case. It would also appear that the difference in pressure between the L2-fan and full scale model could be attributed to a difference in the blade-setting angle. A similar trend is also shown for the N-fan. It was mentioned earlier that the positioning of the protractor for setting the blade-setting angle differed slightly from the full scale models. Therefore the difference in pressures could be attributed to a difference in blade-setting angle. However, the fan shaft power map (see Figure 6.3) suggests otherwise as it shows very good correlation between the L2-fan and the full scale L-fan. The L1-fan's measurements consequently differ from the full scale fan power design values. It would appear that there is a relation between the blade-setting angle and the deviations between the full and small scale fans. Figure 6.4 shows the large difference in fan static efficiency between the full scale and small scale fans. The difference between the full scale fan static efficiencies and peak values of the tested fans is between 10-15 %.

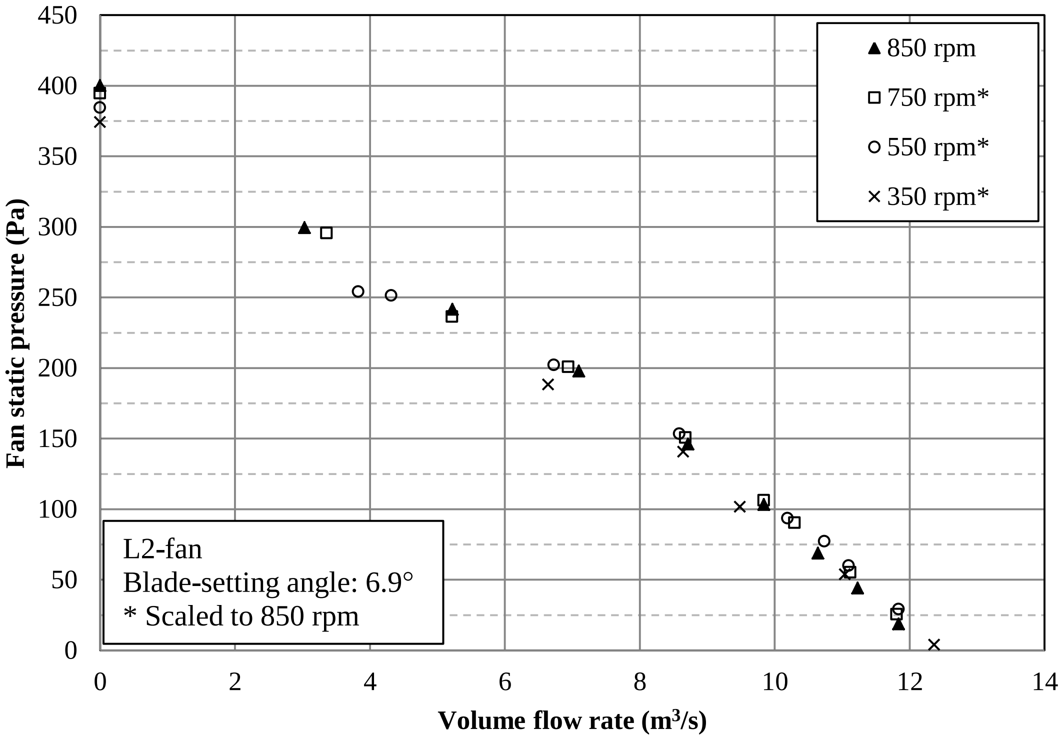

Figure 6.5 – Performance comparison for different rotational speeds of the L2-fan

The validity of the fan scaling laws (see Equations C.11 to C.13) was also examined by testing the L2- and N-fan at different rotational speeds. Figure 6.5 and Figure 6.6 show the scaled performance at various rotational speeds for the L2- and N-fan. In both figures the entire set of rotational speeds are scaled to the highest speed data set. Notice that the N-fan was only tested for 750 rpm and 550 rpm. This is due to large pressure fluctuations and reduced volume flow rates at rotational speeds lower than 550 rpm which resulted in inaccurate measurements. Excessive vibration of the N-fan at rotational speeds higher than 750 rpm also resulted in the fan not being tested at higher speeds. The experimental test values of the L2-fan at 350 rpm also deviated significantly from the rest of the measurements as shown in Figure 6.5. The inaccurate measurements in both cases can also be attributed to the instrumentation being insufficiently sensitive for the lower flow rates mentioned.

Despite the deviations found at the lower speeds, the comparisons between the various scaled data sets shown in Figure 6.5 and Figure 6.6, demonstrate the validity of using the fan scaling laws. This is based on the fact that the deviations shown in these figures are as a result of measurement error as explained earlier.

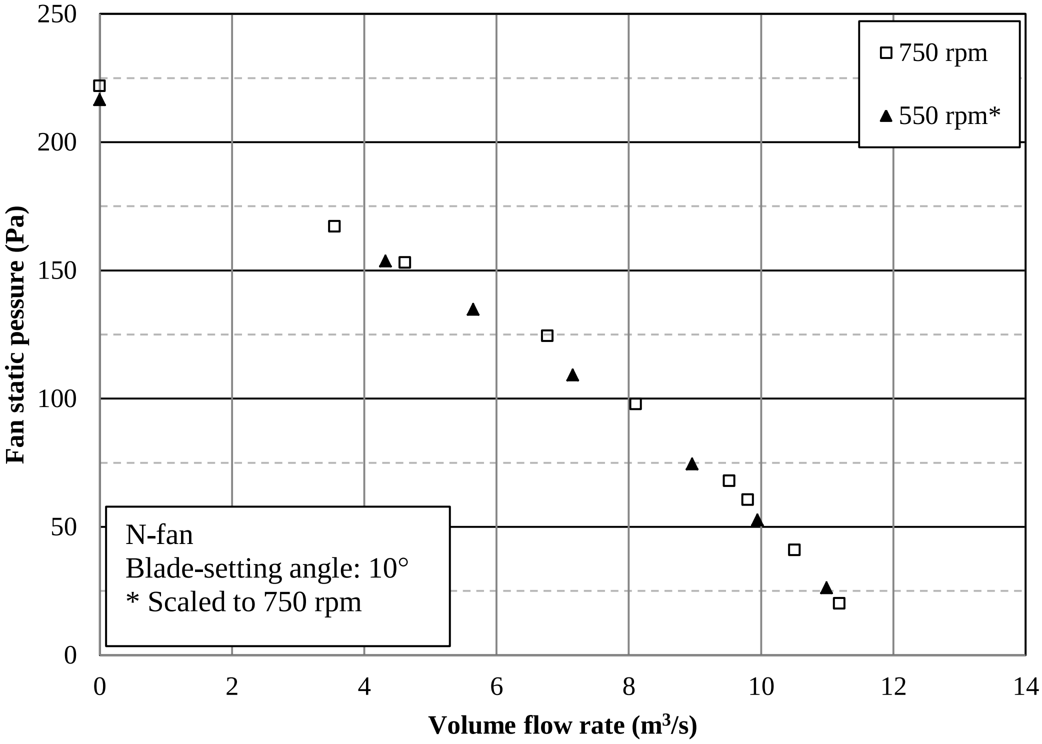

Figure 6.6 – Performance Comparison for 750 rpm and 550 rpm for the N-fan

6.2 Numerical results: B-fan

All simulations of the B-fan were carried out for a blade-setting angle of 59 degrees (as defined in Appendix D). Three operating points for each of the turbulence models were simulated: 12 m^3/s, 16m^3/s (design) and 20 m^3/s. Mesh independence was established and is indicated by Table 6.2 in which the pressure is compared for various operating points. Similar results were found for the power values. Although there are slight changes in the performance of the various meshes, the results indicate that mesh independence of the B-fan is established for a mesh of 10^6 target number cells and a y^+-value of 60. All simulations were carried out using the QUICK spatial discretization scheme. The SIMPLE pressure-velocity coupling algorithm was used. Specific attention to under-relaxation was not required and therefore default values specified by *ANSYS Fluent* were used.

Table 6.2 – Mesh independence of the B-fan for k-ε realizable turbulence model

$\dot{V}$ (m^3/s)	Mesh 1 (2 354 828 cells)	Mesh 2 (3 114 586 cells)	Mesh 3 (5 478 878 cells)
12	295.78 Pa	298.49 Pa	300.19 Pa
16	202.07 Pa	201.97 Pa	203.18 Pa
20	45.36 Pa	44.67 Pa	45.68 Pa

The results of the fan static pressure rise across the B-fan for the various turbulence models of mesh 3 (fine mesh) are shown in Figure 6.7. The area-averaged total pressure was measured at the inlet plane and the area-averaged static pressure measured at the outlet plane. The results show a large deviation between the numerical and experimental values at higher flow rates. However, better correlation is found at lower flow rates.

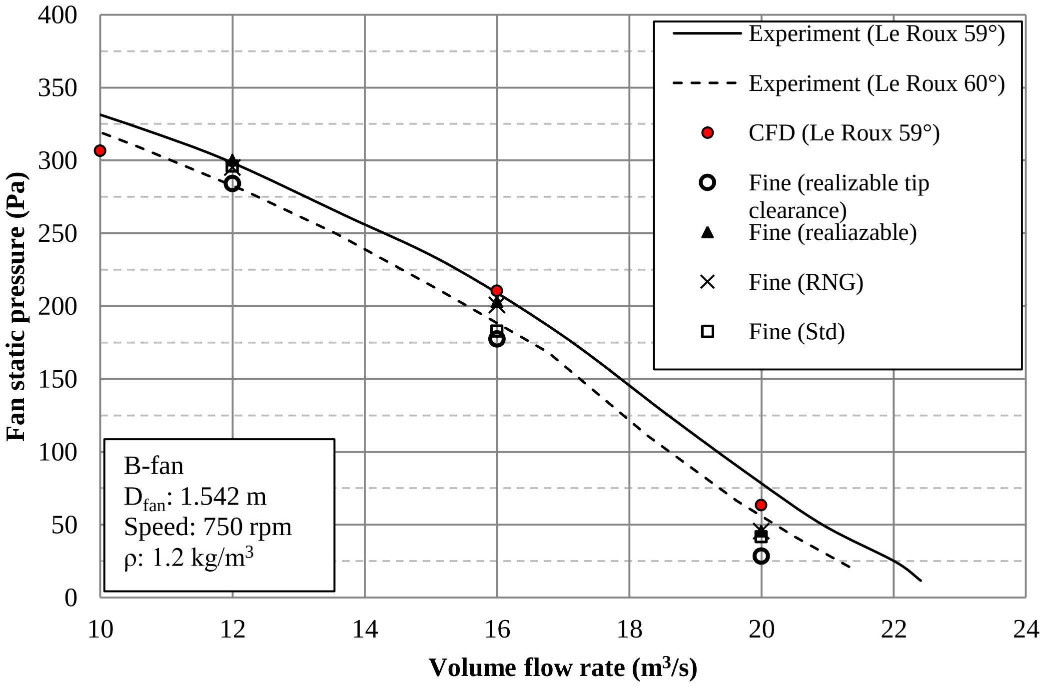

Figure 6.7 – Fan static pressure comparison between experimental and the three refined mesh numerical models of the B-fan

The fan shaft power performance values deviate significantly from experimental results for all flow rates as shown in Figure 6.8. An inconsistent trend in the fan power results compared to the pressure results is also noticed, with the fan power error becoming larger with decreasing flow rates. The numerical results of the B-fan correlate well with the numerical results of Le Roux (2010) for the fan static pressure and fan shaft power.

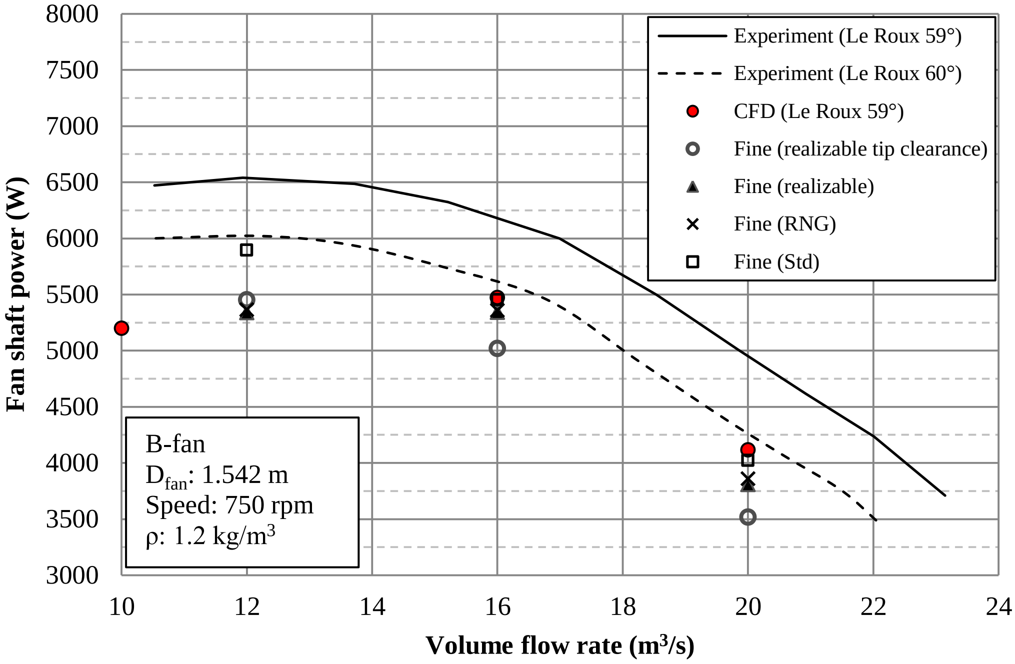

Figure 6.8 – Fan shaft power comparison between experimental and three refined mesh numerical models of the B-fan

With regards to the different turbulence models only small differences in performance were found between the RNG and realizable turbulence models. The standard k-ε turbulence model's results for pressure and specifically power differed substantially from the values of the other two models. The standard turbulence model under-predicted (less accurate) the pressure and over predicted the power (more accurate) relative to the other models. The RNG k-ε model was found to be very unstable compared to the other two models, which resulted in convergence taking longer. The realizable k-ε model, especially at lower flow rates (12 m^3/s) was found to be very stable relative to the other models.

There is also a prominent difference in performance between the no-tip clearance and 3 mm tip clearance case. The tip clearance resulted in a fairly constant reduction in fan static pressure of approximately 20-25 Pa. A similar trend for the fan power is found although at lower flow rates this tendency seems to disappear. A drop of approximately 500 W is found between the two higher flow rate cases. Furthermore, it was noticed that the experimental results for a blade-setting angle of 60 degrees compared more favourably with the numerical results. This merely raises the question whether the definition of experimental and numerical blade-setting angles are the same. Due to the fact that no experiments were carried out for the B-fan no further examination of this conjecture was performed.

The results of the B-fan's simulations indicated the unexpected good performance of the standard k-ε turbulence model compared to more recent formulations. It was found that when the exact same simulation was carried out for a standard k-ε turbulence model without the Enhanced Wall Treatment a drop in pressure (4 %) and power (1 %) was observed. However, based on the results of the B-fan's simulations and the literature study, as discussed in Chapter 2, all further simulations were carried out using the realizable k-ε turbulence model in conjunction with the Enhanced Wall Treatment.

6.3 Numerical results: L2- and N-fan

The results of the L2- and N-fan discussed below include the simulations of Approach 1 and Approach 2. As mentioned in Chapter 5, the mesh sizes of these two approaches were not conducive to mesh independence tests because of the large number of cells. Approach 1 represents the shortened annular inlet and outlet and Approach 2 the large domain resembling the BS 848 test facility. The QUICK spatial discretization scheme was used and the SIMPLE algorithm was used for pressure-velocity coupling. It was, however, noticed that there was no significant change in Approach 1's simulation results when the first-order upwind scheme was used. On the other hand the QUICK scheme provided better results for the larger domain of Approach 2.

Under-relaxation was required for the L2- and N-fan's simulations, particularly at higher flow rates. Approach 1's simulations were especially sensitive to the pressure and momentum under-relaxation factors and values between 0.15-0.25 were used for the pressure and 0.6 for momentum settings.

6.3.1 L2-fan

The L2-fan was simulated for the design blade-setting angle of 6.9 degrees in both approaches. The design flow rate is equal to 10.18 m^3/s and is indicated by the red-filled marker. The fan static pressure was calculated by the sum of the area-averaged total pressure at the inlet and area-averaged static pressure at the outlet. Figure 6.9 compares the experimental and numerical results for the 6.9 degree L2-fan. Excellent agreement with experimental results was found for the entire flow rate region except at a 0 m^3/s. If one considers the pressure values of Approach 1, an increase in error is observed with a decrease in the flow rate. On the other hand the opposite trend is observed for Approach 2. A deviation of only 0.25 % for Approach 2 is found at 3 m^3/s. The largest percentage pressure deviation for Approach 1 is 5.23% at 3 m^3/s and 7.6% for Approach 2 at 12 m^3/s.

In contrast to the fan power results of the B-fan, the L2-fan's numerical results for fan power show much better agreement. Figure 6.10 shows that the fan power of the shortened domain is under-predicted for all operating points, although very good correlation is found for the fan power of Approach 2. Besides the larger deviation at 0 m^3/s, which is expected, the largest percentage deviation for both approaches is below 8% (3 m^3/s for Approach 1) and a difference of only 0.8 % is observed for Approach 2 at 3 m^3/s.

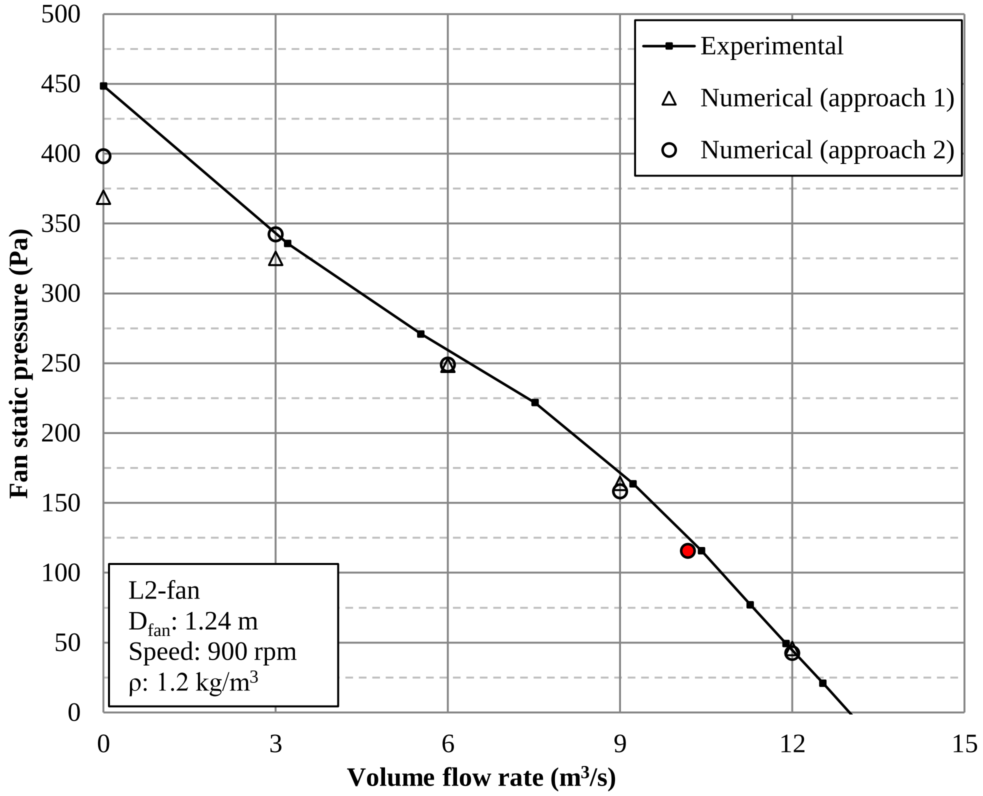

Figure 6.9 - Fan static pressure CFD validation of the 6.9° L2-fan

Due to the good correlation shown for the fan static pressure and fan shaft power, good correlation for the static fan efficiency is expected. Figure 6.11 shows that the fan static efficiency of Approach 1 tends to be slightly over-predicted. This is largely due to the under-prediction of the fan shaft power. The fan static efficiency results of Approach 2 on the other hand are only slightly (~1.5%) under-predicted. In general very good agreement between experimental and numerical values of the L2-fan is found for both approaches.

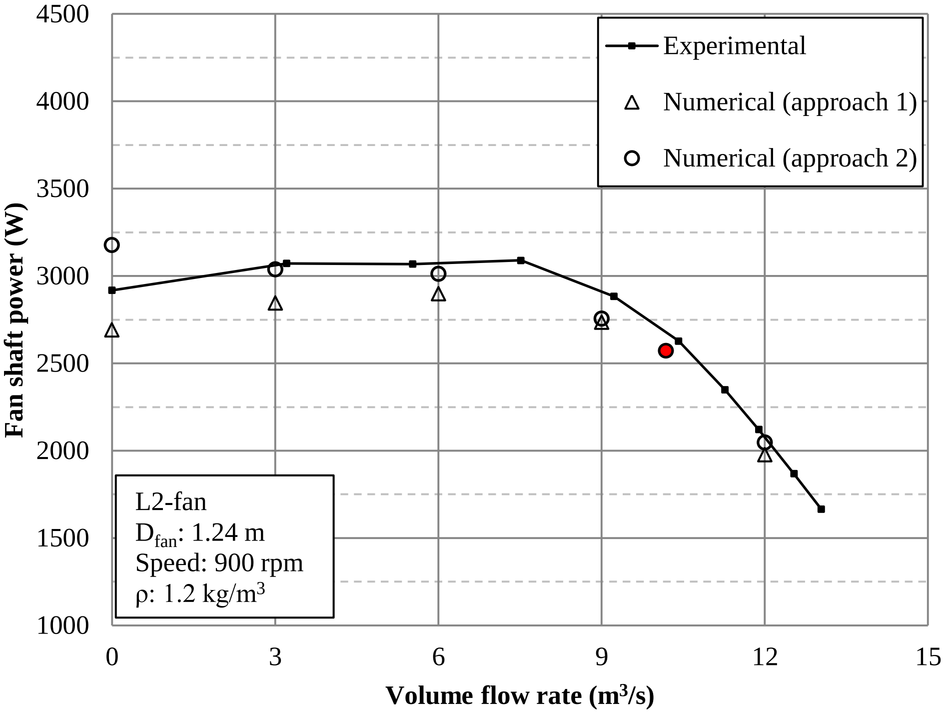

Figure 6.10 - Fan shaft power CFD validation of the 6.9° L2-fan

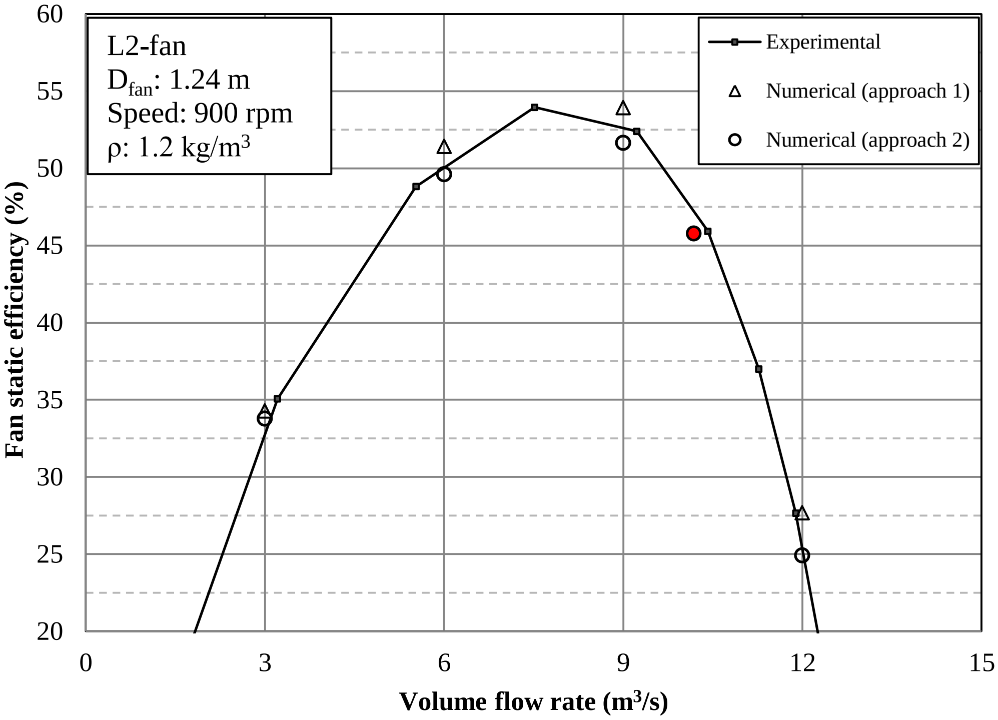

Figure 6.11 - Fan static efficiency CFD validation of the 6.9° L2-fan

6.3.2 N-fan

The N-fan was simulated for a blade-setting angle of 12 degrees. Due to the flow rate operating range of the N-fan being larger than that of the L2-fan the simulated operating points differed from the L2-fan's simulation.

Figure 6.12 shows the fan static pressure for the 12 degree blade-setting angle of the N-fan. As was the case with the L2-fan, very good agreement between the experimental and numerical results was found. Better correlation between Approach 1 and experimental values are also found if compared to the L2-fan. Similar results for pressure values with regards to Approach 2 was found although the fan power for the 3 m^3/s operating point is over predicted by 4%. If the 0 m^3/s case is not considered, the largest percentage deviation in pressure is 7% for Approach 2 at 7 m^3/s. The fan power of the N-fan in Figure 6.13 shows very good correlation, especially with regards to the results of Approach 1.

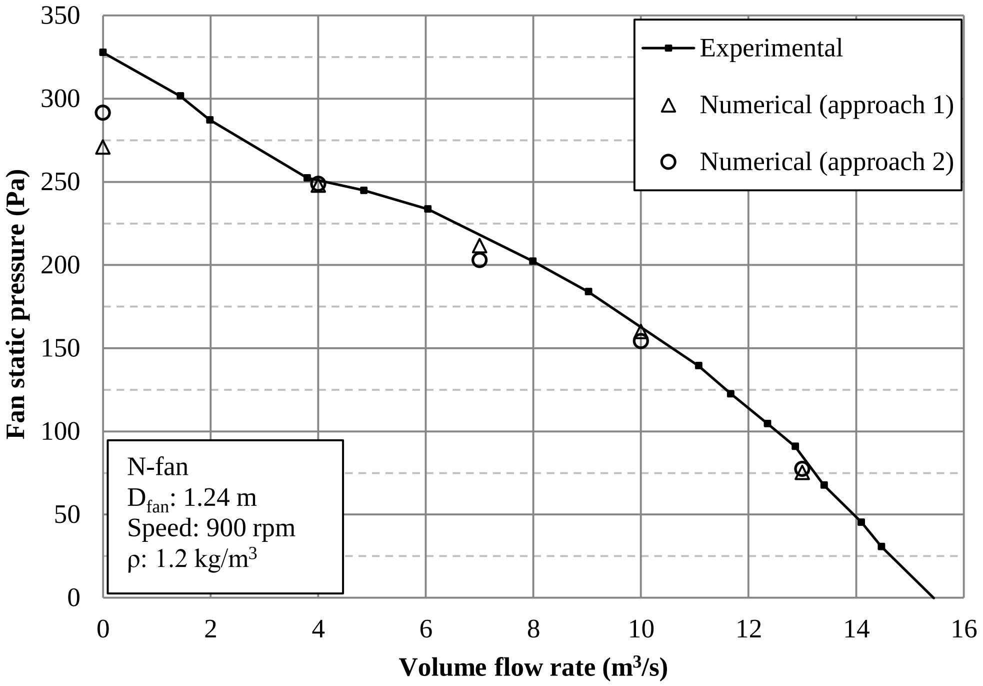

Figure 6.12 – Fan static pressure CFD validation of the 12° N-fan

The fan static efficiency for Approach 1 shows excellent agreement with experimental results although the results of the larger domain slightly (~2%) under predicts the fan static efficiency. Furthermore, very good correlation for the operating points of Approach 2 is also found, except for the larger deviation found at 7 m^3/s.

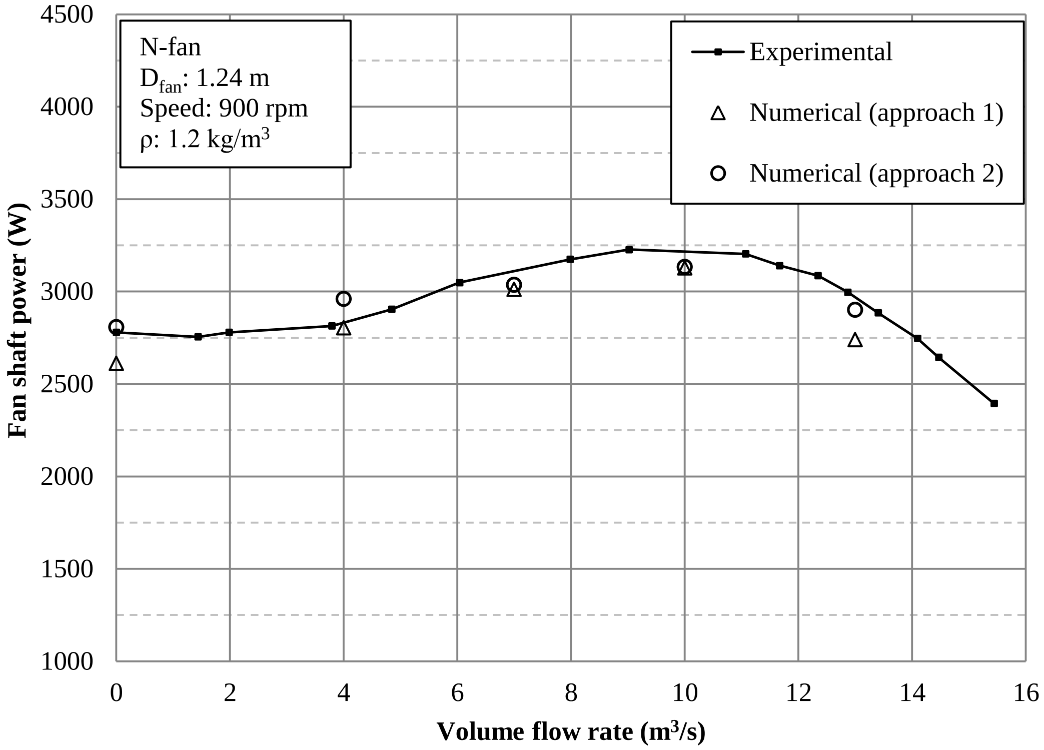

Figure 6.13 – Fan shaft power CFD validation of the 12° N-fan

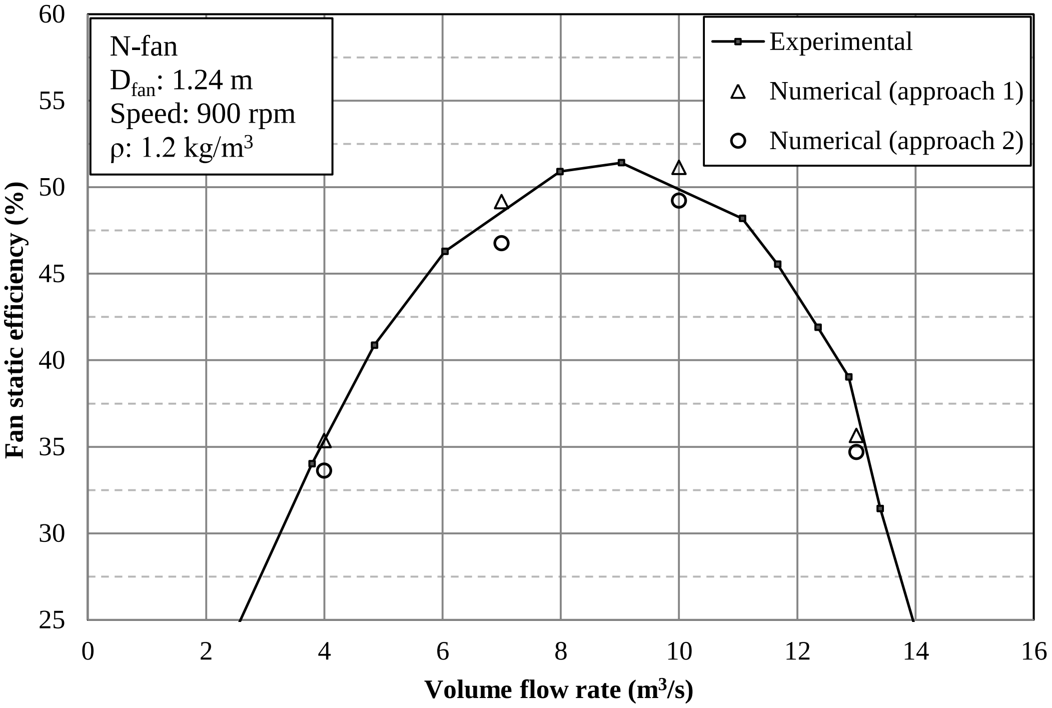

Figure 6.14 - Fan static efficiency CFD validation of the 12° N-fan

6.4 Flow visualization

Figure 6.15 shows the flow fields for the design flow rate (10.18 m^3/s), 6 m^3/s and 3 m^3/s of the L2-fan. The streamlines are released from a plane (y = 0) and do not cross periodicity.

The streamlines in all three cases show that the air is entrained into the outlet domain, resulting in large amounts of backflow at the upper boundary. It also indicates that there is very little (if any) backflow over the downstream outlet boundary. Air exits the boundary at the upper boundary for the lowest flow rate case which also shows circulation in the inlet domain. This is due to air being sucked from the fan outlet through the fan passage and blown out on the inlet side. The absence of streamlines at the outlet of the fan passage indicates that the flow is characterized by a large relative swirl component. This is also seen further downstream of the fan outlet for the 3m^3/s case.

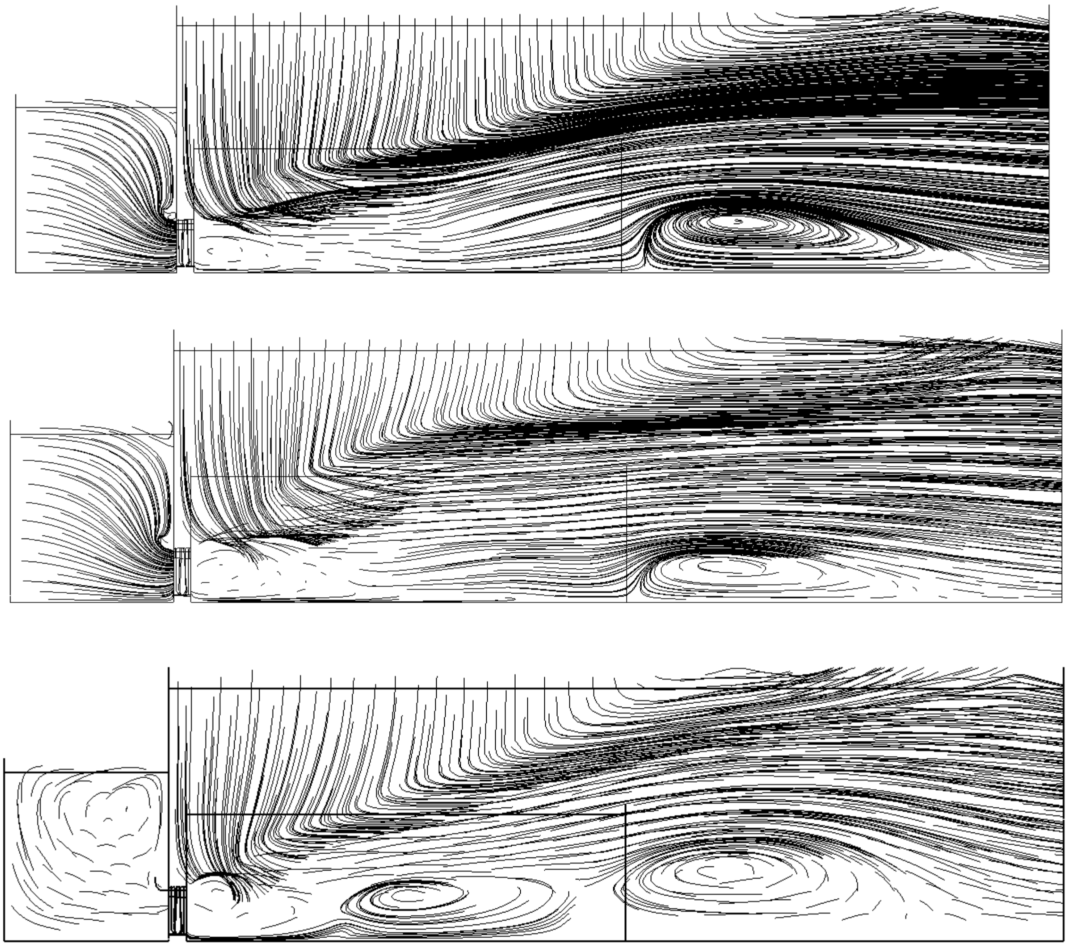

Figure 6.15 - Flow visualization of the L2-fan for 10.18 m^3/s (top), 6 m^3/s (middle) and 3 m^3/s (bottom)

One would expect the flow fields of the two fans to have similar characteristics. Figure 6.15 and Figure 6.16 indicate that the flow field in the region close to the fan outlet are similar. However, the validity of the large circulation zones found in both fans' flow fields cannot be verified. Another interesting observation is made at 4 m^3/s (Figure 6.16) where there is no backflow observed over the fan inlet boundary. This explains the absence of a circulation zone in the inlet domain for the low flow rate of the N-fan.

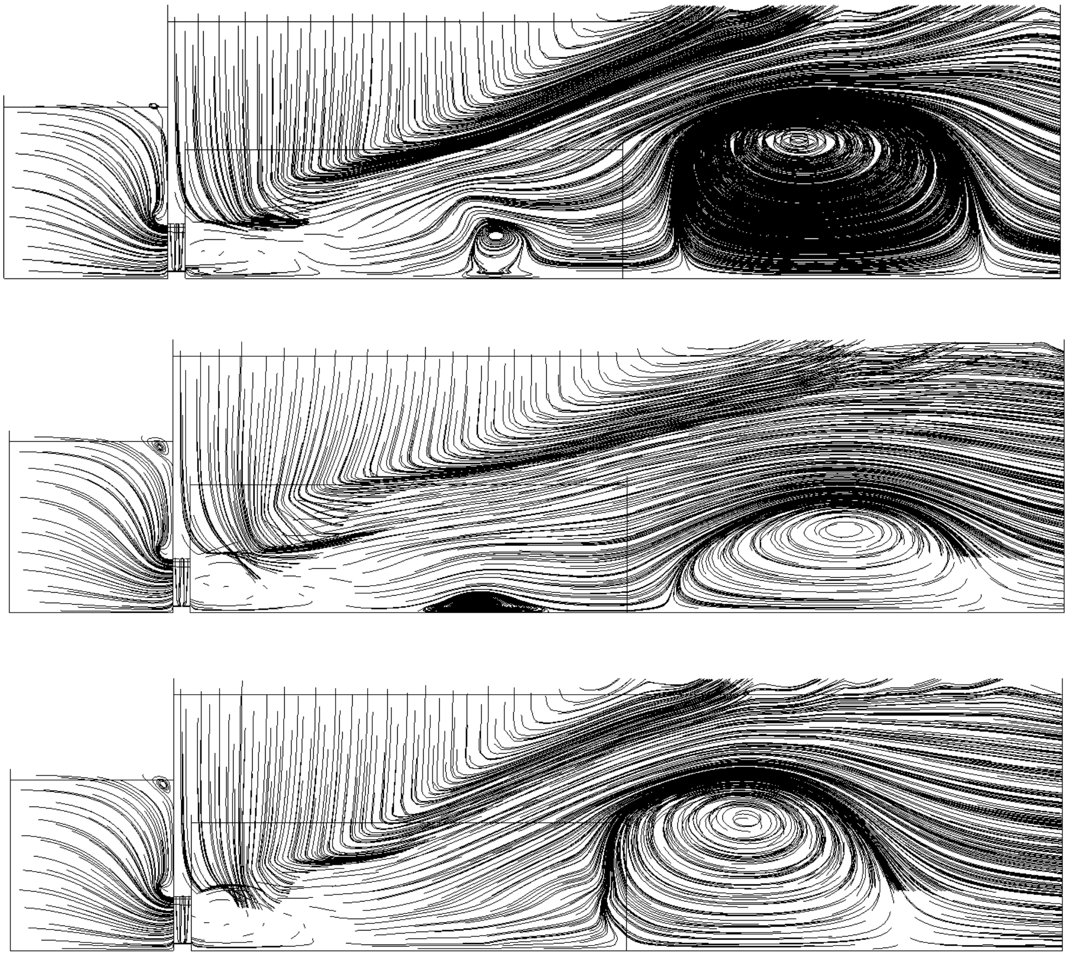

Figure 6.16 - Flow visualization of the N-fan for 10 m^3/s (top), 7 m^3/s (middle) and 4 m^3/s (bottom).

Figure 6.17 shows the flow field around the blade passage domain for the design (10.18 m^3/s) and 3 m^3/s volume flow rate of the L2-fan. The blue domain (inlet, passage and outlet passage) represents the rotating domain of the simulation. The blue streamlines represent air entering the rotor domain from the inlet and outlet. The black streamlines represent air exiting the domain. The figures below do not show cross periodicity which explains why the streamlines in the 3 m^3/s case are shorter at the inlet side. This also indicates that the flow has a large tangential component. For both cases backflow into the rotor domain is observed. Due to the large radial component of the flow at the outlet in the 3 m^3/s case, large amounts of air flow back into the domain. In this specific case a small volume of air also cross the inlet boundary and exits into the inlet domain which results in the large circulation zone observed in Figure 6.15 (bottom).

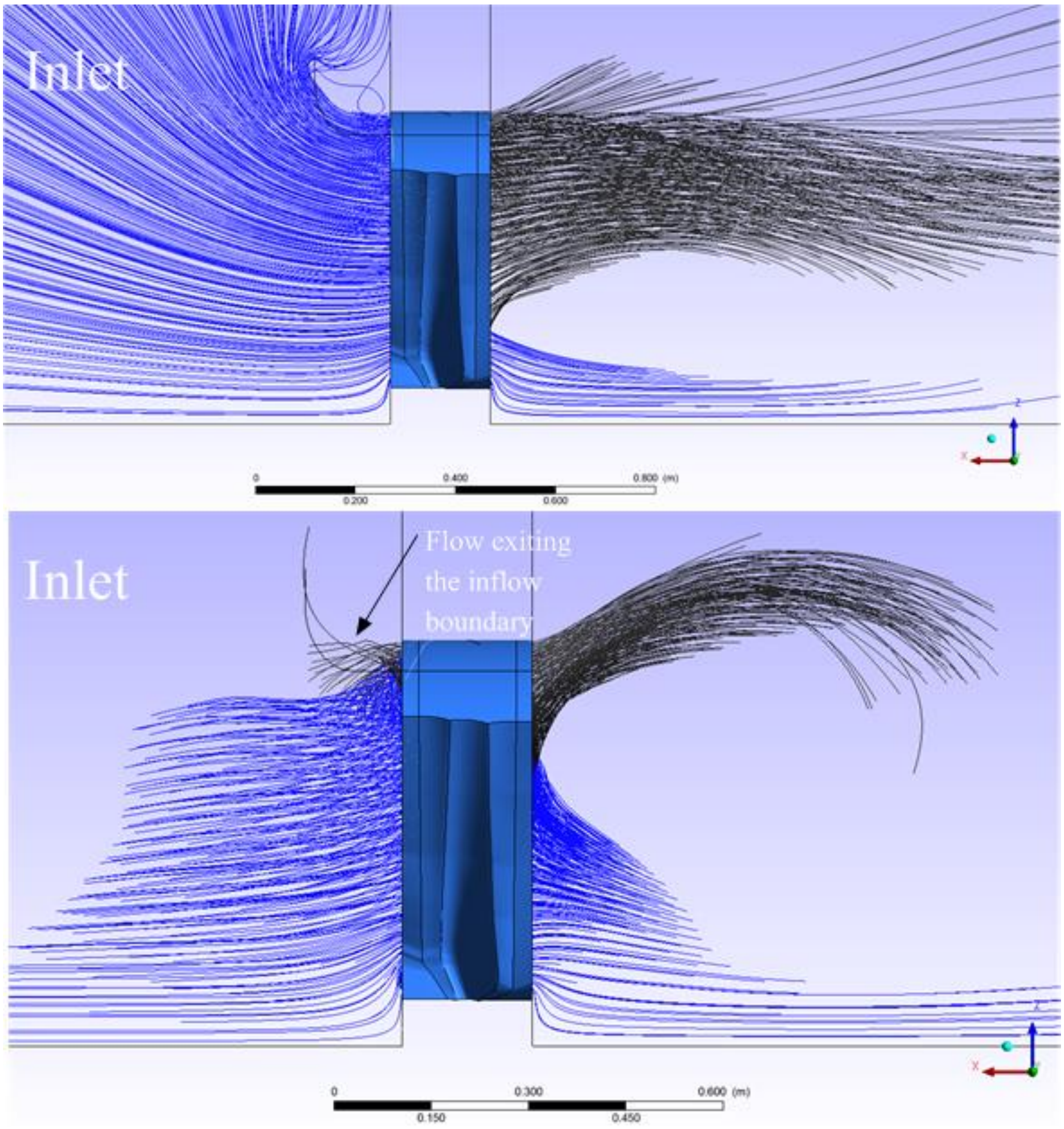

Figure 6.17 - Flow entering and exiting the blade passage domain for the design, 10.18 m^3/s, (upper) and 3 m^3/s (lower) volume flow rate of the L2-fan.

7 Conclusion and Recommendations

Being able to numerically simulate any physical process or operation accurately holds many obvious advantages. Besides the fact that numerical simulations can save time and money, it also allows one to investigate and understand the factors which influence these processes and operations. A better understanding of these factors results in better, revolutionary designs which lead to more cost effective and efficient projects.

With regulations such as the minimum energy efficiency requirements for fans implemented in Europe the need to understand the factors that affect the efficiency of these turbomachines better, has increased. This study focused on the possibility of simulating axial fans accurately using multiple rotating reference frames. A methodology and approach to simulating axial fans had to be developed. This would enable future research to focus on the details of the flow field rather than the method. Reversed engineered numerical solid models were created by three dimensional scanning procedures for numerical simulation purposes. ANSYS *Fluent* was chosen as the software to be used for all numerical simulations. The numerical simulations of the geometric models were validated by experimental tests carried out in a BS 848 fan test facility.

This thesis contains the details regarding the process of developing a reversed engineered fan blade solid model, the procedure and instrumentation used for the experimental testing of the L1-, L2- and N-fan, the details of the numerical simulations and discussions behind the computational domain, mesh and turbulence models. Concluding remarks on these aspects follows.

7.1 Numerical fan models

Numerical models of the L1-, L2- and N-fan were successfully generated from three dimensional scanning procedures. Two methods of scanning were used: contact and non-contact scanning. The contact scanning data was used to generate these models since the non-contact scanner data was considered to be inaccurate. However, based on the simplification of the curves that was later required for mesh generation the non-contact scanner data may be regarded as sufficiently accurate for the purposes of generating a numerical fan model.

A numerical model of the B-fan was also generated and the method described. Although the design details of the B-fan are given by Bruneau (1994), certain specifications such as the stagger angle and camber line were not defined. Therefore the design method has been discussed and a stagger angle and camber line distribution is proposed for future studies.

7.2 Experimental tests

The L1-, L2- and N-fan were tested in a Type A, BS 848 fan test facility for their complete operating ranges. Each fan was tested for five different blade-setting angles. To determine each fan's efficiency the pressure rise across the fan, volume flow rate and fan power were measured. The test results were satisfactory and repeatability of measurements was acceptable.

The test facility was refurbished to allow for accurate test results. The bridge amplifier, A/D converter and measuring software were replaced by an HBM *Spider8* unit which acts as a bridge amplifier and A/D converter. CATMAN *Easy* software was used in conjunction with the *Spider8*. A new torque transducer was installed which required the drive system to be redesigned. The new drive system consisted of fewer couplings and bearings which reduced frictional and mechanical losses. It also allowed for higher rotational speeds of the various fans as the new drive system reduced vibration and shaking of the fan.

The L1- and L2-fan had very similar geometries, the most obvious difference being the thickness distribution. The thicker L1-fan profile attained higher pressure rises for a specific flow rate although it used more power. Therefore, although the L1- and L2-fans differed in general performance their efficiency characteristics were very similar. The 9-bladed N-fan, having a shorter chord length, attained higher flow rates in the lower pressure region but is characterized by lower overall efficiency operation. Interestingly the N-fan was found to be more efficient with a decrease in blade-setting angle. This trend is not observed for the L-fans.

The performance of the scaled and full scale fans at the design point did not agree well. The combined effect of the deviations led to the fan static efficiency deviating significantly (20-24 %) from the experimental results. A study by Pelz et al. (2012) on the influence of Reynolds number on the fan efficiency of axial and centrifugal fans stated that the fan efficiency is directly proportional to a change in the Reynolds number and the physical size of the fan. Figure 7.1, presented by Pelz et al. (2012), shows the large difference in efficiency for two experimentally tested scaled models (with very similar surface finishes) of the same axial fan. The smaller ($Re = 0.89E6$) fan's maximum efficiency is 7% less than the larger ($Re = 7.56E6$) fan's maximum efficiency. This may explain the difference between the full and small scale fan results shown in Figure 6.2 to Figure 6.4.

Pelz et al. (2012) suggests that the difference in efficiency can be explained by the proportional relation $\Delta\varphi \sim \Delta\eta$ where φ is the flow coefficient. A change in the Reynolds number results in a change in boundary layer thickness, especially on the suction side of the blade. This affects the function of the stagger angle and therefore affects the performance of the fan. It is proposed that the scaling of axial fan models should include adjusting the flow coefficient φ by a $\Delta\varphi$ correction. For small stagger angle ($\Delta\beta$) changes it is shown that $\Delta\beta \approx \Delta\varphi$ and possibly explains the observations made in Section 6.2.

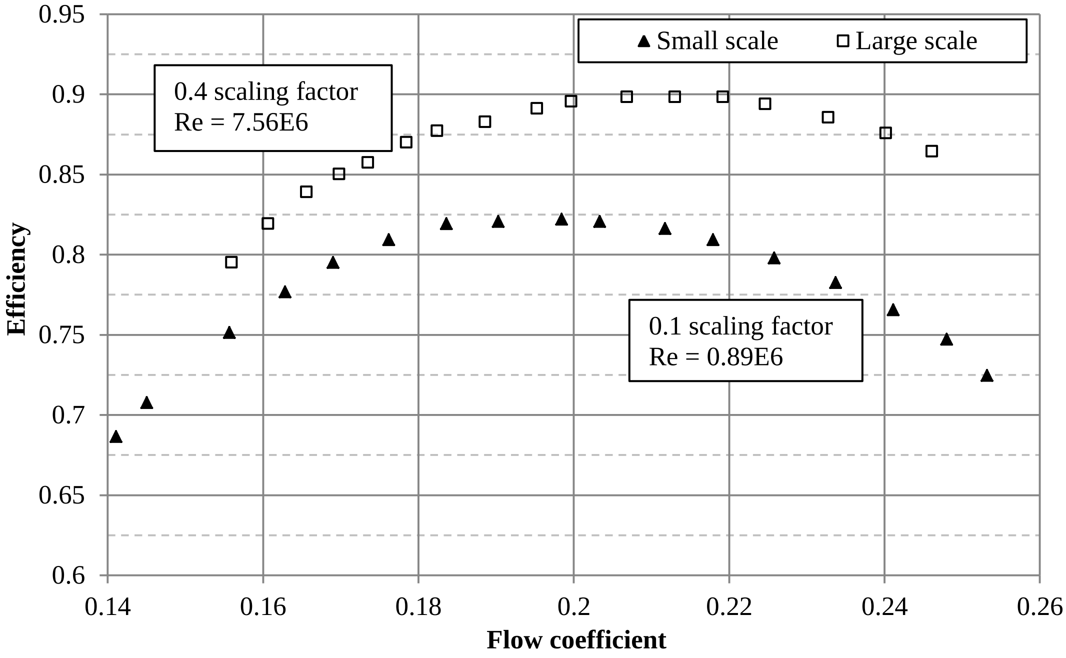

Figure 7.1 - Comparison between two Reynolds number efficiencies for the same fan (Pelz et al., 2012).

7.3 Numerical

Numerical simulations were carried out for the B-fan and two scaled fan models, the L2- and N-fan, using ANSYS *Fluent*. The B-fan was only simulated in a simplified domain, investigating three different k-ε turbulence models (standard, RNG, realizable) with the purpose of developing a method for simulating the reversed engineered numerical fan blade models of the L2-fan and N-fan. Once the method was established importing the numerical models into ANSYS *BladeModeler* and the seamless integration with ANSYS *TurboGrid* resulted in accelerated set-up times for simulations. ANSYS *TurboGrid* was found to simplify and streamline the mesh generation process of the fan passage. However, ANSYS *TurboGrid* has certain limitations with regards to the inlet and outlet's length and size. Therefore, if larger domains were required it had to be created in ANSYS *Meshing*, ANSYS's general meshing software package.

The entire mesh of the B-fan was created using ANSYS *TurboGrid*'s structured mesh generation software. These meshes consisted of three parts, an inlet, passage (rotor) and outlet. The inlet and outlet domains were annular ducted sections. All simulations which include the L2- and N-fan used a steady state, multiple rotating reference frame, approach. Simulations were carried out for three mesh refinements at 12, 16 and 20 m^3/s. Validation of the B-fan's numerical results were done by using the experimental results from Le Roux (2010). The correlation between the numerical and experimental results is regarded as acceptable although there are large deviations found for the fan power. Due to the fact that the fan was never tested during this study no further conclusions can be drawn.

The same methodology used to simulate the B-fan was consequently implemented to simulate the L2- and N-fan. Two computational domains (Approach 1 and 2) were investigated for each of these fans. The first domain resembled the B-fan's domain and the second a larger domain resembling the BS 848 test facility with open atmosphere outlet conditions. All numerical fan models were simulated with a 5 mm tip clearance using the realizable k-ε turbulence model and ANSYS *Fluent*'s Enhanced Wall Treatment.

Very good correlation for both fans was found for a large flow rate operating range. The largest deviation in fan static pressure for both fans of both approaches was 8 %. The good agreement between the experimental and numerical results for the fan static efficiency further supports the validity of these simulations.

The good results of the L2- and N-fan simulations suggest that a simplified domain such as Approach 1 (annulus inlet and outlet) can accurately predict the performance of an axial fan. This is advantageous due to its reduced computational size which reduces computational resources and time compared to Approach 2. Notwithstanding, the value of the excellent agreement of the large open atmosphere simulations with experimental results must not be overlooked as most numerical work in literature has found to be on simplified, small scale, domains. The ability of the realizable k-ε turbulence model in combination with the Enhanced Wall Treatment to accurately model the lower flow rate operating range is encouraging for future numerical work.

Improved results were found in comparison to similar studies (e.g. Le Roux, 2010) which have focussed on the numerical modelling of axial fans in test facilities which differ from the typical inlet and outlet duct setups. The good agreement of the L2- and N-fan's numerical results with its experiments validates not only the numerical results but the methodology and approach.

However, the methodology used in this thesis can still not be regarded as a replacement for the simplified approaches used to model large ACSCs. Louw (2011) using the ADM approach, as an example, modelled an ACSC with 192 fans using approximately 12 million cells. For the same amount of cells using the explicit approach one would only be able to model one full fan domain. Therefore, both approaches have a function in analysing ACSCs as the explicit model cannot yet replace the simplified approaches. As computational power increases in the future the feasibility of the explicit model on a larger scale will become possible. The methodology used in this study must, however, be seen as a tool to accurately validate axial fans with the ability to model multiple fans of an ACSC.

Furthermore, it is concluded that accurate simulations of axial fans require a large number of mesh elements (especially compared to simplified methods such as the pressure jump and ADM approaches). It has been found that in the case of the L2- and N-fan domains required at least two million cells in the passage and another two million for the outlet. The smallest domains had a total of approximately five million cells. Regions of specific importance were the tip clearance, the regions close to the shroud at the interfaces, the near-wall region at the blade surface and the mesh region at the outlet.

Due to the fact that it is very difficult (almost impossible) to accurately measure the performance of an ACSC in reality the validation of any simulation can only produce a good approximation of the operating performance. Modelling the fans, which has a significant effects on the performance of an ACSC, explicitly can be regarded as one step closer to reality. In the far future this would enable time-dependent simulation of the entire ACSC.

Recommendations for future work

Although this study has reached its objectives there are many aspects to the simulation of axial fans that still haven't been fully investigated. It is recommended that the following areas are further researched in the future:

- The reverse engineering of numerical fan models. This includes finding ways of obtaining the design specifications from a scanned blade profile such as the camber line, thickness distribution and stagger angles. Standardized guidelines with regards to post-editing of the scanned blade profiles should be laid out to facilitate and regulate this process. The use of non-contact scanning methods for future work is also recommended.
- The feasibility of large domain simulations has been proven. It is recommended that future studies involving simulation of axial fans should investigate the following numerical aspects:
    - The effect of the outlet mesh. Is there any correlation between the performance (especially the fan power) the size and refinement of the outlet mesh?
    - The low-Reynolds number and transition region – the use of the k-ω SST turbulence model to improve performance in the low flow rate region.
    - Factors affecting the rotational domain. How far should the interfaces be from the rotating fan blade? How do non-conformal interfaces affect the performance of simulations?
    - Meshing software. Although ANSYS Meshing is adequate for general use, it is recommended that specialized meshing software packages such as ANSYS *TGrid* be considered for the fan blade region.
    - Transient, non-periodic simulations. Although these simulations are resource intensive it may be feasible for

smaller domains using a RANS approach such as the realizable k-ε turbulence model. However, the value that non-periodic steady state simulation will add to the understanding of the flow field is questionable.

8 References

Amano, R.S., Lee, E.K., Xu, C., Xie, J., 2005. Investigation of the unsteady flow generated by an axial fan: experimental testing and simulations. International Journal of Rotating Machinery 3, 256–263.

ANSYS Fluent, 2011. ANSYS Inc. - Fluent theory guide.

Bamberger, K., Carolus, T., 2012. Optimization of axial fans with highly swept blades with respect to losses and noise reduction, in: Proceedings of FAN 2012 Conference. France.

Berg, T., Wikström, A., 2007. Fan modelling for front end cooling with CFD. Master’s thesis. Lulea University of Technology.

Borello, D., Corsini, A., Rispoli, F., Sheard, A.G., 2012. Investigation on the unsteady aerodynamics of an industrial fan, in: Proceedings of FAN 2012 Conference. France.

Bredell, J., Kröger, D.G., Thiart, G., 2006. Numerical investigation of fan performance in a forced draft air-cooled steam condenser. Applied Thermal Engineering 26, 846–852.

Bruneau, P., 1994. The design of a single rotor axial flow fan for a cooling tower application. Master's thesis. Department of Mechanical and Mechatronic Engineering. Stellenbosch University.

Cezario, C.A., 2012. CFD electric motor external fan system, in: Proceedings of FAN 2012 Conference. France.

Cyrus, V., Cyrus, J., Panek, P., 2012. Design and aerodynamic performance of a high pressure axial flow fan, in: Proceedings of FAN 2012 Conference. France.

De Gennaro, M., Kuehnelt, H., 2012. Broadband noise modelling and prediction for axial fans, in: Proceedings of FAN 2012 Conference. France.

Fernandez Oro, J.., Arguelles Diaz, K.., Santolaria Morros, C., Galdo Vega, M., 2011. Numerical simulation of the unsteady stator-rotor interaction in a low-speed axial fan including experimental validation. International Journal for Numerical Methods for Heat & Fluid Fllow 21, 168–197.

Guedel, A., Robitu, M., Chaulet, V., 2012. CFD simulations to predict the energy efficiency of an axial fan for various casing configurations, in: Proceedings of FAN 2012 Conference. France.

Heß, M., Pelz, P.F., 2010. On realiable performance prediction of axial turbomachines, in: Proceedings of ASME Turbo Expo 2010: Power for Land, Sea and Air. Glasgow, UK.

Hotchkiss, P.J., Meyer, C J, Von Backström, T W, 2006. Numerical investigation into the effect of cross-flow on the performance of axial flow fans in forced draught air-cooled heat exchangers. Applied Thermal Engineering 26, 200–208.

Howden, 2007. E-series Axial Flow Cooling Fans, Machinery.

Iwase, T., Kishitani, T., Furukawa, M., 2012. Influence of blade number on aerodynamic air-conditioner, in: Proceedings of FAN 2012 Conference. France.

Jian-Hui, Z., Chun-Xin, Y., 2008. Design and Simulation of the CPU Fan and Heat Sinks. IEEE Transactions on Components and Packaging Technologies 31, 890–903.

Kays, W., Crawford, M., Weigand, B., 2004. Convective Heat & Mass Transfer. McGraw-Hill Companies.

Kroger, D.G., 1998. Air-cooled Heat Exchanger and Cooling Towers.

Launder, B.E., Spalding, D.B., 1974. The Numerical Computation of Turbulent Flows. Computer Mehtods in Applied Mechanics and Engineering 3, 269–289.

Le Roux, N., 2010. The CFD simulation of an axial flow fan. University of Stellenbosch. Master's thesis. Department of Mechanical and Mechatronic Engineering. Stellenbosch University.

Lin, S., Tsai, M., 2011. An integrated study of the design method for small axial-flow fans, based on the airfoil theory. Journal Of Mechanical Engineering Science 225, 885–895.

Louw, F.G., 2011. Performance Trends of a Large Air-Cooled Steam Condenser during Windy Conditions. Stellenbosch University. Master's thesis. Department of Mechanical and Mechatronic Engineering. Stellenbosch University.

Masi, M., Lazzaretto, A., 2012. CFD models for the analysis of rotor-only industrial axial-flow fans, in: Proceedings of FAN 2012 Conference. France.

McGhee, R.J., Beasley, W.D., 1973. Low-speed aerodynic characteristics of a 17-percent-thick airfoil section designed for general aviation applciations, Security. Washington, D.C.

McGhee, R.J., Beasley, W.D., Somers, D.M., 1975. Low-speed aerodynamic characteristics of a 13-percent-thick airfoil section designed for general aviation applications. Nasa Technical Memorandum.

Menter, F.R., 1994. Zonal Two equation k-ε turbulence models for aerodynamic flows. AIAA 32, 1598–1605.

Meyer, C.J., Kröger, D.G., 2001. Numerical simulation of the flow field in the vicinity of an axial flow fan. International Journal for Numerical Methods in Fluids 36, 947–969.

Moin, P., Mahesh, K., 1998. DIRECT NUMERICAL SIMULATION: A Tool in Turbulence Research. Annual Review of Fluid Mechanics 30, 539–578.

Owen, M.T.F., Kröger, D.G., 2010. The effect of screens on air-cooled steam condenser performance under windy conditions. Applied Thermal Engineering 30, 2610–2615.

Pascu, M., Miclea, M., Epple, P., Delgado, A., Durst, F., 2009. Analytical and numerical investigation of the optimum pressure distribution along a low-pressure axial fan blade. Proceedings of the Institution of Mechanical Engineers, Part C: Journal of Mechanical Engineering Science 223, 643–657.

Pather, V., 2004. Eskom and Water, in: Proceedings of the 2004 Water Institute of Southern Africa (WISA) Biennial Conference. Cape Town, South Africa, pp. 659–664.

Pelz, P.F., Stonjek, S., Matyschok, B., Darmstadt, T.U., 2012. The influence of Reynolds number and roughness on the efficiency of axial and centrifugal fans – a physically based scaling method, in: Proceedings of FAN 2012 Conference.

Shankaran, G. V, Dogruoz, M.B., 2010. Validation of an advanced fan model with multiple reference frame approach, in: IEEE Intersociety Conference on Thermal and Thermomechanical Phenomena in Electronic Systems. Austin, United States.

Shih, T.-H., Liou, W.W., Shabbir, A., Yang, Z., Zhu, J., 1995. A New k-e Eddy Viscosity Model for High Reynolds Number Turbulent Flows - Model Development and Validation. Computer Fluids 24, 227–238.

Spalart, P.R., Allmaras, S.R., 1992. A one-equation turbulence model for aerodynamic flows, in: AIAA. p. Paper 92.

Stinnes, W H, Von Backstrom, T.W., 2002. Effect of cross-flow on the performance of air-cooled heat exchanger fans. Applied Thermal Engineering 22, 1403–1415.

Stinnes, Wolf Hubertus, 1998. The performance of axial fans subjected to forced cross-flow at inlet. Univesity of Stellenbosch. Master's thesis. Department of Mechanical and Mechatronic Engineering. Stellenbosch University

Thiart, G.D., Von Backström, T W, 1993. Numerical simulation of the flow field near an axial flow fan operating under distorted inflow conditions. Journal of Wind Engineering and Industrial Aerodynamics 45, 189–214.

Tu, J., Yeoh, G.H., Liu, C., 2008. Computational Fluid Dynamics - A Practical Approach. Elsevier, Retrieved from www.knovel.com.

Vad, J., Kwedikha, A.R.A., Horváth, C., Balczó, M., Lohász, M.M., Régert, T., 2007. Aerodynamic effects of forward blade skew in axial flow rotors of controlled vortex design., in: Proceedings of the Institution of Mechanical Engineers -- Part A -- Power & Energy. Professional Engineering Publishing, pp. 1011–1023.

Van der Spuy, S.J., 2011. Perimeter Fan Performance in Forced Draught Air-Cooled Steam Condensers. Stellenbosch University. Ph.D thesis. Department of Mechanical and Mechatronic Engineering. Stellenbosch University.

Van der Spuy, Sybrand J, Backström, Theodor W Von, Kröger, Detlev G, 2010. An Evaluation of Simplified Methods to Model the Performance of Axial Flow Fan Arrays. R & D Journal 26, 12–20.

Venter, S.J., 1990. The effectiveness of axial flow fans in A-frame plenums. Ph.D thesis. Department of Mechanical and Mechatronic Engineering. Stellenbosch University.

Versteeg, H.K., Malalasekera, W., 2007. An Introduction to Computational Fluid Dynamics: The Finite Volume Method, 2nd ed. Pearson, Harlow.

Zhao, W., Qu, Q., Li, Q., 2012. Numerical investigation on the flow field of an axial flow fan in a direct air-cooled condenser for a large power plant. Heat Transfer-Asian Research.

A Instrumentation

To test the three axial flow fans using the BS 848 test facility required certain modifications. In general the following changes and improvements were made to the facility:

- The drive shaft's pulley diameter was reduced from 315 mm to 250 mm which enabled the fan shaft to rotate at 900 rpm at lower electrical frequencies. The protective casing, housing three new belts, also had to be altered.
- The position of the shaft relative to the shroud had to be changed by tilting the entire mounting frame slightly forward.
- A new torque transducer was implemented which eventually resulted in the design of a new drive system.
- A newly designed drive system with new components was installed.
- The analog-to-digital measuring and processing unit was replaced.
- The pressure transducers were replaced due to increasing amounts of drift during operation.
- The power unit for the use of a variable speed control on the auxiliary fan was altered.

A.1 Improvements to the facility

Most of the improvements made to the test facility were as a result of the increasingly unreliable nature of the facility during initial tests. The next section explains the improvements made in more detail.

A.1.1 Recording equipment

Previous experiments carried out at the test facility used a HBM bridge amplifier to amplify the voltage signals. The signals were converted by a data acquisition module and connected via USB to a computer. All experimental data from the L1-fan was measured using the above mentioned equipment. However, due to the bridge amplifier becoming increasingly unreliable, new recording equipment and software was implemented. All further measurements from the L2- and N-fan were performed using the equipment described below.

A *HBM Spider8* data acquisition system with built-in bridge amplifier was used in conjunction with *CATMAN Easy* software. The *Spider8* connects to a computer via USB. A notebook computer (not specific) was used. This simplified the setup considerably and also resulted in faster set-up and set-down times. The *Spider8* uses DA-15 connection channels and therefore the signal cables' connectors had to be changed.

CATMAN Easy software is a measuring and data recording software program. It also allows the recording of multiple channels which can be defined individually according to its transducer type. The measuring frequency can be defined and filters can be added to the channels. The type of transducer is chosen according to each instruments' requirements and the output can be specified during the calibration of instrumentation. The settings used for each channel during testing are given in Table A.1.

Table A.1 - *Catman Easy* recording channel settings

Channel	Frequency/Filter	Transducer type	Output
Settling chamber	5Hz/Auto filter	Inductive halfbridge	Pa
Bellmouth	5Hz/Auto filter	Inductive halfbridge	Pa
Torque	5Hz/Auto filter	Inductive fullbridge (T2) DC Voltage 10V (T22)	Nm/V
Speed	5Hz/Auto filter	DC Voltage 10V	rpm

When a project is initialized, all readings are zeroed and real-time outputs for each channel are graphically represented. The real-time output became a convenient indicator of whether tests had reached a steady state condition for an operating point. Measurements were taken at a 5Hz frequency but data recording was controlled manually. This ensured that signal fluctuations between steady state operating points were not recorded and taken into account when measurements were averaged. At higher flow rates there were larger pressure fluctuations at the bellmouth as shown in the Figure A.1. This phenomenon was also evident in graphical output of the settling chamber pressure readings.

A certain degree of post-processing of the data was required because *CATMAN Easy* software has no averaging function built into the software. All data is recorded in real-time according to the frequency specified and stored as real-time data. A *Scilab* algorithm was written that averaged the measurements of each operating point for the complete set of data.

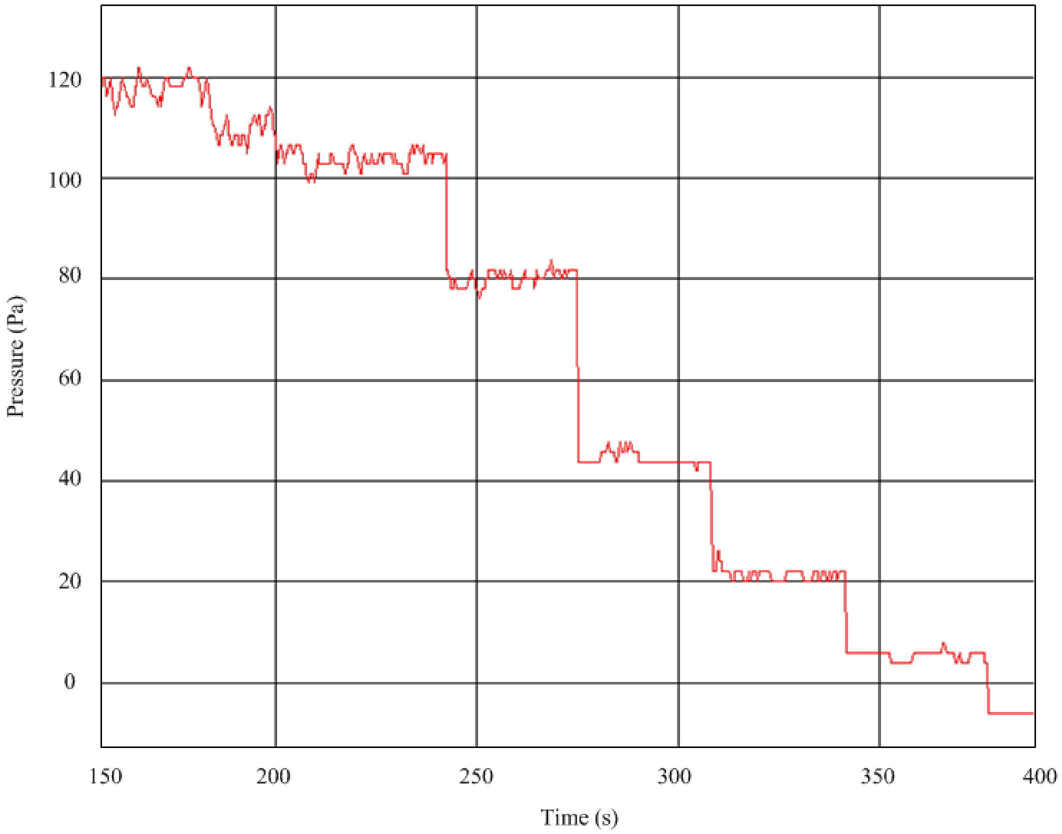

Figure A.1 - Real-time graph of the recorded inlet bellmouth pressure over time

A.1.2 Drive train

During the pre-test preparations large vibrations, originating from the drivetrain, were noticed. These vibrations intensified when the chains, fixed to the shroud of the test facility and steadying the driven side of the shaft, were loosened. Tightening the chains resulted in larger vibrations being transmitted to the settling chamber shroud. Inspection of the drivetrain revealed that the bearings supporting the two shafts had to be replaced. Large misalignment between the couplings was also identified as a source of vibration.

Figure A.2 illustrates the changes that had been made. As mentioned earlier, a new torque transducer was installed, which reduced the number for support bearings needed. A new drive shaft was designed and the positioning of the support bearings was changed. This improved the alignment between the two shafts. The HRC couplings were also replaced with much lighter bellow couplings which further reduced the excess weight of the drivetrain. However, these couplings were installed for the purposes of the L2- and N-fan tests and are only rated at 30 Nm. The simplified arrangement reduced the vibration transferred to the fan considerably and it was possible to test the fan at the desired speed in most cases.

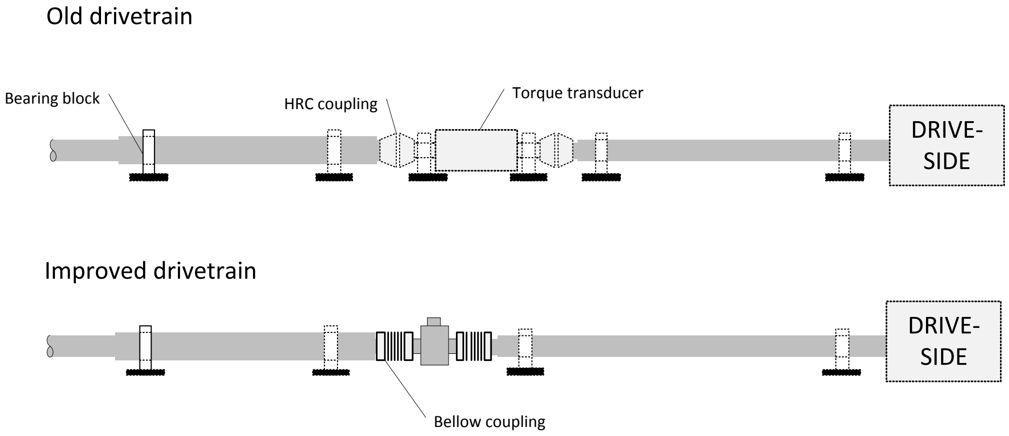

Figure A.2 - An illustration of the old and improved drivetrain of the test facility

A.2 Equipment

Generating fan characteristic curves for low flow rate axial fans proved to be challenging. This is largely due to the small changes in the pressure and torque measurements with a change in volume flow rate. Sensitive pressure transducers were necessary and thorough calibration was particularly critical considering that the tests would be used for numerical validation. Small changes in temperature and atmospheric pressure could also lead to differences between experimental and numerical results. Measuring the right parameter with properly calibrated equipment was therefore essential.

A.2.1 Pressure

To measure the static pressure inside the settling chamber and pressure drop across the bellmouth, two HBM PD1 inductive differential transducers with a range of ±1000 Pa were used. The transducers were kept in a fixed position inside the control room. Due to the large drift (~20 Pa) found during continuous testing, calibration of the pressure transducers were frequently redone to ensure accurate and repeatable measurements. Both transducers were open to the atmosphere at one end. Due to the position of the transducers long lengths of tube was used to transport the pressures and subsequently one could expect small fluctuations in the pressure to be dampened by the long lengths of tube. The pressure transducers were connected directly to the *Spider8* module.

A.2.2 Torque

The HBM T2 slip-ring torque transducer has been used for many years at the facility. Prior to the first tests the strain gauges of the transducer were replaced because of faulty operation. Due to the large size of the T2 torque transducer, which had a nominal rating much higher than required, and increased unreliability, a smaller torque transducer was installed. The T22 torque transducer with nominal rating of 100 Nm (see Figure A.3), being fairly new, used no-slip ring technology, which is different from the old torque transducer. The L2- and N-fan tests were carried out using the T22 torque transducer installed into the more simplified drivetrain which decreased frictional effects dramatically. The connection of the T22 to the *Spider8* module differed from the other measuring transducers. The T22's output signal was sent to a powered modulator which generated a voltage signal between 0 and 10. Zero indicated no torque was applied and the nominal rating of 100 Nm would be indicated by 10 V. The voltage output signal was connected to the *Spider8* module.

Figure A.3 - T22 torque transducer

A.2.3 Speed

The rotational speed of the fan was measured using an inductive proximity sensor positioned adjacent to the shaft. The output, a frequency signal that was generated by the proximity sensor, was converted into a 0 to 10 voltage reading through the use of a frequency-to-voltage modulator. The voltage output signal was connected to the *Spider8* module. The proximity sensor was found to be very sensitive to the distance between the sensor and the induction material. If this distance became too large the voltage reading was characterized by instability at a constant rotational speed.

A.2.4 Variable speed drives

To overcome the system resistance of the facility and measure the maximum flow rate the use of an auxiliary fan was needed. The BS 848 test facility was designed for larger fans such as the B-fan which operated at much higher flow rates than the N and L-fans. Consequently the auxiliary fan, being designed for much larger fans, proved to be too powerful for the requirements of this study. Therefore, in order to use the installed auxiliary fan, the rotational speed had to be controlled (and reduced) using a variable speed drive that also required alteration of the power module of the auxiliary fan. It was also found that the use of certain older variable speed drives introduced a disturbance onto the measuring signals. The problem could not be solved by changing the position of the variable speed drive with regards to the measuring equipment and other drives were used instead.

A.2.5 Other

To compensate for the change in temperature during continuous testing a thermometer was placed inside the settling chamber. This minimized the difference between the ambient temperature and the airflow temperature inside the settling chamber. The ambient pressure was measured by a mercury column barometer situated nearby. Data provided by the Engineering Faculty's local, small scale, weather station was also used to validate the pressure readings.

A.3 Experimental procedure

As stated earlier, the facility is situated outdoors and the effect of changing weather conditions had to be taken into account when tests were carried out. The slightest presence of wind at the bellmouth inlet affected the readings, especially at low flow rates.

A summary of the test procedure is as follows:

1. The atmospheric pressure and temperature at the location of the test facility was taken before each test of a blade-setting angle was conducted. Le Roux (2010) found that changes in the ambient temperature had an effect on the readings of the torque transducer. Therefore, before any readings were taken (including the zero readings), the fan was operated at maximum flow rate for a duration of 5-10 minutes. The temperature inside the plenum and the pressure outside was then measured and the torque reading was zeroed.

2. The pressure, torque and proximity sensor's readings were zeroed by the measuring software and a reading for the non-operational state was recorded.

3. The variable speed drive controlling the test fan was then increased to maximum rotational speed (900 RPM if possible) with the test tunnel throttle in the full open position. The auxiliary fan was started and its rotational speed was increased until the settling chamber pressure reading was just below zero Pascal. This indicated the maximum flow rate for the fan and the first measurements could now be taken.

4. The real-time output provided by CATMAN *Easy* enables the user to identify when the flow has reached a steady state. Once the real-time graph's reading reached a steady value at a specific throttle position, measurements were taken. Between 200 and 300 readings were taken at 5

Hz depending on how stable the measurements are (shown graphically). The volume flow rate, settling chamber pressure, shaft torque and shaft speed were measured for each flow rate change.

5. At a certain stage the function of the auxiliary fan is not required anymore and it can be switched off. It was found easiest to use the auxiliary fan's variable speed drive to control the flow rate further. Therefore, as the speed of the auxiliary fan was reduced, the flow rate was also reduced until it was completely switched off.

6. To ensure that the flow was fully blocked, a large obstruction was placed in front of the bellmouth to block the flow of air. Measurements were taken and the obstruction was again removed.

7. To test the repeatability of the data the process explained above was followed as the flow rate was increased again. The auxiliary fan, however, was not used for these purposes. Once the throttle was at the fully open position the test fan was switched off and zero readings were taken again to compensate for any drift in the system during the procedure.

8. The temperature inside the settling chamber was taken again and the average between the first and second reading was used for calculation purposes.

9. This process was repeated for every blade angle. For the various rotational speed tests, the process described above was followed similarly.

Sample calculations illustrating the processing of the measured values are shown in Appendix C. Figure A.4 is a schematic layout of the test facility and the equipment used during testing.

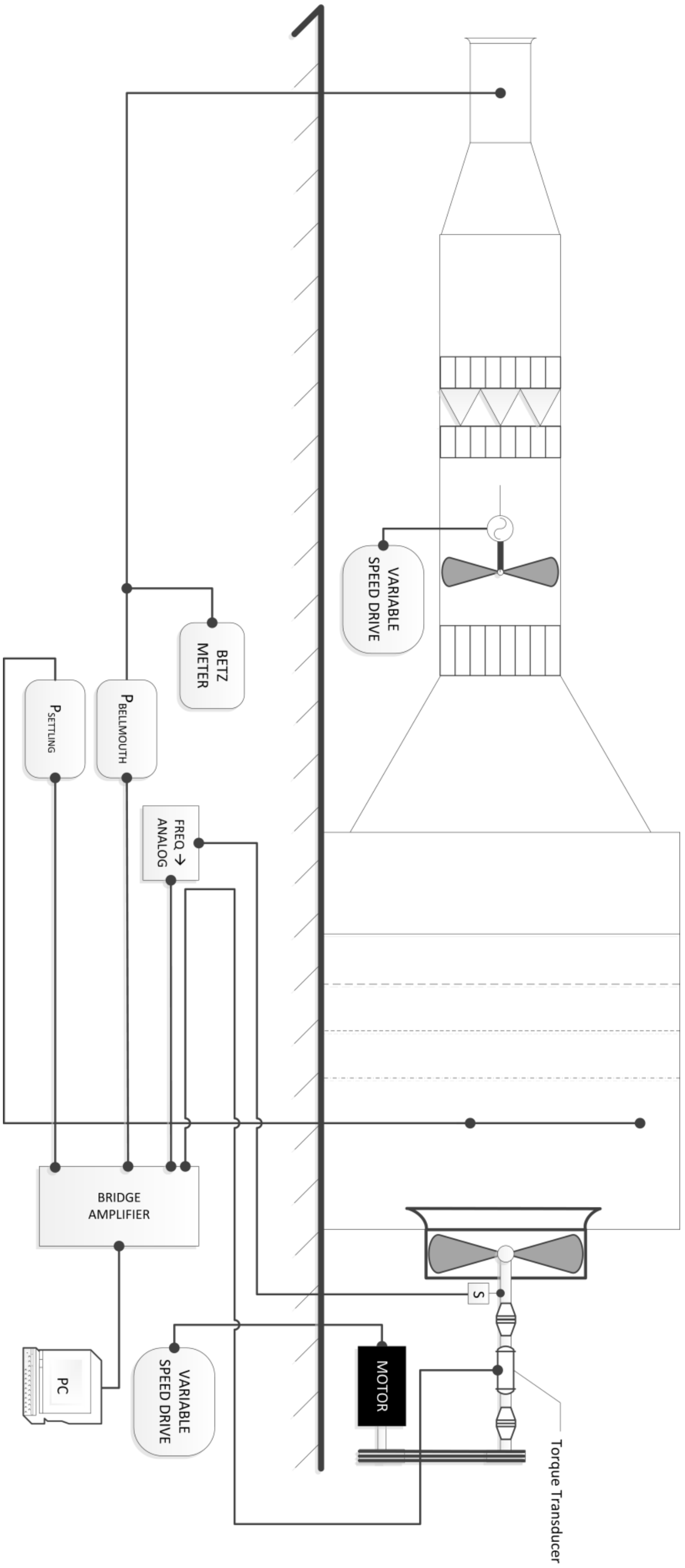

Figure A.4 - Schematic layout of the instrumentation of the test facility

A.4 Fan failure

During preparation for the final testing of the L1-fan, one of the blades failed at operational speed (±900 rpm). The facility was not damaged although the blade itself was damaged to an irreparable condition. No conclusive cause for failure can be given, but it is suspected that the shoulder of the blade at the hub (see Figure A.5) failed and due to the centrifugal force on the blade, was pulled outwards. The tip came into contact with the shroud and caused damage to the tip and root of the blade. The figure below shows the damage to the fan and blade. Adequate testing on the L1-fan was however conducted prior to the failure.

Figure A.5 - Fan blade failure

B Calibration

Although *CATMAN Easy* has preloaded sensor calibration data it was still necessary to calibrate all sensors used in the experimental setup. Calibration of the pressure and torque was done before each set of tests to ensure accuracy and repeatability.

B.1 Torque

Two torque transducers were used during testing. The calibration setup and procedure was the same for the T2 and T22 transducers. Due to the discontinued use of the T2 transducer, the calibration process which was followed will be described in terms of the T22 transducer. The details of the two torque transducers were already discussed in Appendix A.

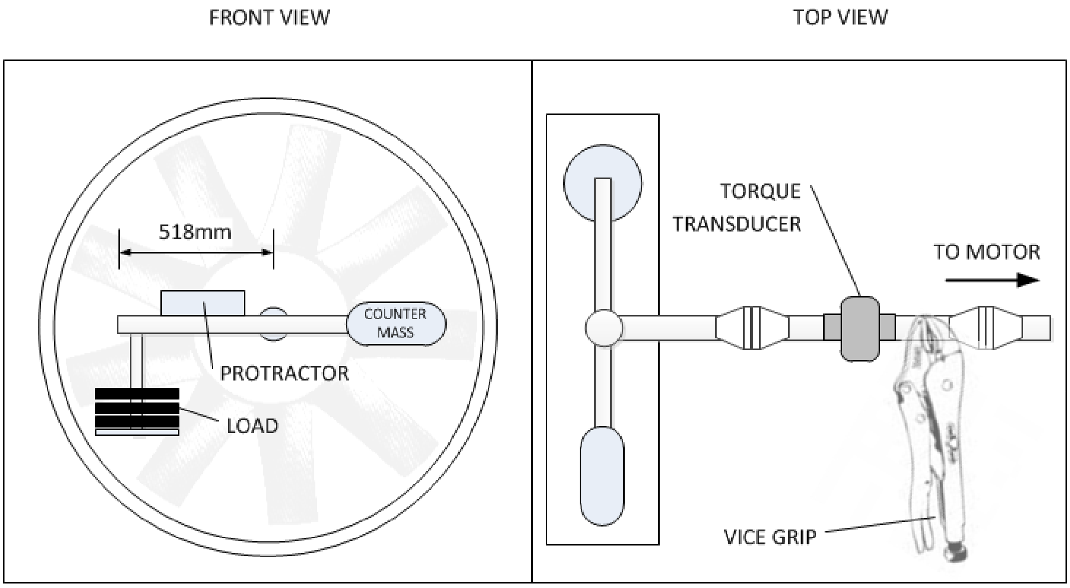

Figure B.1 - Setup for static torque calibration

To calibrate the torque transducer a static procedure as shown in Figure B.1 was carried out. The T22 transducer was connected to a 0 to 10 voltage amplifier and the output signal to the *Spider8* was therefore a DC voltage signal. To exert a rotational force on the shaft a cantilever arm was fixed to the front of the fan shaft with the fan removed. The torque was transmitted to the transducer by the bellow coupling mentioned in Appendix A. The shaft on the motor side of the torque transducer was locked (see “top view” of Figure B.1) using a vice grip. Mass was added to the cantilever beam in 1kg (5 Nm) increments (see “front view” of Figure B.1) and the corresponding voltage readings were taken. Before any measurements were taken the cantilever beam was positioned horizontally using a digital protractor. The measurements of the tested fans were expected to be between 20 and 30 Nm. The calibration data for the torque is given in Table B.1 and the calibration trend line is given in Figure B.2.

Table B.1 - Calibration values for the T22 torque transducer

Reading	Mass (kg)	Torque (Nm)	Voltage (V)
1	**0**	**0**	**0.0532**
2	**0.999**	**5.037298**	**0.2992**
3	**2.015**	**10.16032**	**0.5496**
4	**3.014**	**15.19761**	**0.8008**
5	**4.022**	**20.28029**	**1.0564**
6	**5.01**	**25.26212**	**1.3048**

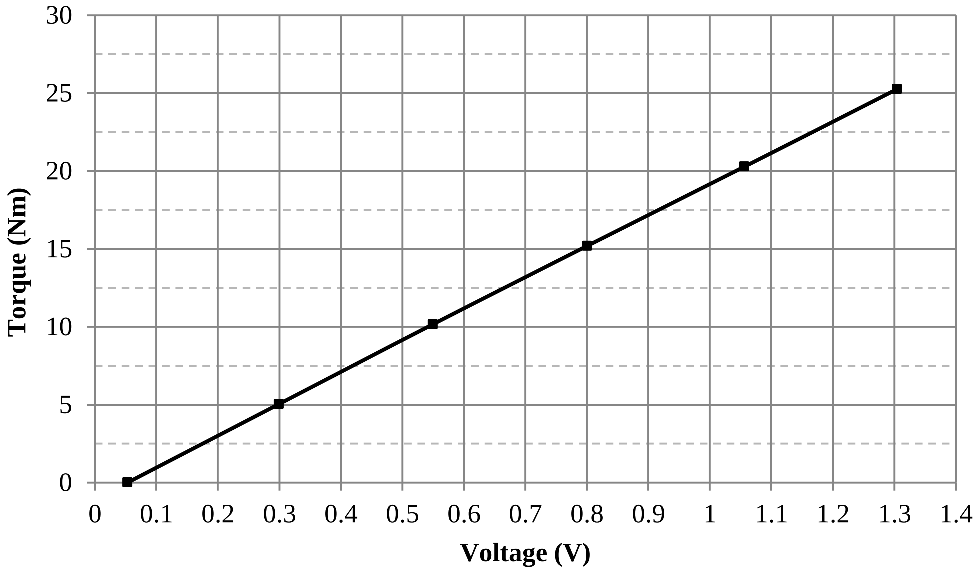

Figure B.2 - Trend line for the torque calibration values

To compensate for losses due to the dynamic operation of the drive system the blades were removed from the hub. The torque for a hub-only configuration was consequently measured at the design speed (900rpm). Although the measured torque was less than 2% of the maximum fan torque values it was subtracted from the calculated fan torque at design speed.

Consider Figure B.3 which shows data from the torque transducer for approximately 30 seconds. It indicates a fair amount of fluctuation during normal operation which can be attributed to various factors: A slightly bent drive shaft, misalignment between connecting shafts and a slightly unbalanced fan. To determine the torque an average of the measurements, taken for a specific operating point, was calculated.

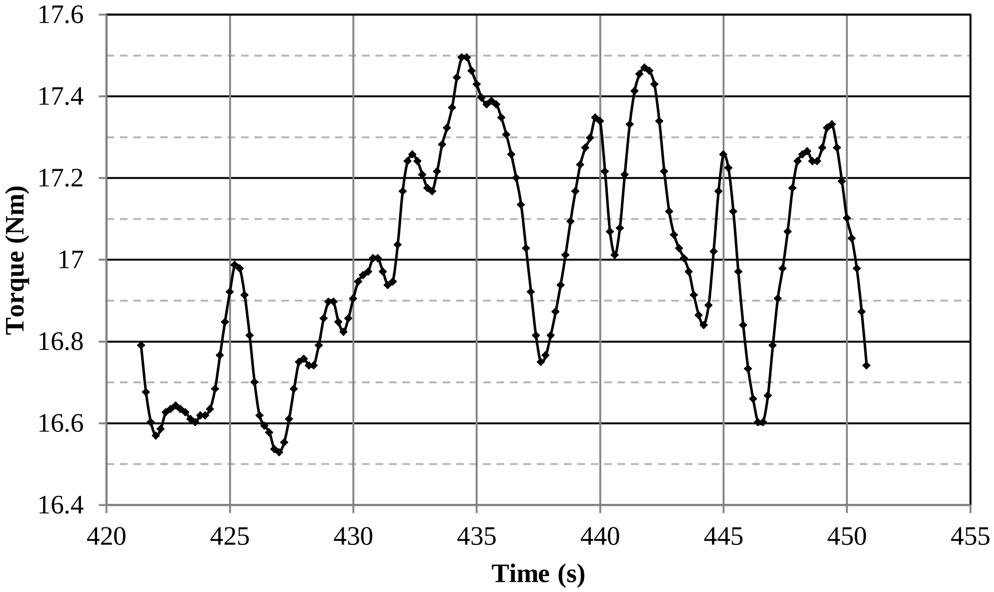

Figure B.3 - Torque fluctuations for 30 seconds

B.2 Pressure

The pressure transducers were situated inside the test room and calibration was also carried out there. All pressure calibrations were conducted using the Betz manometer. The piping connections were configured in such a way that no disconnection after calibration would result in movement of the pressure transducers. The pressure transducers were open to the atmosphere at one end and connected to the Betz manometer on the other end. Due to the fact that the pressure differences in the bellmouth were much smaller than in the settling chamber, calibration was carried out separately.

Figure B.4 shows the entire configuration which was used to calibrate the pressure transducers. The pressure transducers were calibrated using the corresponding pressure value from the Betz manometer as guideline. Time had to be given for the water level to stabilize before measurements were taken.

Regular calibration of the pressure transducers between blade-setting angle changes was also necessary due to the drift of the transducers. The drift significantly affected the measured results, especially in the case of the bellmouth measurements which had small pressure changes. To identify drift during testing, the Betz manometer was used to monitor the difference between the reading given by the software (affected by drift) and the manometer reading.

Although the pressure transducers were the same, their calibration curves were notably different as shown by Figure B.5 and Figure B.6. The calibration data for the pressure transducers are also given below in Table B.2 and Table B.3

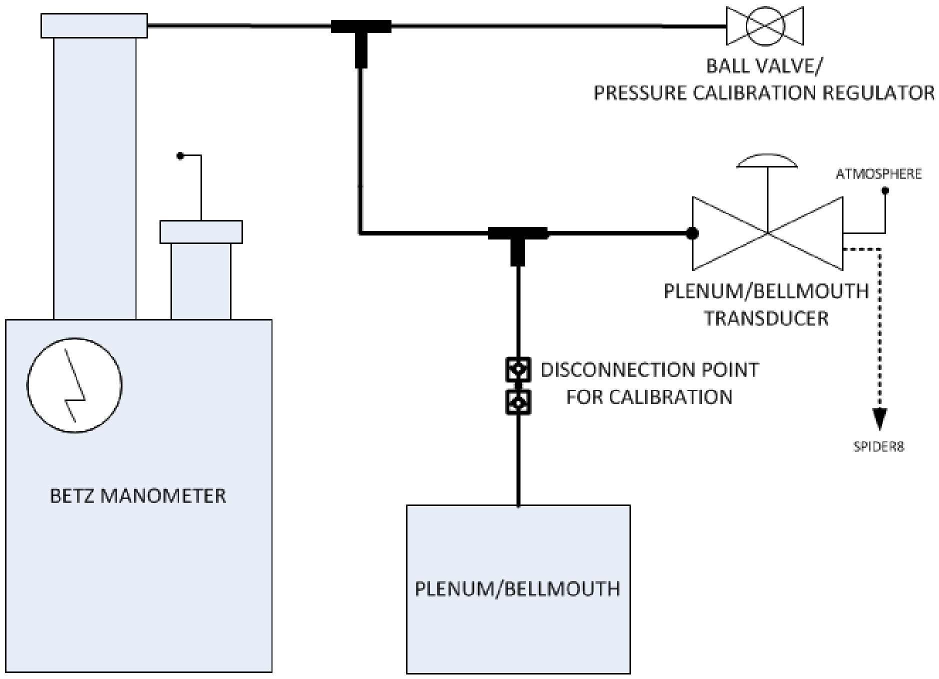

Figure B.4 - Configuration for calibrating the pressure transducers

Table B.2 - Settling chamber pressure calibration values

Voltage (V)	Betz (mmH_2O)	Pressure (Pa)
-3.265	**0**	**0**
-3.01	**10**	**98.0655**
-2.76	**20**	**196.131**
-2.505	**30**	**294.1965**
-2.255	**40**	**392.262**
-2	**50**	**490.3275**

Table B.3 - Inlet bellmouth pressure calibration values

Voltage (V)	Betz (mmH_2O)	Pressure (Pa)
0.775	**0**	**0**
0.87	**4**	**39.2262**
0.965	**8**	**78.4524**
1.06	**12**	**117.6786**
1.155	**16**	**156.9048**
1.25	**20**	**196.131**

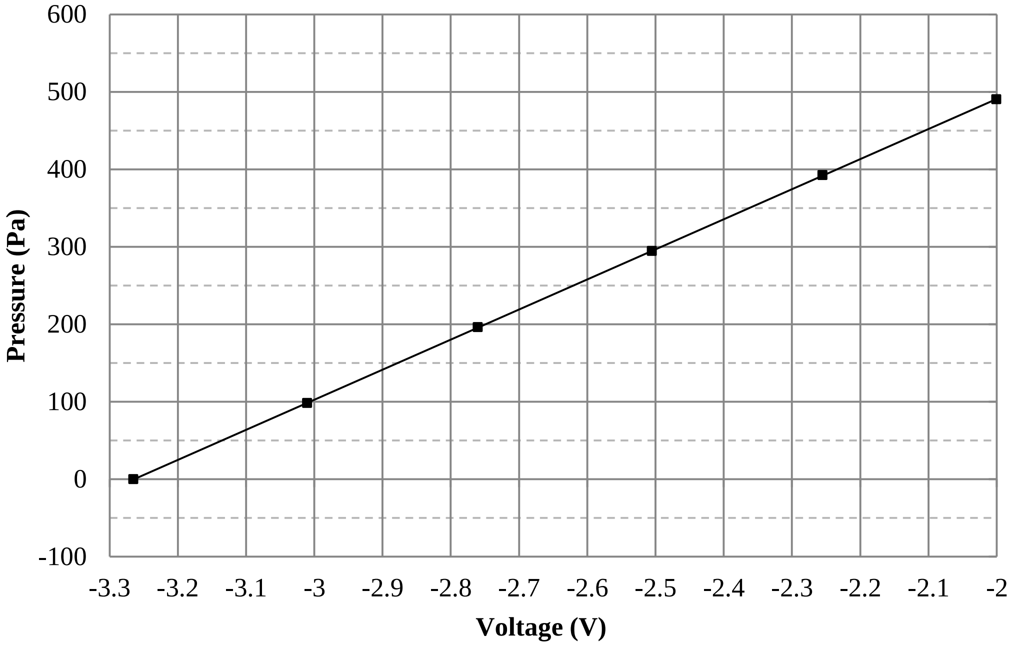

Figure B.5 - Settling chamber trend line for calibration values

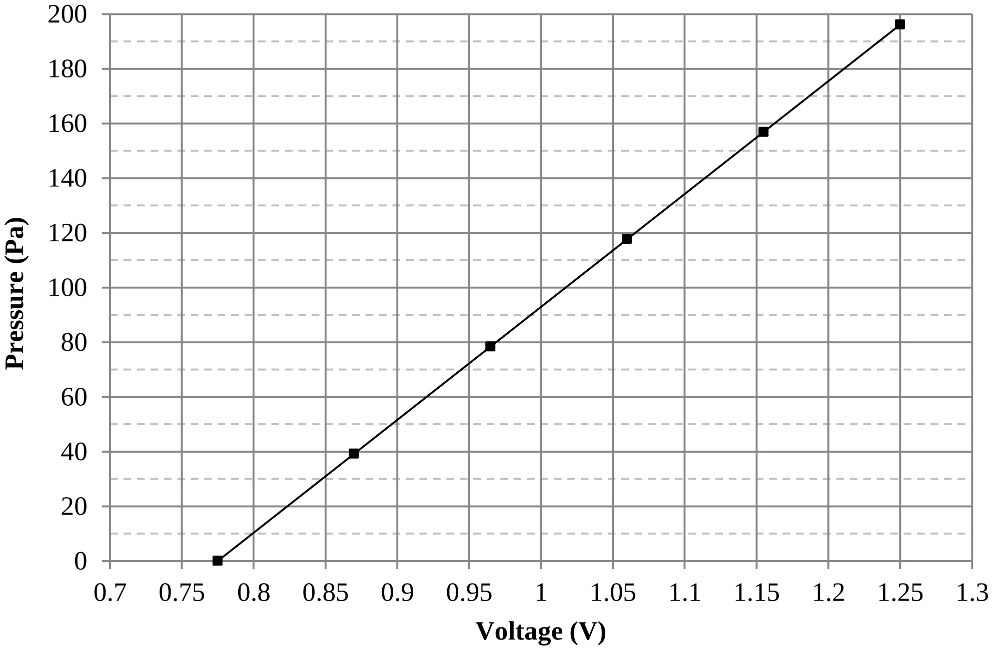

Figure B.6 - Inlet bellmouth trend line for calibration values

B.3 Speed

The rotational speed of the shaft was calibrated using a handheld tachometer. The fan was removed from the shaft and the motor frequency was increased in 10 Hz increments. For each frequency the tachometer measured the rotational speed in rpm and the corresponding voltage reading was taken (see Table B.4 and Figure B.7).

Table B.4 - Proximity sensor calibration values

Motor frequency (Hz)	Voltage (V)	Tachometer (rpm)
0	**0**	**0**
10	**2.2204**	**193**
20	**4.4504**	**386**
30	**6.6796**	**578**
40	**8.9056**	**772**

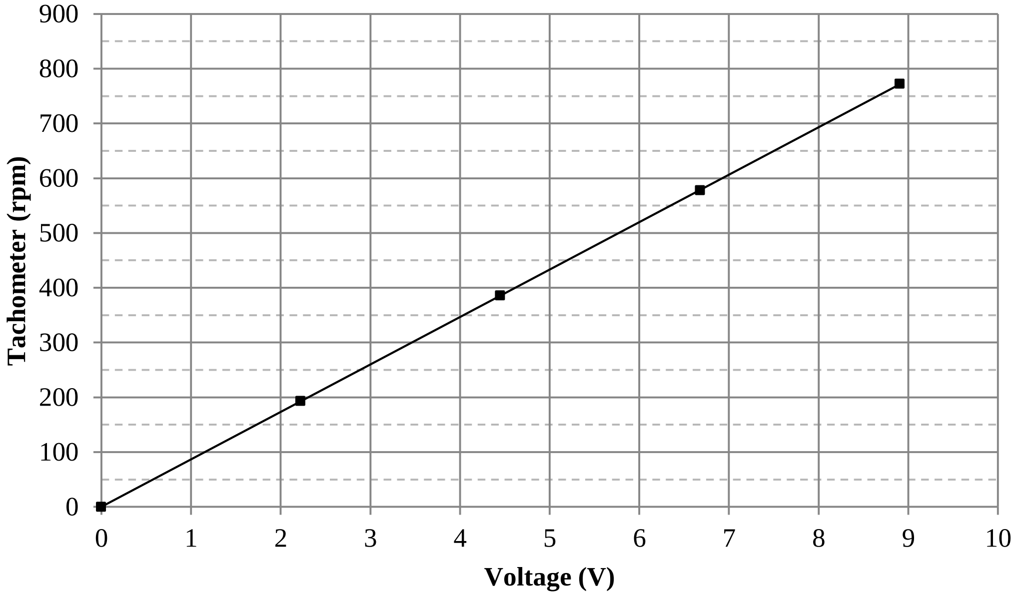

Figure B.7 - Proximity sensor trend line of calibration values

C Sample Calculations

Calculations were performed in accordance with the BS 848 (1997) guidelines. Due to the fact that the calibration calculations are carried out in *CATMAN Easy*, there was no need for calibration equations. The values measured and the data exported was already calibrated and the sample calculations will use these values. The effect of drift is taken into consideration before the fan static pressure, fan shaft power and fan static efficiency is calculated.

For the sample calculations below, the following measurements taken during the testing of the L2-fan will be used.

Table C.1 - Sample calculation properties

Axial flow fan	L2
Blade-setting angle	6.9°
Atmospheric pressure	1014.9 hPa
Temperature (pre-test reading)	23 °C
Temperature (post-test reading)	23 °C

Table C.2 - Values used for sample calculations

	Settling chamber (mmH_2O)	**Bellmouth (mmH_2O)**	**Torque (Nm)**	**Rotational speed (rpm)**
Zero (pre-test)	0	0	-0.0496	-0.0348
Data (7th measurement)	14.8165	7.6028	27.7456	853.1933
Zero (post-test)	-0.1961	0.0285	-0.0329	0.0382

To calculate the settling chamber and bellmouth pressures in Pascal the following conversion from mmH_2O to Pascal is done:

$$\Delta P_{bell} = 14.8165\, mmH_2O \times 9.80655$$

$$= 145.3\, Pa$$

$$\Delta P_{sett} = 7.6028\, mmH_2O \times 9.80655$$

$$= 74.56\, Pa$$

The torque and rotational measurements were given in Nm and rpm respectively and requires no change. To compensate for the drift, the following equation was used:

$$drift = data(n_0) + (n_{i-1}/(n_n - 1)) \times (data(n_n) - data(n_0)) \quad \textbf{(C.1)}$$

Equation C.1 assumes a linear drift between the initial zero value, taken before a test started, and the nth value taken after the test was finished. The initial deviation (if not zero) is also subtracted from the measurement. The drift for the sample measurements is therefore:

$$\Delta P_{sett\_drift} = \Delta P_{sett} - (P_{sett_0} + (n_{i-1}/(n_n - 1)) \times \Delta P_{sett_0})$$

$$= 145.3 - (0 + (6/(12 - 1) \times (-1.923)$$

$$= 146.35\ Pa$$

$$\Delta P_{bell\_drift} = \Delta P_{bell} - (P_{bell_0} + (n_{i-1}/(n_n - 1)) \times \Delta P_{bell_0})$$

$$= 74.56 - (0 + (6/(12 - 1) \times (0.279))$$

$$= 74.405\ Pa$$

$$T_{drift} = T - (T_0 + (n_{i-1}/(n_n - 1)) \times \Delta T_0)$$

$$= 27.75 - (-0.05 + (6/(12 - 1) \times (-0.033))$$

$$= 27.786\ Nm$$

$$N_{drift} = N - (N_0 + (n_{i-1}/(n_n - 1)) \times \Delta N_0)$$

$$= 853.193 - (-0.035 + (6/(12 - 1) \times (0.038))$$

$$= 853.188\ rpm$$

The measured ambient pressure as given in Table C.1 was,

$$p_{amb} = 1014.9\ hPa$$

The operating temperature in Kelvin for a test was determined by calculating the average between the pre- and post-temperature of a test.

$$T_{amb} = \frac{T_1 + T_2}{2} + 273.15 \quad \textbf{(C.2)}$$

$$= \frac{23 + 23}{2} + 273.15$$

$$= \; 296.15\, K$$

The ambient density can then be calculated using the ideal gas law,

$$\rho_{amb} = \frac{p_{amb}}{R\, T_{amb}} \tag{C.3}$$

$$= \frac{101490}{287.08\; 296.15}$$

$$= \; 1.194\; kg/m^3$$

The pressure drop over the bellmouth can be used to calculate the mass flow rate using Bernoulli obstruction theory which simplifies to the following equation,

$$\dot{m} = \alpha\varepsilon \frac{\pi\, {D_{bell}}^2}{4} \sqrt{2\, \rho_{amb}\, \Delta p_{bell\_drift}} \tag{C.4}$$

where,

$$D_{bell} = 1.008\, m$$

and the compound calibration constant value obtained from Venter (1990) is given as,

$$\alpha\varepsilon = 0.9802$$

The mass flow rate is then calculated as,

$$\dot{m} = 0.9802\; \frac{\pi\; 1.008^2}{4} \sqrt{2\; (1.194)\; (74.405)}$$

$$= \; 10.427\; kg/s$$

The air density inside the settling chamber is adjusted relative to the atmospheric pressure as follows:

$$\rho_{sett} = \rho_{amb} \frac{p_{amb} - \Delta p_{sett\_drift}}{p_{amb}} \tag{C.5}$$

$$= 1.194 \frac{101490 - 146.35}{101490}$$

$$= \; 1.192\; kg/m^3$$

Having calculated the mass flow rate and settling chamber density, the average dynamic pressure and volume flow rate inside the settling chamber can be determined.

The volume flow rate is calculated by,

$$Q = \frac{\dot{m}}{\rho_{sett}} \tag{C.6}$$

$$= \frac{10.427}{1.192}$$

$$= 8.75\ m^3/s$$

The dynamic pressure inside the settling chamber is manipulated by the following equation,

$$p_{dsett} = \frac{1}{2}\rho_{sett}\, {V_{sett}}^2 \tag{C.7}$$

$$= \frac{1}{2}\rho_{sett}\left(\frac{\dot{m}}{\rho_{sett}\, A_{sett}}\right)^2$$

$$= \frac{1}{2\ \rho_{sett}}\left(\frac{\dot{m}}{A_{sett}}\right)^2$$

where the area of the settling chamber is,

$$A_{sett} = 16\ m^2$$

and the dynamic pressure inside the settling chamber is then calculated as follows,

$$= \frac{1}{2\ (1.192)}\left(\frac{10.427}{16}\right)^2$$

$$= 0.178\ Pa$$

The fan static pressure rise is defined by BS 848 (1997) as the difference between the outlet static pressure and the inlet total pressure. Since the outlet static pressure is atmospheric, the fan static pressure can be calculated as follows:

$$p_{FS} = p_{amb} - (p_{static\ sett} - p_{dsett}) \tag{C.8}$$

$$= \Delta p_{sett\_drift} - p_{dsett}$$

$$= 146.35 - 0.178$$

$$= 146.17\ Pa$$

In Appendix B it was mentioned that a no-load measurement of the torque was taken at 900 rpm. The no-load torque was measured as,

$$T_{no\_load} = 0.473\ Nm$$

Therefore the no-load fan power can be calculated subtracting the no-load torque from the measured torque.

$$T = T_{shaft\_drift} - T_{no\_load} \tag{C.9}$$

$$= 27.786 - 0.473$$

$$= 27.313\ Nm$$

The fan power is calculated as follows,

$$P = \frac{2\,\pi\, N_{shaft\_drift}\, T}{60} \tag{C.10}$$

$$= \frac{2\,\pi\,(853.188)\,(27.313)}{60}$$

$$= 2440.3\ W$$

which is 40 W less than when the no-load torque would be neglected. The calculated data is referenced to a standard air density of 1.2 kg/m^3 and rotational speed of 900 rpm, using the fan scaling laws. The fan scaling laws are defined as:

$$\left(\frac{Q}{ND^3}\right)_1 = \left(\frac{Q}{ND^3}\right)_2 \tag{C.11}$$

$$\left(\frac{p}{\rho N^2 D^2}\right)_1 = \left(\frac{p}{\rho N^2 D^2}\right)_2 \tag{C.12}$$

$$\left(\frac{P}{\rho N^3 D^5}\right)_1 = \left(\frac{P}{\rho N^3 D^5}\right)_2 \tag{C.13}$$

Due to the diameter being the same for both cases, these laws simplify to the following equations and the fan pressure, volume flow rate and power are calculated as follows,

$$Q' = Q\left(\frac{N'}{N}\right) \tag{C.14}$$

$$= 8.75\left(\frac{900}{853.188}\right)$$

$$= 9.23\ m^3/s$$

$$p'_{FS} = p_{FS}\left(\frac{N'}{N}\right)^2\left(\frac{\rho'}{\rho_{sett}}\right) \tag{C.15}$$

$$= 146.17\left(\frac{900}{853.188}\right)^2\left(\frac{1.2}{1.192}\right)$$

$$= 163.7\ Pa$$

$$P' = P_{no\_load}\left(\frac{N'}{N}\right)^3\left(\frac{\rho'}{\rho_{sett}}\right) \tag{C.16}$$

$$= 2440.3\left(\frac{900}{853.188}\right)^3\left(\frac{1.2}{1.192}\right)$$

$$= 2883.6\ W$$

Finally the fan static efficiency is calculated as,

$$\eta_{FS} = \frac{p'_{ps}\ Q'}{P'} \tag{C.17}$$

$$= \frac{163.74\ (9.23)}{2883.6} \times 100$$

$$= 52.4\%$$

D Numerical fan models

The procedure for creating the solid models of the various fans was briefly explained in Chapter 3. This section will discuss the details behind the creation of solid models of the different fans. It also includes an analysis of the scanned fans using software algorithms.

D.1 B-fan: specifications

The original B2-fan, designed by Bruneau (1994), used the GA(W)-2 aerofoil. The GA(W)-2 aerofoil is a 13% thick version of the 17% thick GA(W)-1 aerofoil. The original GA(W)-1 aerofoil data points, as taken from McGhee & Beasley (1973) are given in Table D.1.

Table D.1 - B-fan blade profile data

Data by McGhee et al (1973)			Calculated parameters	
x/c	**(z/c)upper**	**(z/c)lower**	**Camber line (z_c)**	**Thickness (17%) (z_t)**
0	0	0	0	0
0.002	0.013	-0.00974	0.00163	0.01137
0.005	0.02035	-0.01444	0.002955	0.017395
0.0125	0.03069	-0.02052	0.005085	0.025605
0.025	0.04165	-0.02691	0.00737	0.03428
0.0375	0.04974	-0.03191	0.008915	0.040825
0.05	0.056	-0.03569	0.010155	0.045845
0.075	0.06561	-0.04209	0.01176	0.05385
0.1	0.07309	-0.047	0.013045	0.060045
0.125	0.07909	-0.05087	0.01411	0.06498
0.15	0.08413	-0.05426	0.014935	0.069195
0.175	0.08848	-0.057	0.01574	0.07274
0.2	0.09209	-0.05926	0.016415	0.075675
0.25	0.09778	-0.06265	0.017565	0.080215
0.3	0.10169	-0.06448	0.018605	0.083085
0.35	0.10409	-0.06517	0.01946	0.08463
0.4	0.105	-0.06483	0.020085	0.084915
0.45	0.10456	-0.06344	0.02056	0.084
0.5	0.10269	-0.06091	0.02089	0.0818
0.55	0.09917	-0.05683	0.02117	0.078
0.575	0.09674	-0.05396	0.02139	0.07535
0.6	0.09374	-0.05061	0.021565	0.072175
0.625	0.09013	-0.04678	0.021675	0.068455
0.65	0.08604	-0.04265	0.021695	0.064345
0.675	0.08144	-0.0383	0.02157	0.05987
0.7	0.07639	-0.03383	0.02128	0.05511

0.725	0.07096	-0.0293	0.02083	0.05013
0.75	0.06517	-0.02461	0.02028	0.04489
0.775	0.05913	-0.0203	0.019415	0.039715
0.8	0.05291	-0.01587	0.01852	0.03439
0.825	0.04644	-0.01191	0.017265	0.029175
0.85	0.03983	-0.00852	0.015655	0.024175
0.875	0.03313	-0.00565	0.01374	0.01939
0.9	0.02639	-0.00352	0.011435	0.014955
0.925	0.01965	-0.00248	0.008585	0.011065
0.95	0.01287	-0.00257	0.00515	0.00772
0.975	0.00604	-0.00396	0.00104	0.005
1	-0.00074	-0.00783	-0.004285	0.003545

Figure D.1 illustrates the small difference between the GA(W)-2 data, which had a thickness distribution of 13% given by McGhee et al. (1975), and the GA(W)-1 with a calculated thickness distribution of 13% using the approximate equation for the camber line in Chapter 3. It clearly shows the validity of Equation 3.6 by the small deviations found between data points. The data found in Table D.1 was consequently used to determine the blade profile coordinates for a linear decrease of 13 to 9%.

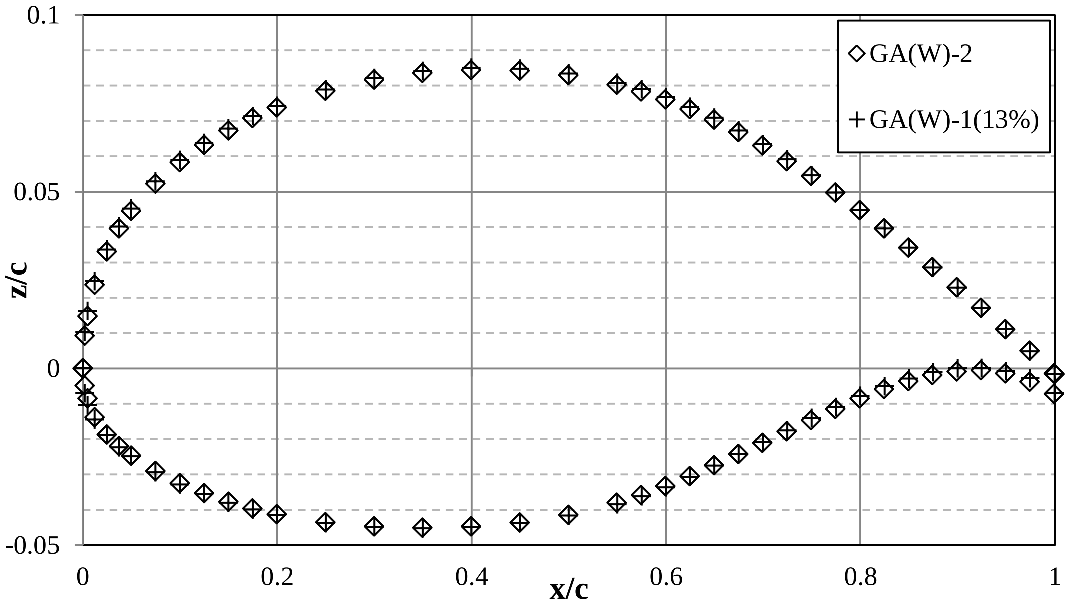

Figure D.1 - Comparison between the GA (W)-1 and GA (W)-2 aerofoils

For the purposes of this study, five blade profiles at equally spaced radial stations along the blade were calculated. The angle for each profile was determined by calculating the stagger angle for a specified radius. Fitting a trendline through the data, shown by Figure D.2, the stagger angle for any radius could be calculated. A rotation matrix was used to rotate the data points by the calculated stagger angle.

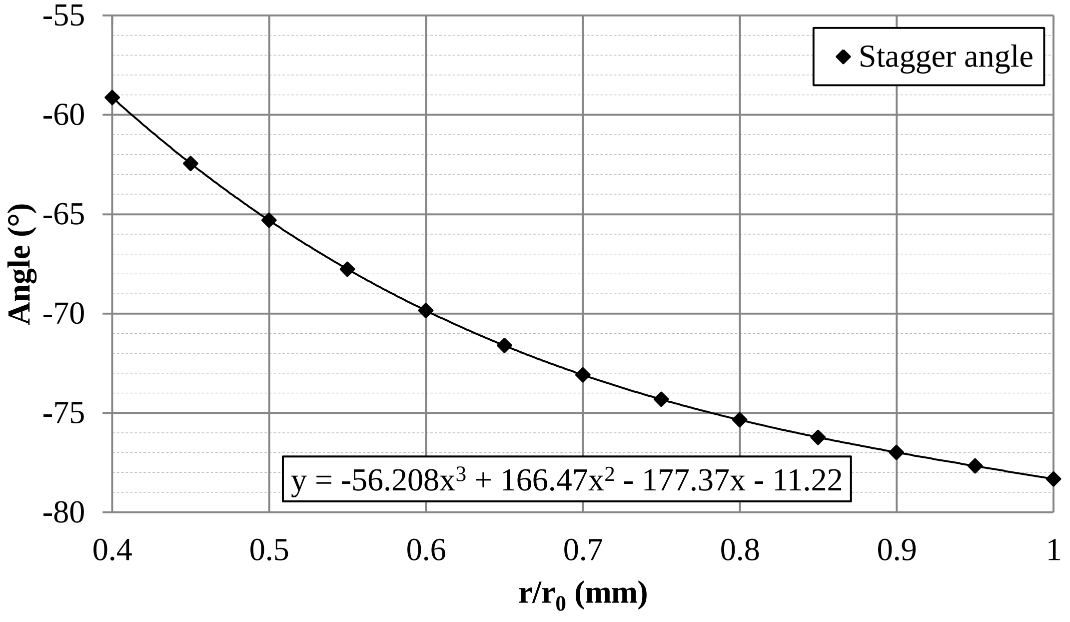

Figure D.2 - Stagger angle trendline for the B-fan (Stinnes, 1998)

The chord line lengths, varying linearly from the hub to the tip, were taken from Meyer and Kröger (2001) and are given in Table D.2 together with other important specifications. The specifications of the B-fan are as follows:

Table D.2 - General specifications of the B-fan

D_o	1.536 m
D_i	0.6168 m
Tip clearance	3 mm
Chord r/r_0 = 0.4	184 mm
Chord r/r_0 = 1	153 mm
Speed	750 rpm

D.2 N and L-fans: specifications

Because the N and L-fans were manufactured models there were no design details available. It was mentioned in Chapter 3 that initially an average representative blade was calculated for simulation purposes. The calculated blade, proved to be a poor representation of the real average due to specific factors. The following section explains the methods implemented to try and find the parameters that characterize these fans and also discuss the factors that resulted in the average blade not being used. Table D.3 gives the available data as specified by the supplier of the N and L-fans. The data for all the scaled fans are similar.

Table D.3 - General specifications for the N and L-fans

D_o	1.24 m
D_i	0.169 m
Tip clearance	5 mm
Speed	900 rpm

D.3 N and L-fans: analysis

The initial idea of calculating a representative blade included: normalizing each blade profile of a specified radius for an entire fan, averaging the combined normalized data (of all the blade profiles and repeating for various radii. The process of calculating an average fan blade and its characteristic parameters such as the chord line length, stagger angle, camber line and thickness distribution is divided into four sections for explanation purposes. The process is illustrated in Figure D.3.

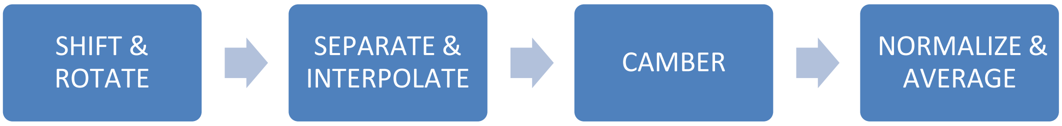

Figure D.3 - The four steps used to create the average representative blade.

1. *Shift & Rotate*

The original data of each scanned fan blade was positioned differently relative to a fixed Cartesian coordinate system. For averaging to be possible the data for each blade had to be shifted and rotated to a similar reference point. The origin (0,0,0) was used for this purpose. Due to the fact that the rotation, chord length and relative position varied between each profile (although care was taken during scanning) it was necessary to calculate these parameters for each blade profile in order to determine the positional change required.

Figure D.4 (a) shows the original difference in relative position between the tip profiles (r = 605mm) of the L2-fan’s eight blades. To rotate each profile to the same relative position the chord line was calculated and the angle of the chord line was determined. The calculated chord lines for five radial blade profiles of a single fan blade are shown in Figure D.4 (b). Having determined these parameters, they are used to shift and rotate each profile to the origin as shown in Figure D.4 (c).

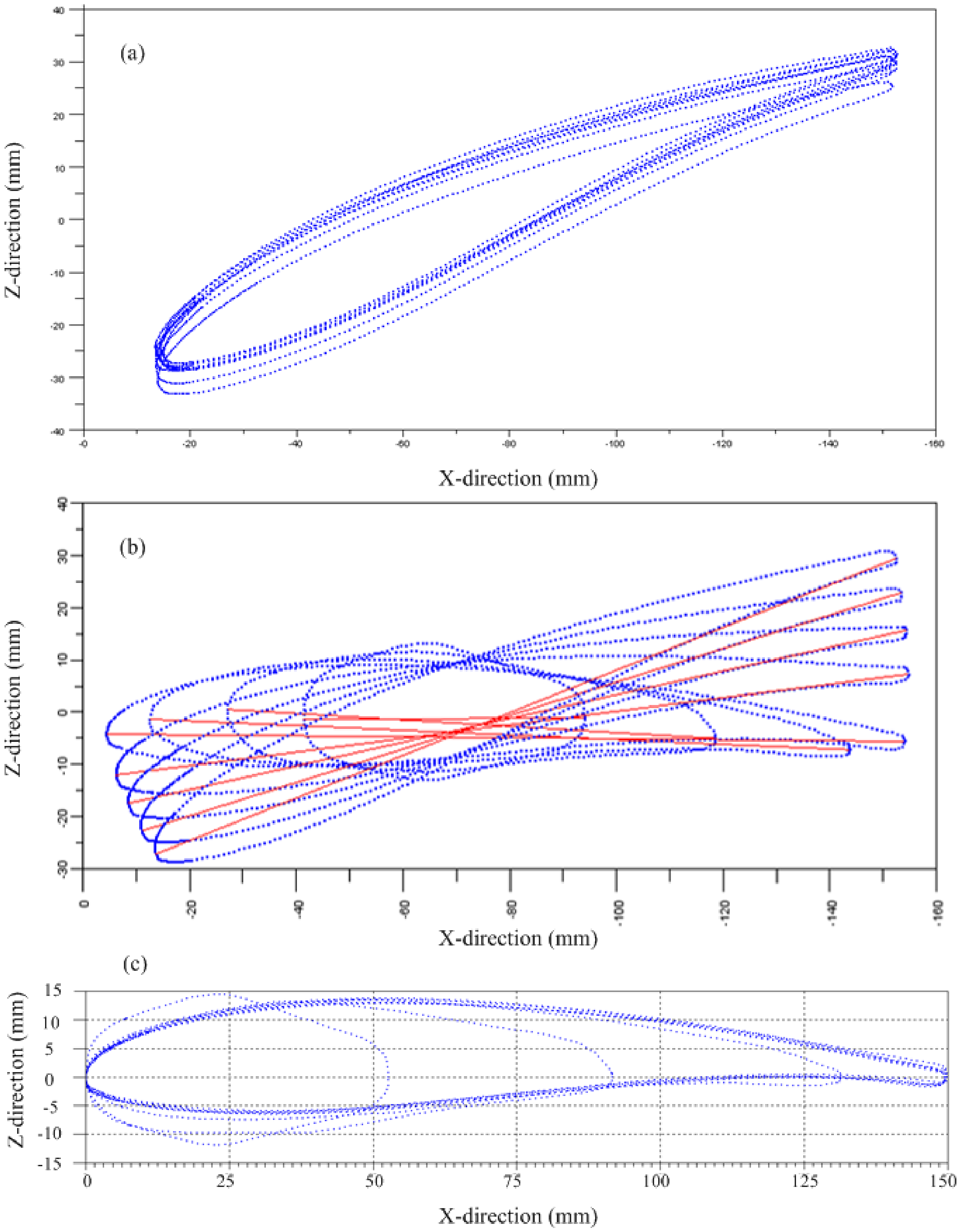

Figure D.4 - (a) Original position of tip profiles for the different blades of a fan; (b) Relative position and chord lines calculated for blade profiles of a particular fan; (c) Blade profiles in (b) shifted and rotated

It was mentioned in Chapter 3 that the L1 and L2 fans are similar axial fans, supposedly having the same profile characteristics and chord lengths. From simple observations it was recognised that the thickness distribution differed slightly and the experimental test results confirmed this. Using the parameters calculated for the shift and rotate procedure further comparisons could be made.

Figure D.5 compares the differences between the chord line lengths at specific radii for the eight blades of the L1- and L2-fan. It clearly shows that the L2-fan has a narrower chord length range for each radius than the L1-fan. It would also appear that there is no definitive change in the chord length with increasing radius which differs from the design of the B-fan.

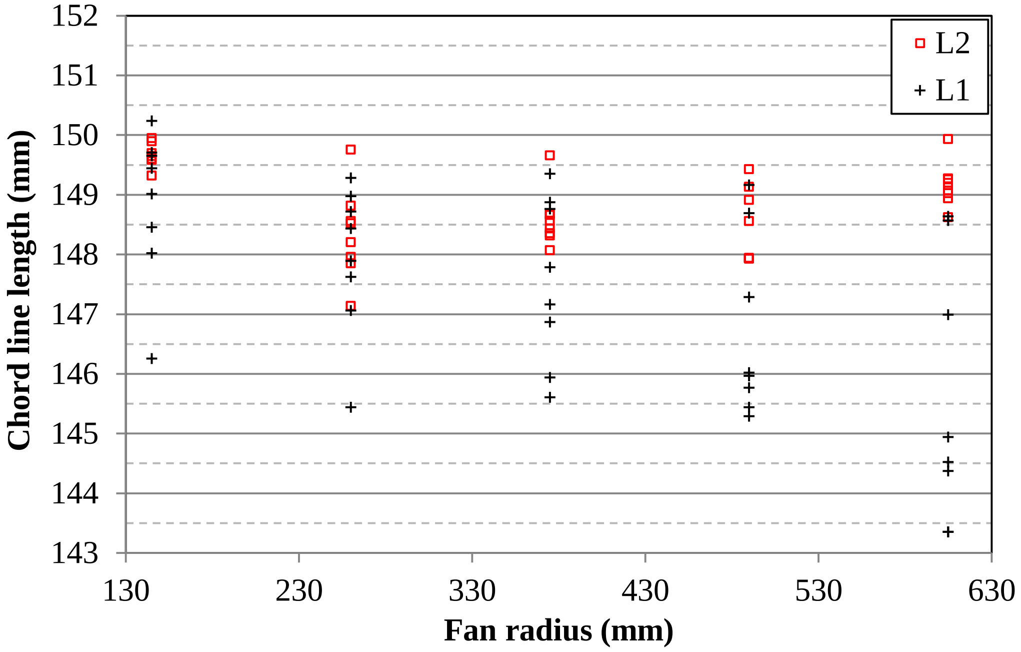

Figure D.5 - Comparison between the L1- and L2-fan's chord length distribution for 145, 265, 375, 490, 605 mm radial position

The gradient of each chord line was used as a measure of the relative twist found in each fan blade profile. Figure D.6 shows the small variation in angles for specific radii. It must be emphasized that the angles shown in Figure D.6 are only a relative comparison and must not be regarded as the actual stagger angles of the L-fans. The second degree polynomials, fitted to the data of the L1 and L2-fans, indicate the trend for each data set. It shows a close correlation between the blade angles of both axial. However, the difference in the performance of the two fans may be partially attributed to the small angle differences in the tip region.

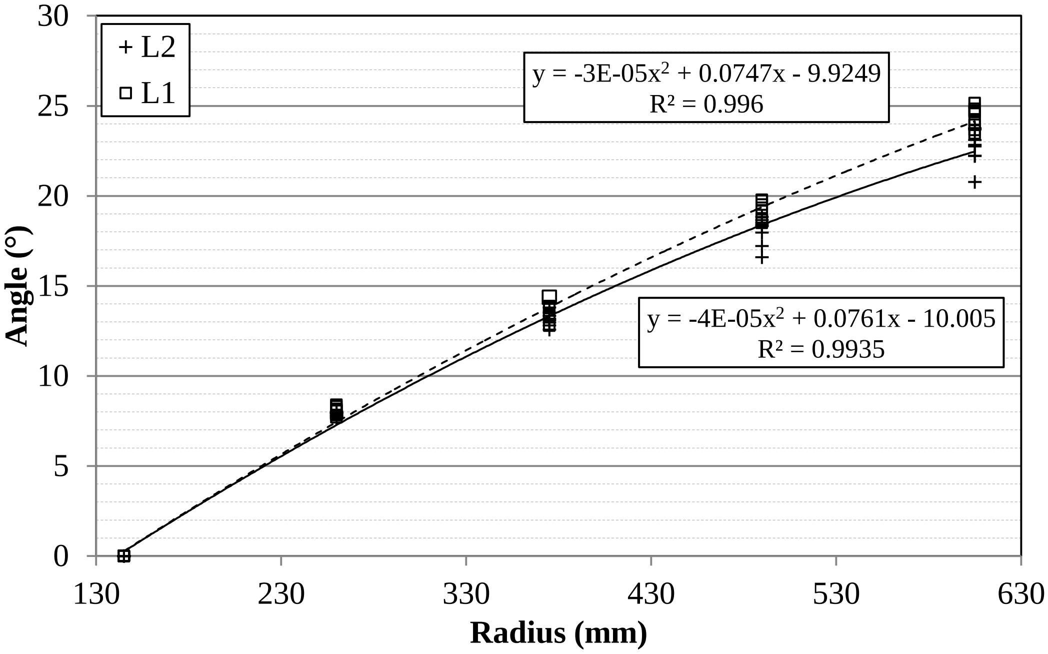

Figure D.6 - Relative blade angle distribution for the L1-fan and L2-fan at 145, 265, 375, 490 and 605 mm radial position

2. *Separation and Interpolation*

The data points shown in Figure D.4(c) have no particular structure or pattern relative to the x-axis. To calculate the camber and thickness distribution for the purpose of determining an average representative blade it was necessary to redistribute the data points in a regular arrangement to the x-axis. For interpolation of the points to be possible an increasing x-coordinate array was required. A blade aerofoil, however, could have two y-coordinates for a single x-coordinate and therefore it was necessary to separate the pressure and suction sides of each profile. Simply separating the positive y-coordinates from the negative y-coordinates was not found to be an accurate and effective method of separation. The algorithms used to separate the two sets of data had to work universally for any chord length and camber.

The interpolation scheme had to create a new set of x-coordinates without changing the geometry of the blade profile. The separate sides' data were used to interpolate the corresponding y-coordinates for an array of pre-defined x-coordinates. Due to the large number of data points, linear interpolation was determined to be an acceptable approximation. Figure D.7 compares the original data points to the new interpolated coordinates. Note the fine distribution of the x-coordinate points close to the leading edge to ensure a well approximated and defined leading edge. Combining the pressure and suction sides' interpolated data resulted in there being two y-coordinates for every equally spaced, incremented, x-coordinate.

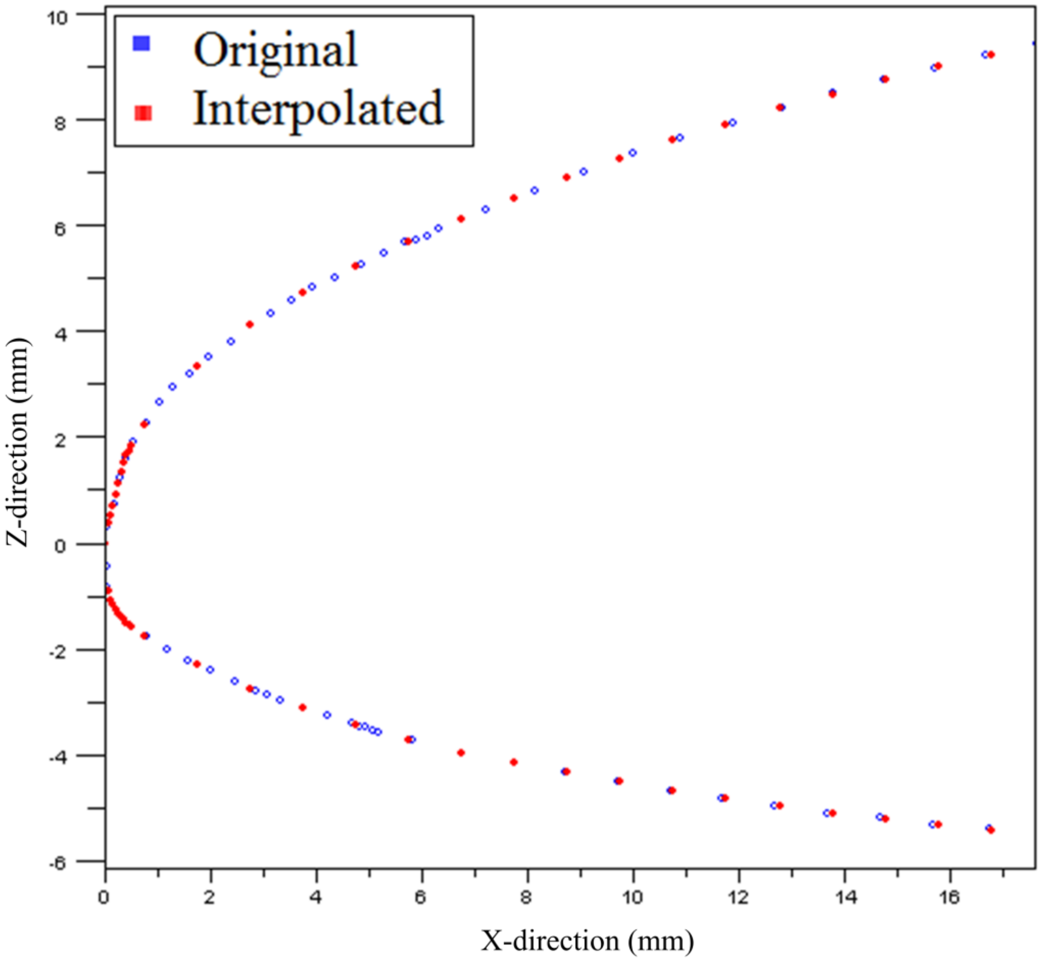

Figure D.7 - Original and interpolated points of the leading edge of a blade profile

3. *Camber*

Earlier in Chapter 3 the principles behind the thickness distribution and camber line was discussed. An approximation was also proposed for blade profiles with relatively small camber. Although the data was now regularly distributed for the approximate camber line approach, the camber was unknown. To validate the approximate camber line an attempt was made to find the true camber line.

To find the true camber line an alternate method than that explained in Chapter 3 had to be found. Figure D.8 illustrates the principle used to determine a more accurate estimate of the camber line. The camber line is defined below by the intersection point of equal distance between a specified coordinate on the suction side and its corresponding coordinate on the pressure side.

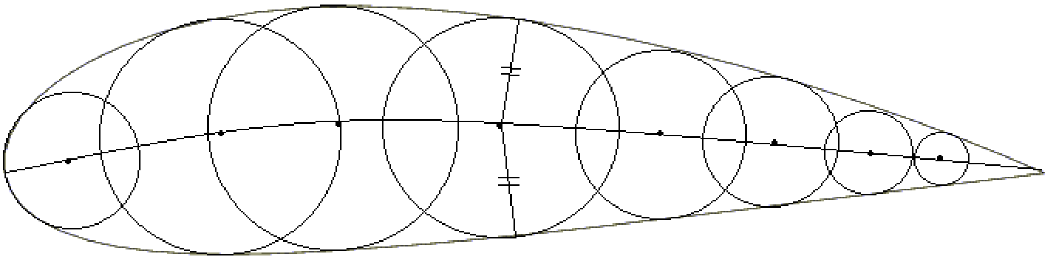

Figure D.8 - Accurate method of determining the camber line for an aerofoil

The algorithm used the golden section search method to find the intersection point. This is shown in Figure D.9 where the changing boundaries can also be seen. The search algorithm was carried out for all the interpolated x-coordinates and the final camber line which was calculated is compared to the approximate camber line in Figure D.10. It indicates the small difference between the two approximations. It must be noted that although this above described method is referred to the true camber line, both methodologies are still considered approximations, the one being more accurate than the other.

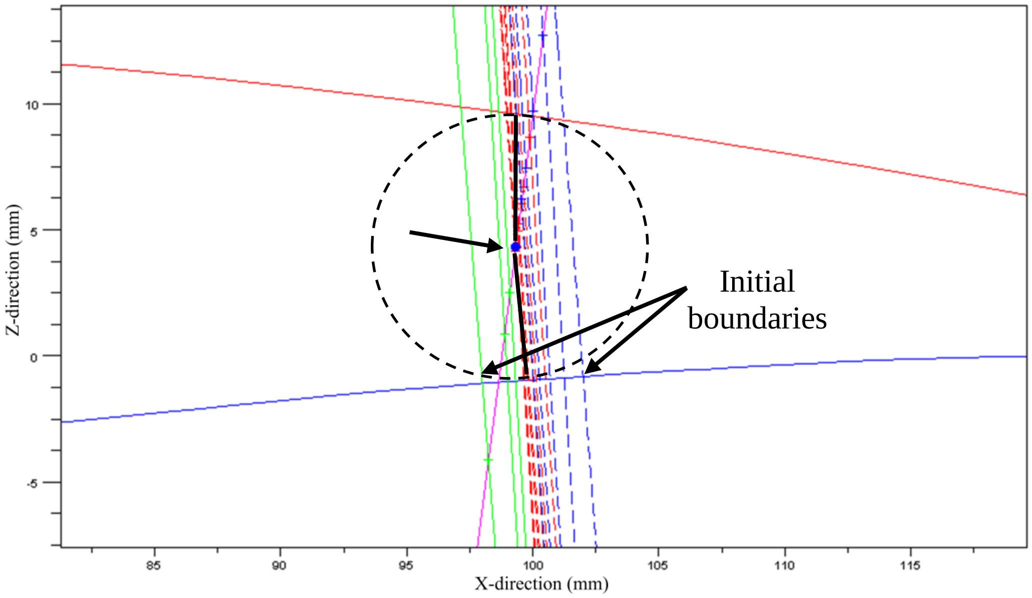

Figure D.9 - Search algorithm calculating the intersection point for equal lengths of the upper and lower tangent lines

Although it was possible to determine a more accurate camber line, the methodology for determining it was less stable than the approximate equation for every blade profile of all the fan blades. Having determined that there was a very small difference in the two methodologies the approximate camber line algorithm was used for further calculations.

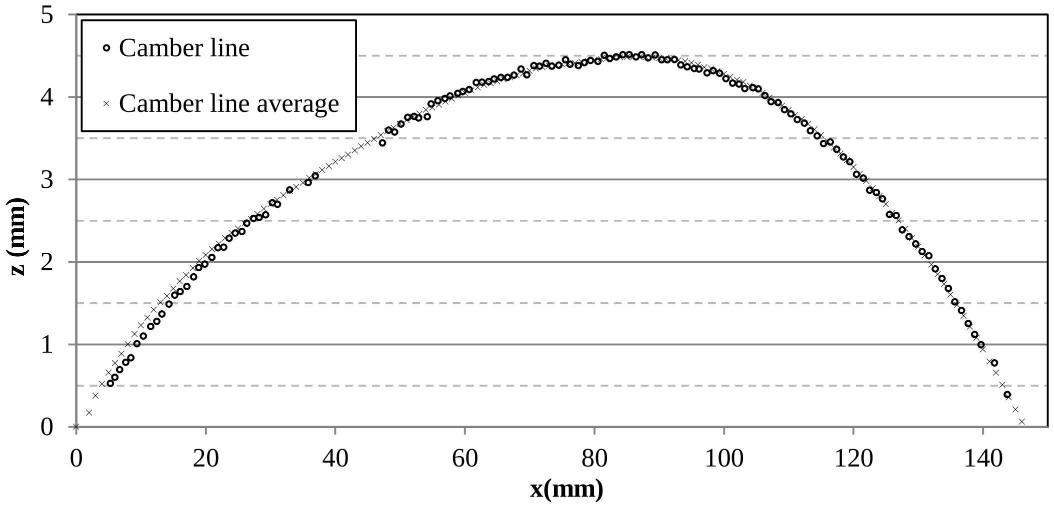

Figure D.10 - A comparison between the approximate camber line (average) and true camber line.

In Figure D.11 the thickness distributions and camber lines calculated by the approximate approach for five different radii (r > 145 mm) of the L2-fan are compared. Figure D.11 indicates that there is no notable change in the thickness distribution with increase in radius.

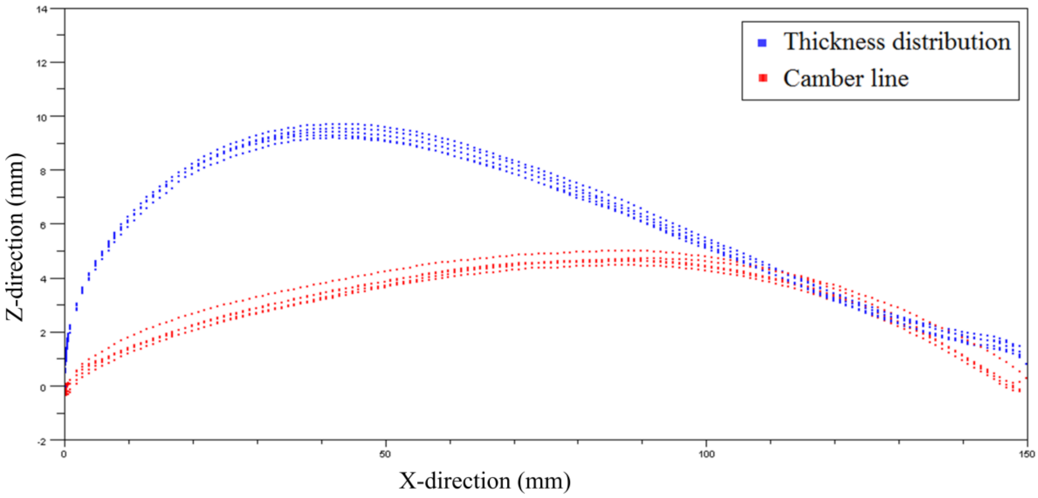

Figure D.11 - Thickness distribution and camber lines for various radial blade profiles of a single L2-fan blade

4. *Normalize and Average*

To determine the average representation of the blades, all camber lines and thickness distributions for each fan blade were normalized. An average camber and thickness distribution was calculated for every scanned radius using the combined data of eight (L-fans) or nine (N-fan) blades. Although an average fan could be calculated, the validity of the final result must be questioned. Determining the average profiles for each radius was possible as shown in Figure D.12. Attempting to realign and rotate each averaged profile according to an average blade angle distribution, without knowledge of the real stacking line, included a large number of approximations.

It is recommended that the methodology discussed above be used for the purpose of analysing single fan blades and comparing multiple blades of the same fan to each other. It was found that in determining the average representative of multiple fan blades, too many approximations are required.

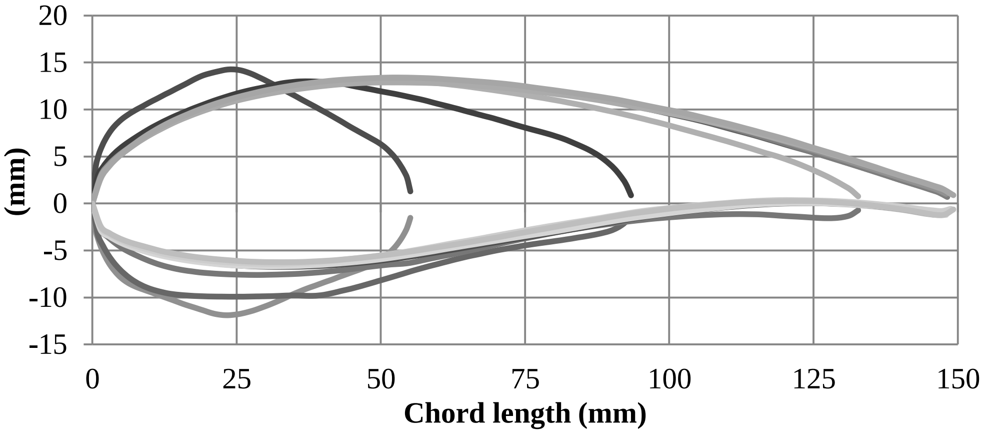

Figure D.12 - Average representative blade profiles of the L2-fan

E Fan performance characteristics

The performance characteristic maps for the three tested fans are shown in this appendix. For each of the three fans the static fan pressure, fan shaft power and fan static efficiency is given. Note that for the L-fans, a 1° change between blade-setting angles was used and for the N-fan, a 2° change. Using the fan scaling laws all performance characteristics were scaled to 900 rpm and a density of 1.2 kg/m^3

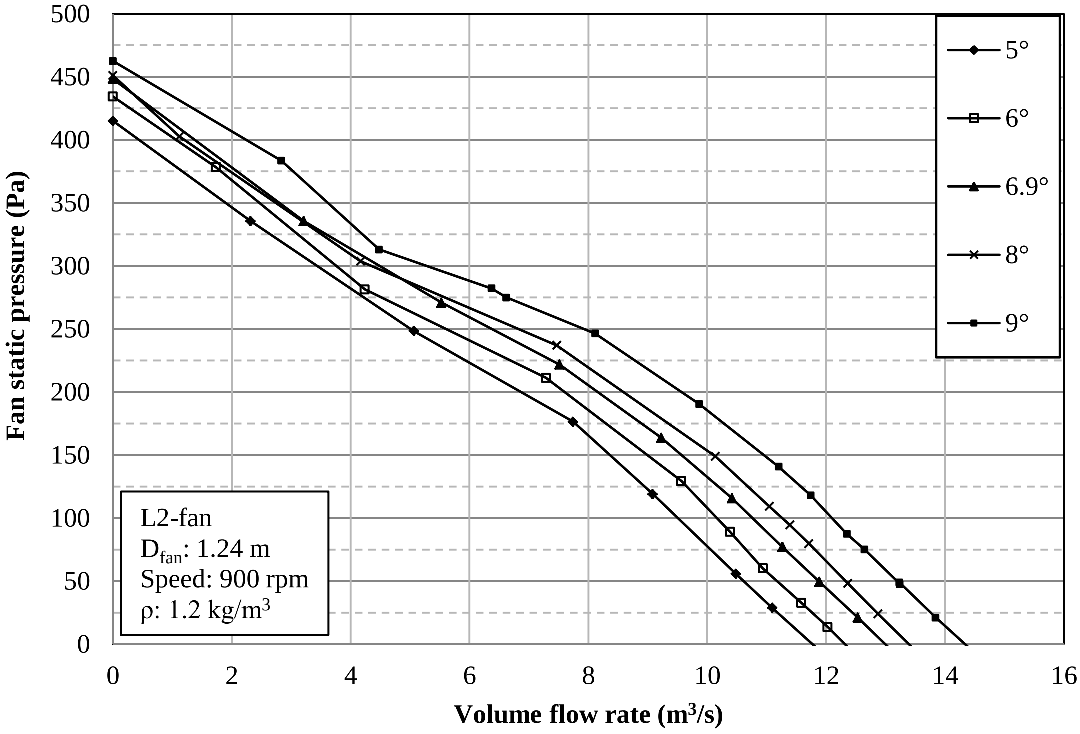

Figure E.1 - Fan static pressure map of five blade-setting angles for the L2-fan

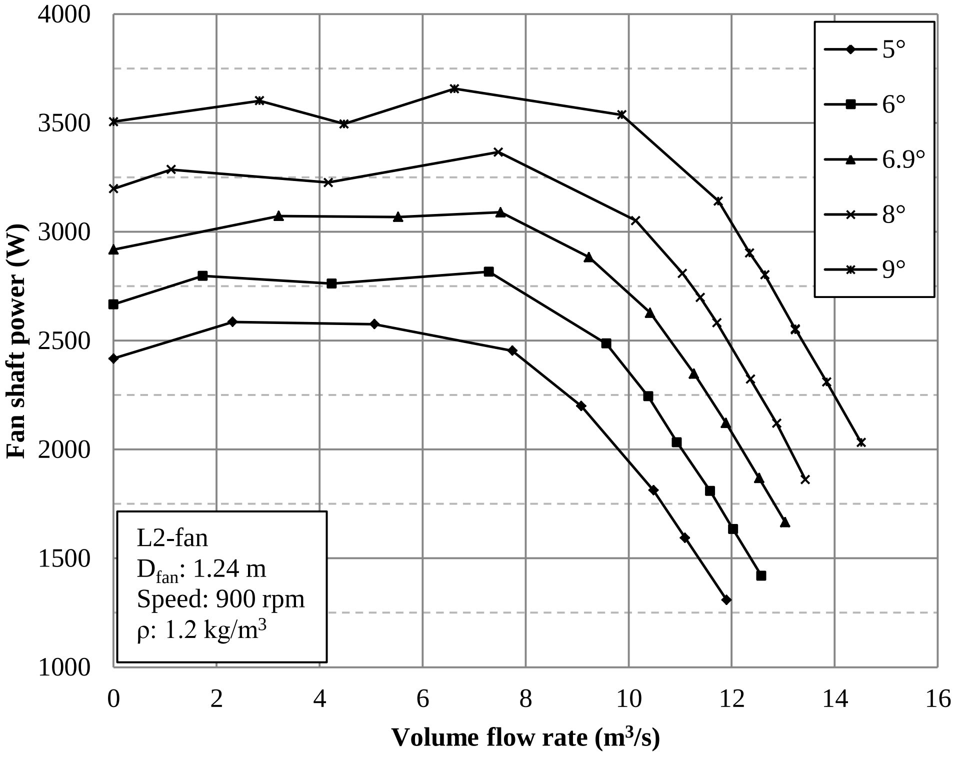

Figure E.2 - Fan shaft power map of five blade-setting angles for the L2-fan

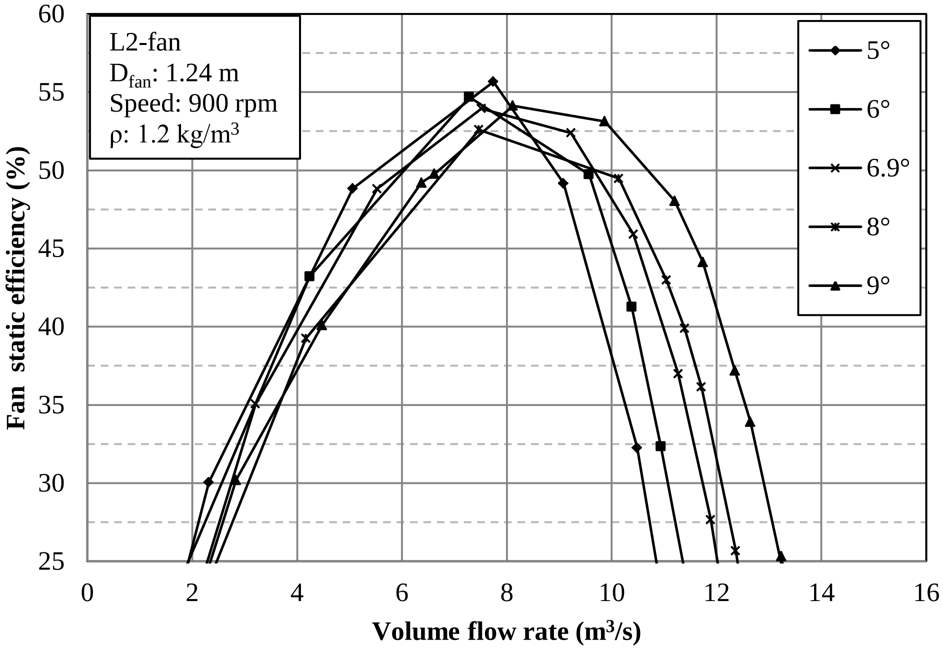

Figure E.3 - Fan static efficiency map of five blade-setting angles for the L2-fan

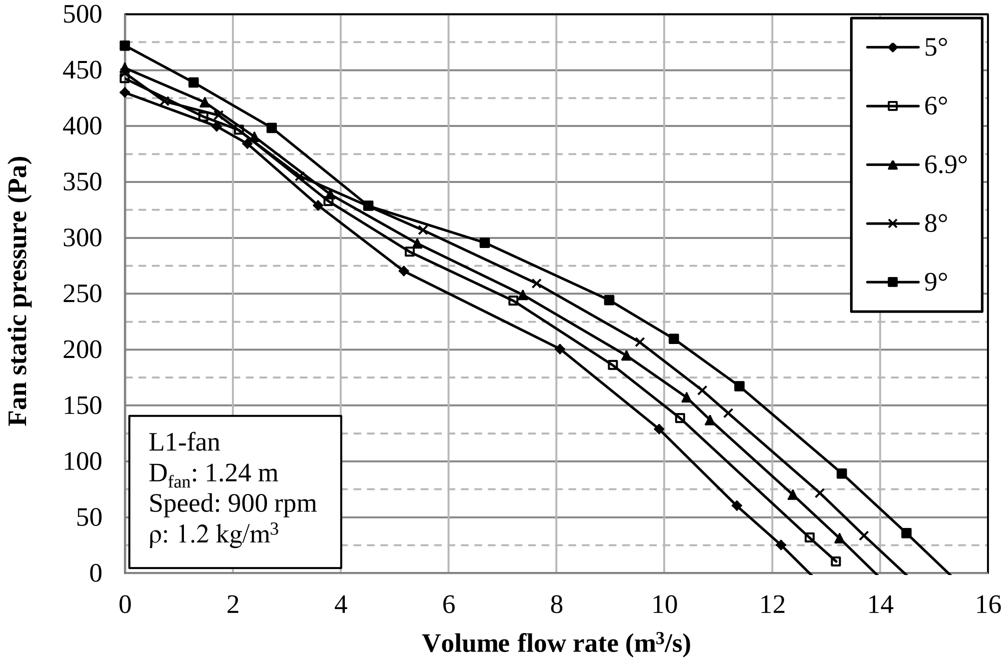

Figure E.4 - Fan static pressure map of five blade-setting angles for the L1-fan

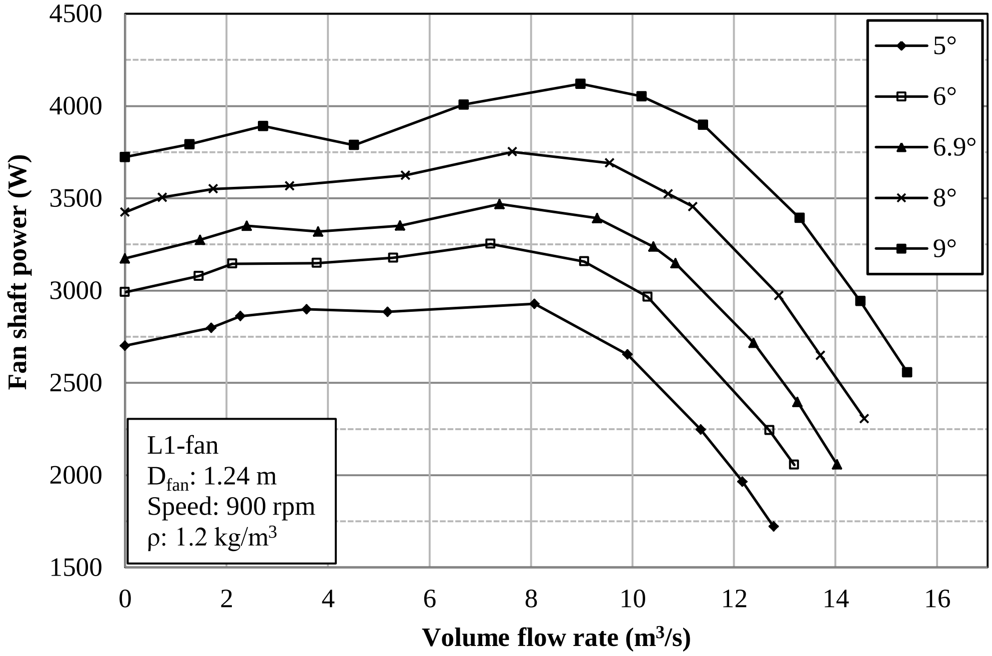

Figure E.5 - Fan shaft power map of five blade-setting angles for the L1-fan

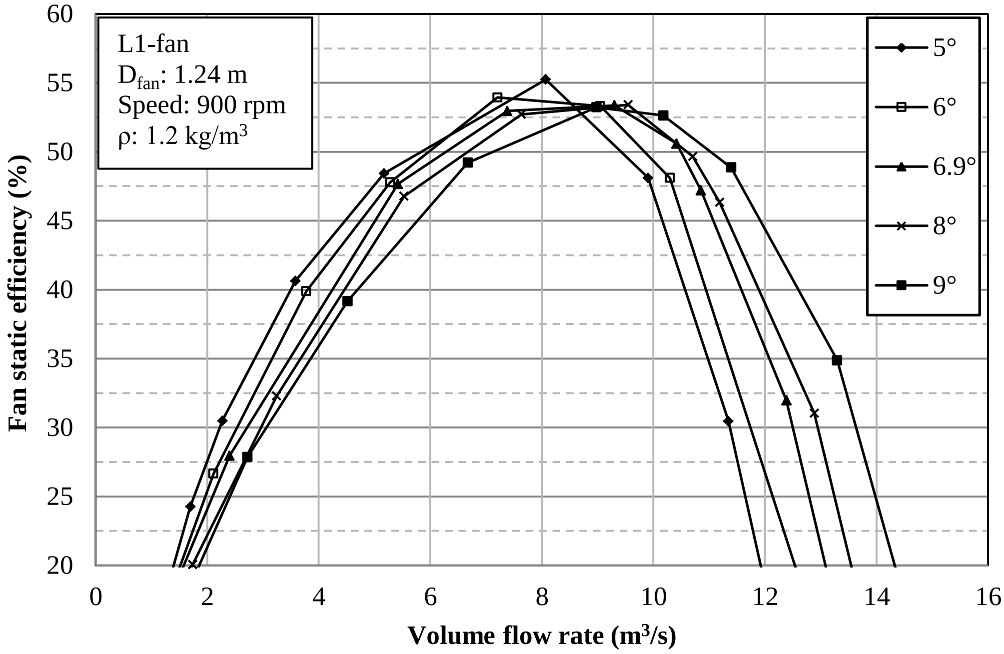

Figure E.6 - Fan static efficiency map of five blade-setting angles for the L1-fan

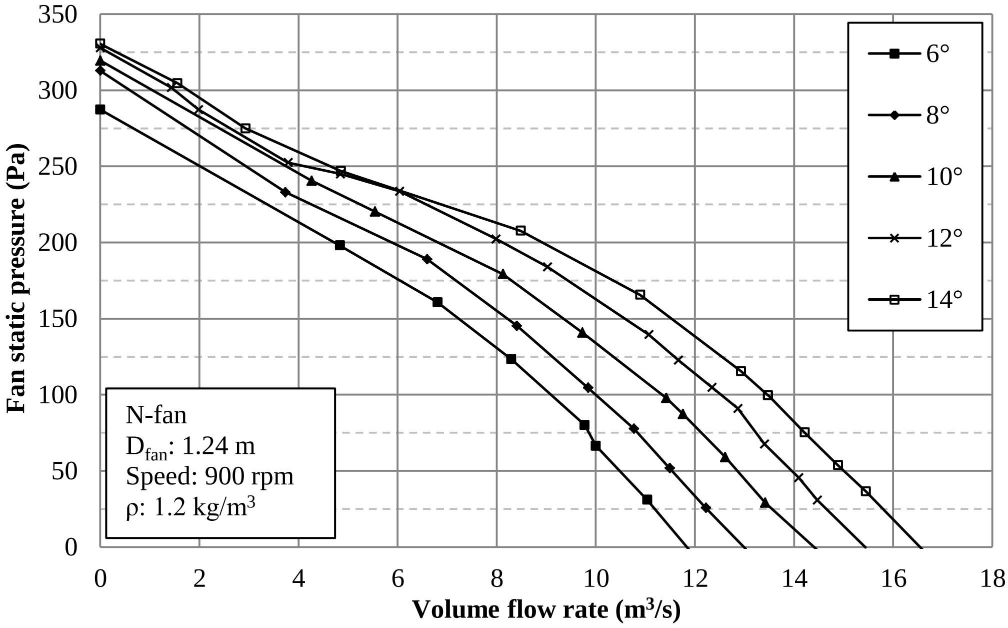

Figure E.7 - Fan static pressure map of five blade-setting angles for the N-fan

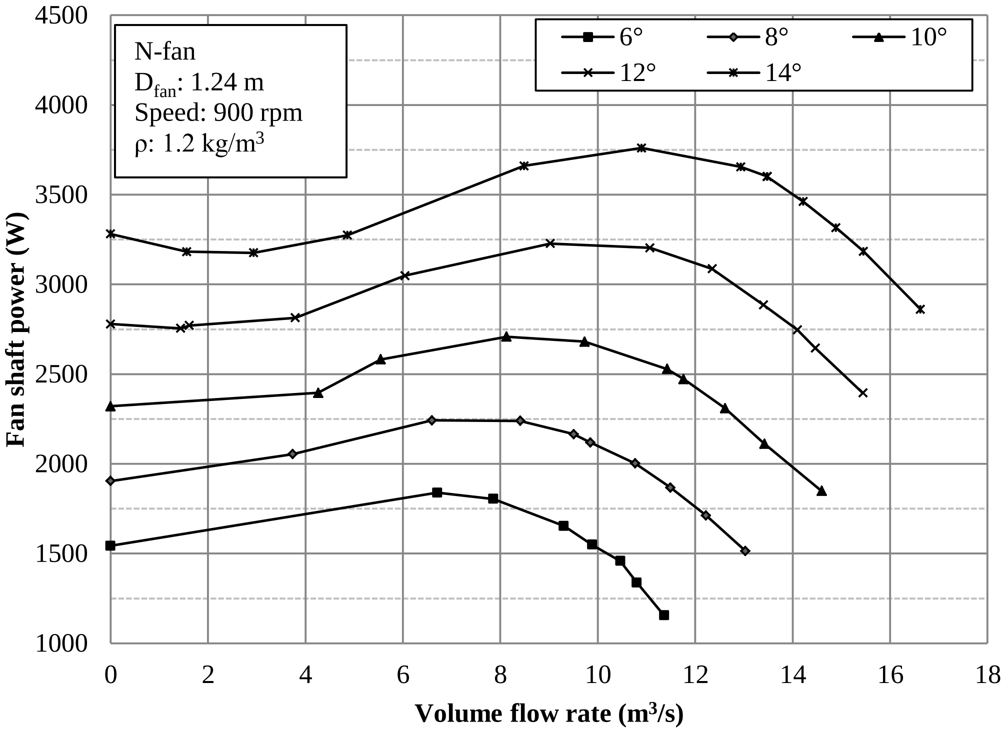

Figure E.8 - Fan shaft power map of five blade-setting angles for the N-fan

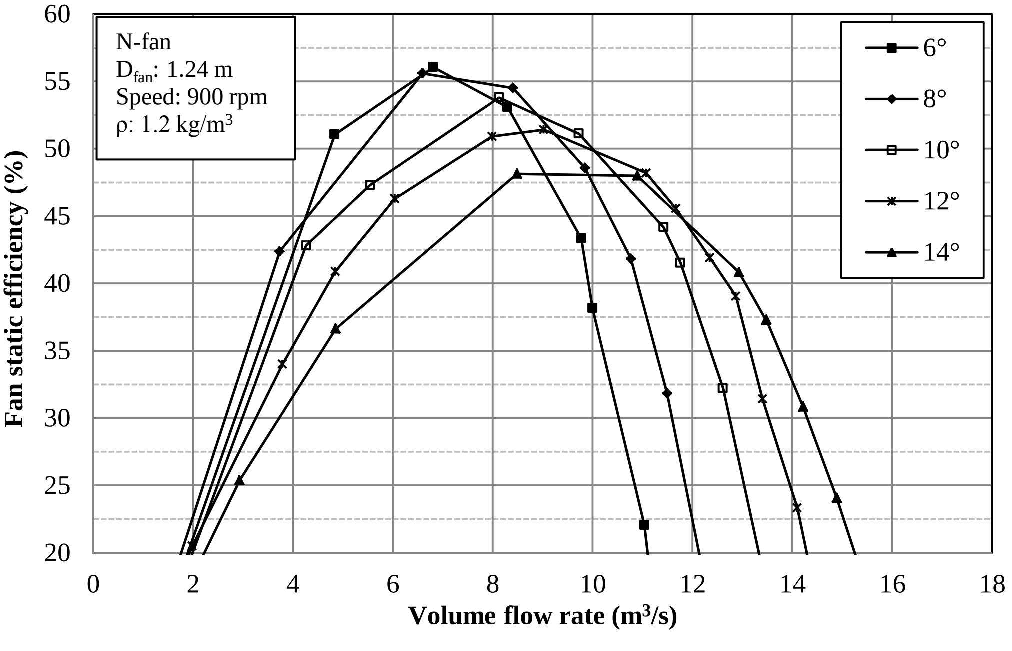

Figure E.9 - Fan static efficiency map of five blade-setting angles for the N-fan

F *Scilab*: Static fan blade balancing algorithm

The algorithm presented below was used to calculate the optimal arrangement between the fan blades of the L1-, L2- and N-fan. It calculated the arrangement which would result in the minimum static resultant, R.

```
function output = bladebalance();


mass = [1000 762 965 905 883 842 967 813];        //array of blade masses (g)
angle = [0 45 90 135 180 225 270 315];            // 8 blades = 360°/8 = 45°
R_max = 150;                                      // initial resultant (R) value
mass_min=[];                                      //array for results


for i = 1:8
   for ii = 1:8
      mass_temp = mass
      temp = mass_temp(i);
      mass_temp(i) = mass_temp(ii);
      mass_temp(ii) = temp;
      anglevectorx = cosd(angle);                 //calculating components x
      anglevectory = sind(angle);                 //calculating components y
      Wx = sum(mass_temp.*anglevectorx)           //summation of components x
      Wy = sum(mass_temp.*anglevectory)           //summation of components x
      R = sqrt(Wx^2+Wy^2)                         //resultant R
      if R < R_max then                           //”if” to determine minimum
         R_max = R
         mass_min = mass_temp;
      end
   end


end
   output = [R_max mass_min];
endfunction
```